Liquid Lubricants over Iron Oxides: A Scanning Probe Study

Moriguchi, Shiho

(Degree)
博士（理学）

(Date of Degree)
2020-09-25

(Date of Publication)
2021-09-01

(Resource Type)
doctoral thesis

(Report Number)
甲第7846号

(URL)
https://hdl.handle.net/20.500.14094/D1007846

Doctoral Dissertation

Liquid Lubricants over Iron Oxides: A Scanning Probe Study

（液中動作する走査プローブ顕微鏡を用いた
潤滑油と鉄酸化物界面の研究）

July 2020

Graduate School of Science, Kobe University

SHIHO MORIGUCHI

Table of Contents

Chapter 1 General introduction

1.1 Back ground

Most machines include sliding parts that perform relative motion while supporting the load. In the sliding part, repeated frictional motion is conducted, and wear and seizure are often generated. In order to reduce friction, lubrication has long been used, in which a third material (lubricant) having a small shear resistance is interposed between solids performing frictional motion to suppress direct contact between the solids. By reducing friction and preventing wear and seizure, the life of the machine is extended and energy is saved. According to the JOST report published in 1966, the economic effect of optimizing duplication is about 3% of Japan's GNP, which is not small at all.

Lubrication is classified into three types according to its form: hydrodynamic lubrication, mixed lubrication, and boundary lubrication. Hydrodynamic lubrication is a state in which a lubricant film sufficiently thicker than the surface roughness is formed between two sliding surfaces and the friction surfaces are completely separated. The condition in which the distance between two sliding surfaces is close and contact between solids is partially generated is called boundary lubrication. Boundary lubrication has been accepted as a typical lubrication system since W. B. Hardy proposed it in 1925[1]. Figure 1.1.1 shows an image of boundary lubrication. The state in which both hydrodynamic lubrication and boundary lubrication are mixed is called mixed lubrication. Figure 1.1.2 shows Stribeck curve. Hydrodynamic lubrication has high load capacity and low friction compared to other lubrication modes. In addition, it has high damping property, excellent anti-seizure property and anti-fatigue fracture property, and is the most ideal sliding mode. However, in an actual machine, it is difficult to realize hydrodynamic lubrication in all sliding parts, and a method to reduce friction is required even in boundary

lubrication, the distance between two sliding surfaces is small, and it is required to reduce friction with a film of a monolayer[1] or multi-molecular layers of at most few layers[2]. In these circumstances, the adsorbed layers and liquid covering the layers form an easily sheared film to minimize adhesion and wear.[3]

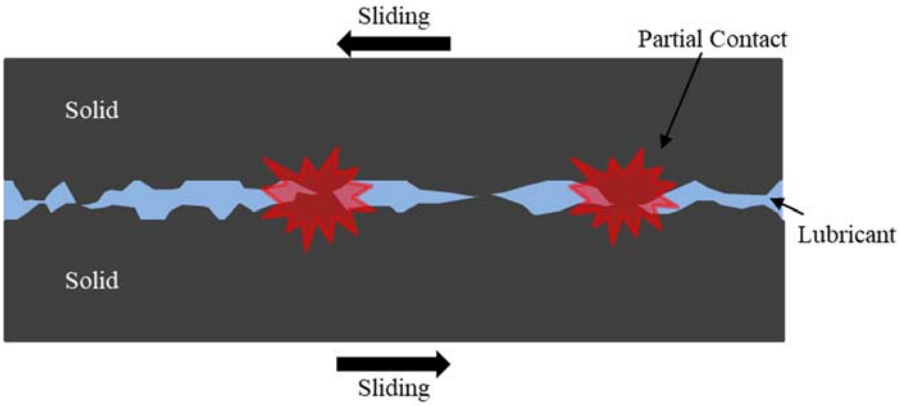

Figure 1.1.1 Image of boundary lubrication. the distance between two sliding surfaces is close and contact between solids is partially generated.

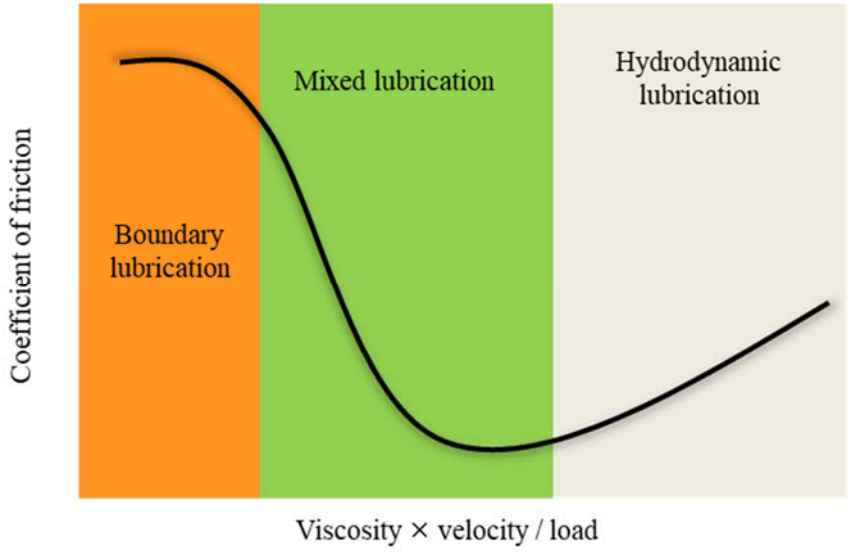

Figure 1.1.2 Stribrck curve which shows that friction coefficient is a non-linear function of the contact load, the lubricant viscosity and the lubricant entrainment speed.

As one of the representative lubricants which realize the friction reduction of the sliding part which takes the boundary lubrication form, there are lubricating oils such as engine oil. The lubricating oil consists of a base oil which is a nonpolar organic solvent and a modifier which is a polar compound. Because the prevention of wear and seizure and reduction of friction in boundary lubrication cannot be sufficiently achieved only by the performance of base oil, modifiers are used as a countermeasure. This modifier reduces friction and prevents wear and seizure by modifying the solid surface or adsorbing to the solid surface. Controlling the adsorption of modifiers to the solid surface at the boundary lubrication is the key to smooth sliding and stable friction. Modifiers are classified into extreme pressure agents, antifriction agents, and oiliness agents according to their operating environments and mechanisms. For example, a modifier classified as an extreme pressure agent or antifriction agent prevents seizure and wear by forming a tribofilm of reaction secondary products on a solid surface. Although there is no clear difference between the extreme pressure agent and the antifriction agent, the extreme pressure agent is mainly used when the sliding part has high temperature, high contact pressure and high sliding speed, and the antifriction agent is mainly used when the sliding part has high contact pressure and low sliding speed, as distinguished by the operating environment. On the other hand, a modifier classified as an oiliness agent forms a molecular layer by physical and chemical adsorption on a solid surface, and reduces friction by preventing direct contact between solids. It is used when the temperature of the sliding part is not too high compared with room temperature. Figure. 1.1.3 shows the simplest schematic diagram of the function of extreme pressure agent, antifriction agent (a) and oiliness agent (b).

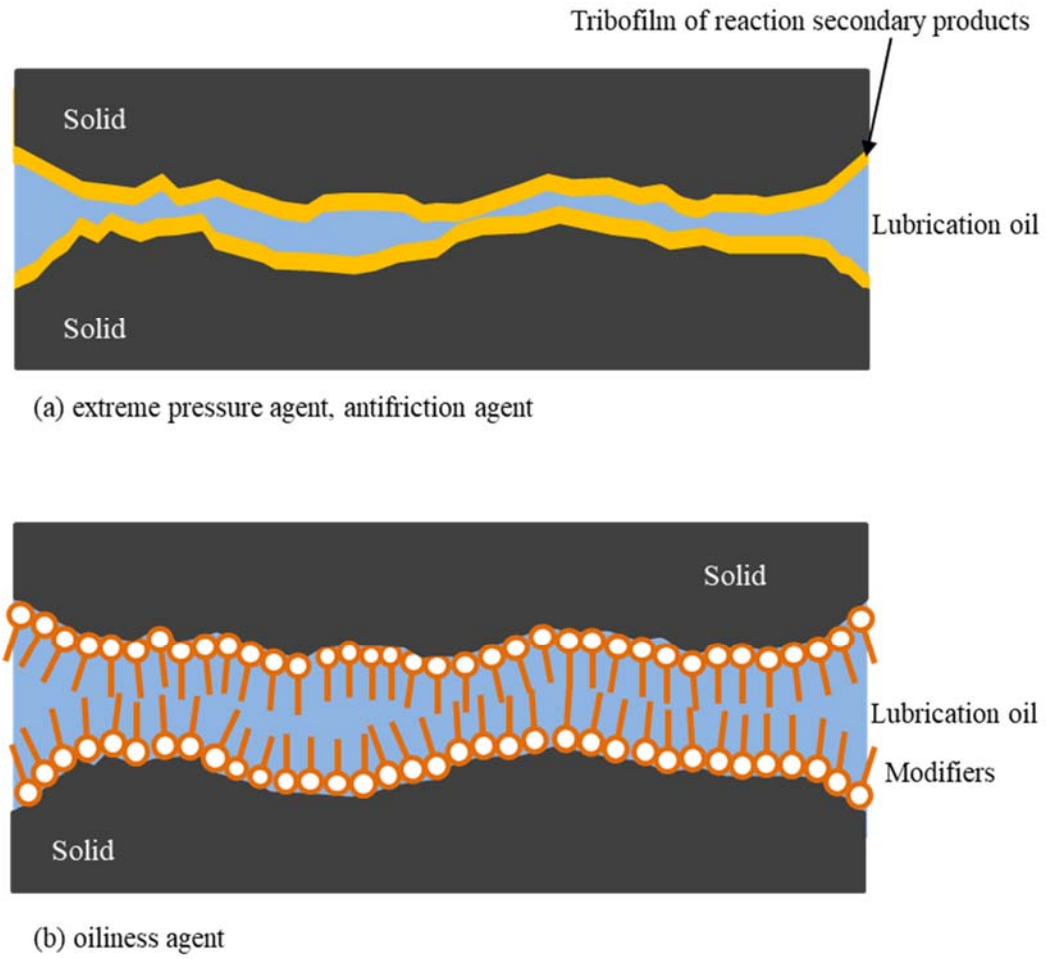

Figure 1.1.3 A schematic diagram of the function of (a) extreme pressure agent, antifriction agent and (b) oiliness agent. Modifiers contained in the lubricants form an adsorbed film on the metal surface to prevent direct contact between metals.

There have been many studies on modifiers. Since it was the first priority to attempt the life extension of the machine by suppressing abrasion and seizure, the research on the film formation by the extreme pressure agent was mainly carried out at the beginning.[4-9] However, recently, by development of new materials, improvement of surface treatment technology, improvement of machining accuracy, etc., seizure has become less a problem than before. Then, the interest has also shifted to how to reduce the friction on the assumption that the seizure does not occur at

present. The modifier adsorption film greatly contributes to the reduction of friction, and knowing and controlling the modifier adsorption film is the key to controlling lubrication. Especially, in the boundary lubrication in which the single molecule adsorption film influences the friction reduction characteristic, the adsorption of the modifier to the solid surface directly leads to the performance improvement of the lubricating oil. There have been many studies evaluating the friction reduction effect of a modifier adsorption film[10-12]. However, few studies have visualized how modifier molecules are adsorbed on solid surfaces. Visualizing the adsorption film of the modifier with molecular resolution means that it is possible to directly analyze how the modifier is adsorbed on the solid surface, which will help to clarify the formation mechanism of the adsorbent film. And, if the effect of the adsorption film structure at the molecular level on the macroscopic lubrication characteristics can be evaluated by considering the adsorption state of the modifier together with the actual lubrication performance, mixing of the modifier with higher performance and the thinnest concentration which brings about the effect on the lubrication can be designed with the theoretical reason.

On the other hand, even today, it is not easy to characterize adsorbed modifiers of nanometer-scale thickness. They are always buried in lubricant–solid interfaces. Electron-based methods for surface analysis do not function there. In situ, hopefully operando methods working in lubricants should have been developed, since weakly adsorbed modifiers leave the surface when the surrounding lubricant is removed. The mass of adsorbed modifiers was determined with microbalance sensors.[13,14] Infrared absorption,[15–17] Raman scattering,[18] and sum-frequency generation[19] provided vibrational spectra of adsorbed modifiers to estimate their chemical structure. The layer thickness of deuterium-labeled modifiers was evaluated in a sub-nanometer

precision by fitting neutron reflectivity as a function of scattering vector length.[20,21] In these methods, the mass of mass of adsorbed modifiers, their chemical structure, and the thickness of the adsorption film were clarified. In actual sliding parts, it is expected that the adsorption is not uniform, but at present, there is only an analysis method based on the assumption that the adsorption is uniform. Recently, Hirayama et al. applied Frequency-Modulation Atomic Force Microscopy (FM-AFM) for visualizing palmitic acid modifier layers on copper films immersed in a hexadecane-based model lubricant[22]. Okubo et al. evaluated the thickness of adsorption films composed of trimethylolpropane trioleate on the diamond-like carbons immersed in a PAO-based model lubricant using FM-AFM.[23]. AFM/Scanning Probe Microscope (SPM) is a useful microscope that provides new knowledge in nanoscale analysis. It has a spatial resolution on the order of nanometers in the horizontal direction and on the order of sub nanometers in the vertical direction, and it can detect unevenness at the molecular level of the adsorption film in either direction. Conventional AFM/SPM has been used to evaluate the thickness of the adsorption film[24] and the mechanical response of the polymer brush[25]. The FM-AFM which has superior spatial resolution and force sensitivity compared with the conventional AFM/SPM has been operable only in ultrahigh vacuum[26-28]. However, in recent years, drastic noise reduction of the detection circuit system has been realized[29], and at present, it has been operated even in air and liquid. Since the FM-AFM has a 10-pN-order force sensitivity, not only a solid adsorption film of modifier but also a liquid-like adsorption film of modifier at the solid-liquid interface can be captured. In addition to high force sensitivity, FM-AFM has a special resolution of atomic and molecular size. Especially, in boundary lubrication where the monolayer of the modifiers influences the lubrication performance, it is a great advantage that the adsorption film can be observed with molecular resolution.

For example, extreme pressure agents and antifriction agents form a tribofilm of reaction secondary products on a solid surface to prevent seizure and wear. The formed reaction coating is hard enough to be recognized as a solid and can be analyzed with a conventional AFM/SPM or other analysis method such as AES, XPS and TEM. However, the precursors formed by the physical or chemical adsorption of modifier molecules on the solid surface as a preliminary step to this reaction are so soft that they require a 10-pN-order force sensitivity achieved in FM-AFM for detecting the layer-induced force response. The adsorption film formed by the oiliness agents is as soft as the precursor adsorption film formed by the extreme-pressure agent or the antifriction agent. Precursor adsorption films formed by phosphate esters, typical antifriction agents, are analyzed in Chapter 2, and those formed by carboxylic acids, typical oiliness agents, in Chapter 3.

In an actual lubricating oil, a plurality of kinds of modifiers are mixed to improve performance. It is very useful in designing a modifier formulation to know which modifier preferentially forms an adsorption film and provides a good effect, when multiple modifiers are mixed. SPM can measure a variety of physical quantities in addition to the mechanical responses described above. In Chapter 4, the possibility of analyzing the adsorption of modifiers using surface potential distribution is discussed, which is one of the physical quantities measured by SPM.

FM-AFM can be expected as a new method to accelerate the development of lubricants by clarifying the behavior of lubricants at the friction interface on a molecular scale and providing a theoretical basis for the design of lubricants.

1.2 Methods

1.2.1 SPM

1.2.1.1 Introduction and principle of SPM

Scanning probe microscope (SPM) is a microscope that can make images of various physical property by scanning a small probe near the sample surface and detecting an atomic force acting between the probe tip and the sample surface. The most typical function is Atomic Force Microscopy (AFM)[30] that measures a three-dimensional topography of the sample surface by detecting the atomic force acting between the probe and the sample surface. In addition to AFM, there are various functions such as Scanning Tunneling Microscopy (STM)[31, 32] which measures a three-dimensional topography of the sample surface by detecting the tunneling current, Lateral Force Microscopy (LFM) which makes the image of a friction distribution by detecting lateral force, Kelvin Probe Force Microscope (KPFM) which makes the image of surface potential distribution by detecting electro static force, and Magnetic Force Microscope (MFM) which makes the image of magnetic information distribution by detecting magnetic force. KPFM was used in this study and will be discussed in detail in Chapter 4.

Figure. 1.2.1 shows a structure diagram of SPM. In the SPM measurement, a micrometer-sized cantilever is used for the force detection. There is a small probe on the end of the cantilever. And laser beam is irradiated from a laser diode. After passing through a lens, the laser beam is vertically turned down by a beam splitter and reflected on the back side of the cantilever. The reflected laser beam is turned left with a mirror and goes into the photodetector. The sample is set on a tube piezo scanner, and below the cantilever.

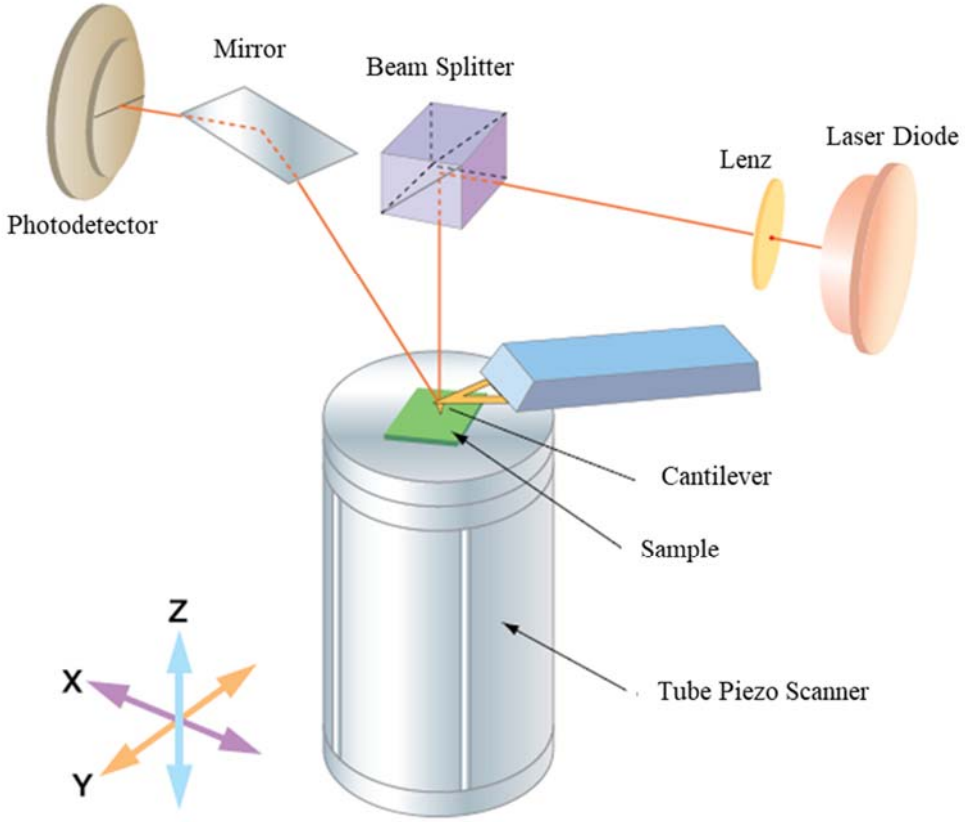

Figure 1.2.1 Structure diagram of AFM

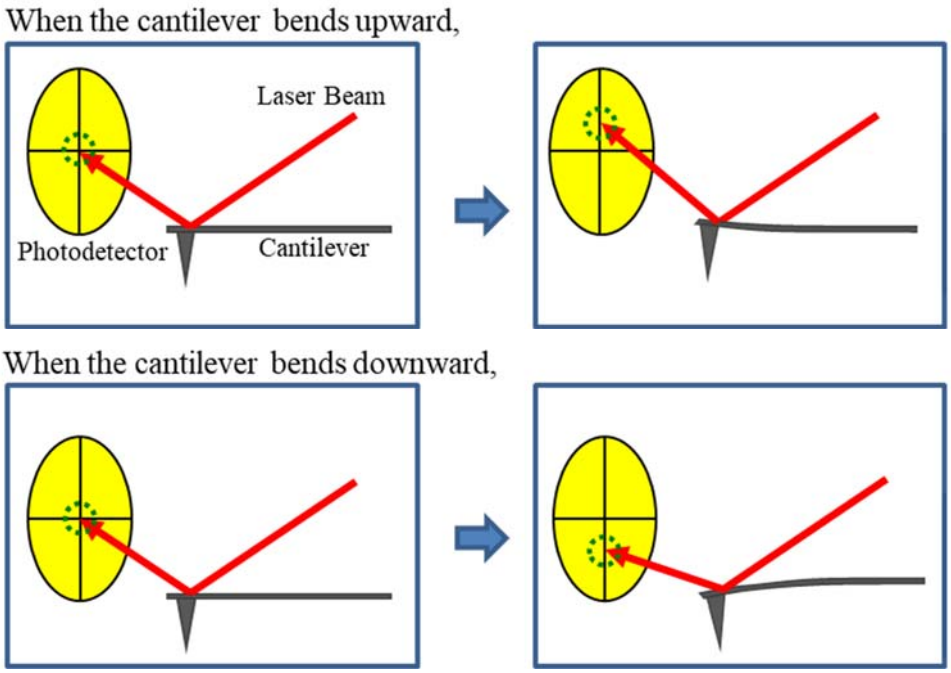

Figure 1.2.2 A schematic diagram of displacement of the tip apex.

Figure 1.2.2 shows a schematic diagram of an optical setup for detecting the tip displacement. When the cantilever bends upward, the reflected beam shifts upward in the photodetector. When the cantilever bends downward, the reflected beam goes down in the photodetector. Displacement of the tip apex as small as in the order of nanometers can be detected using this simple optical setup.

1.2.1.2 Control method of AFM scanning

Although there are several basic scanning methods in AFM, the dynamic mode is currently the mainstream. In dynamic mode, the cantilever is mechanically oscillated, and the cantilever oscillation is changed by the interaction force between the probe tip and the sample surface. The change in the cantilever oscillation is detected by the optical setup described above. Dynamic mode is classified into amplitude-modulation (AM) and frequency-modulation (FM) according to the control method.

In AM control, the cantilever is mechanically oscillated at a frequency (operating frequency) close to its resonance frequency. When repulsive or attractive force is applied on the probe tip, the oscillation amplitude at the operating frequency decreases. This is illustrated in Figure 1.2.3. Whether the force applied to the probe tip is repulsive or attractive, the oscillation amplitude decreases. Therefore, in AM, it cannot be determined whether the force acting on the probe tip is attractive or repulsive.

Figure 1.2.4 shows a scanning to observe topography of the sample surface. The topography is traced with regulation of the tip–surface distance by keeping the amplitude at a prefixed setpoint. Holding the oscillation amplitude at the fixed setpoint means that the atomic force acting between the probe tip and the sample surface is kept constant. The atomic force changes depending on the distance between atoms and the type of atom. Therefore, scanning with the constant atomic force means

measuring the topography and atomic image of the sample surface. AM-AFM has spatial resolutions of few nanometers in the XY direction and sub nanometers in the Z direction.

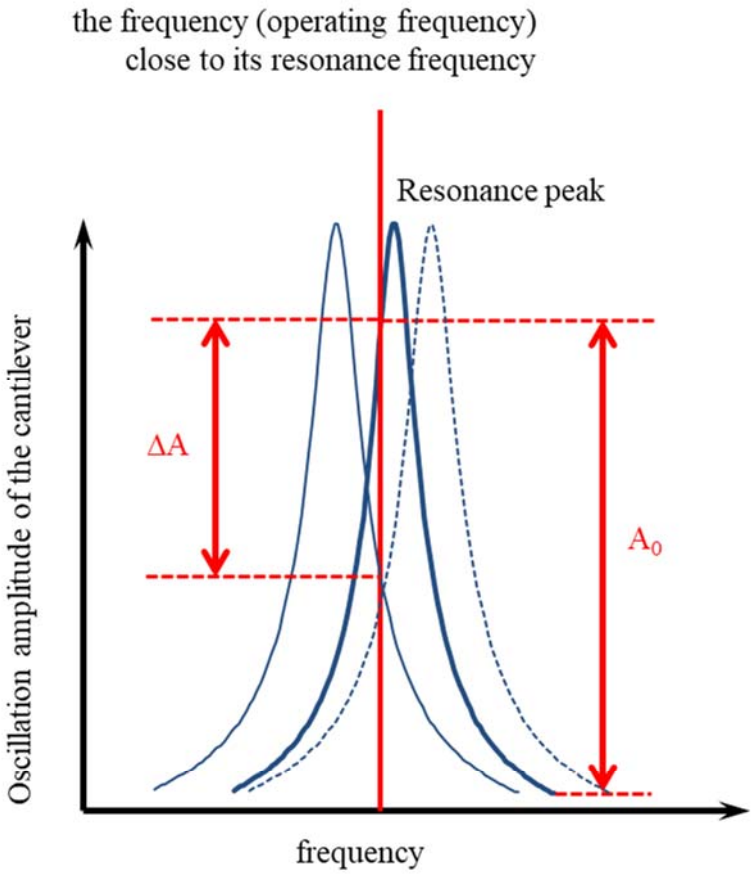

Figure 1.2.3 In AM-AFM, the cantilever is mechanically oscillated at the frequency close to its resonance frequency. Then the change in the oscillation amplitude caused by the atomic force is monitored

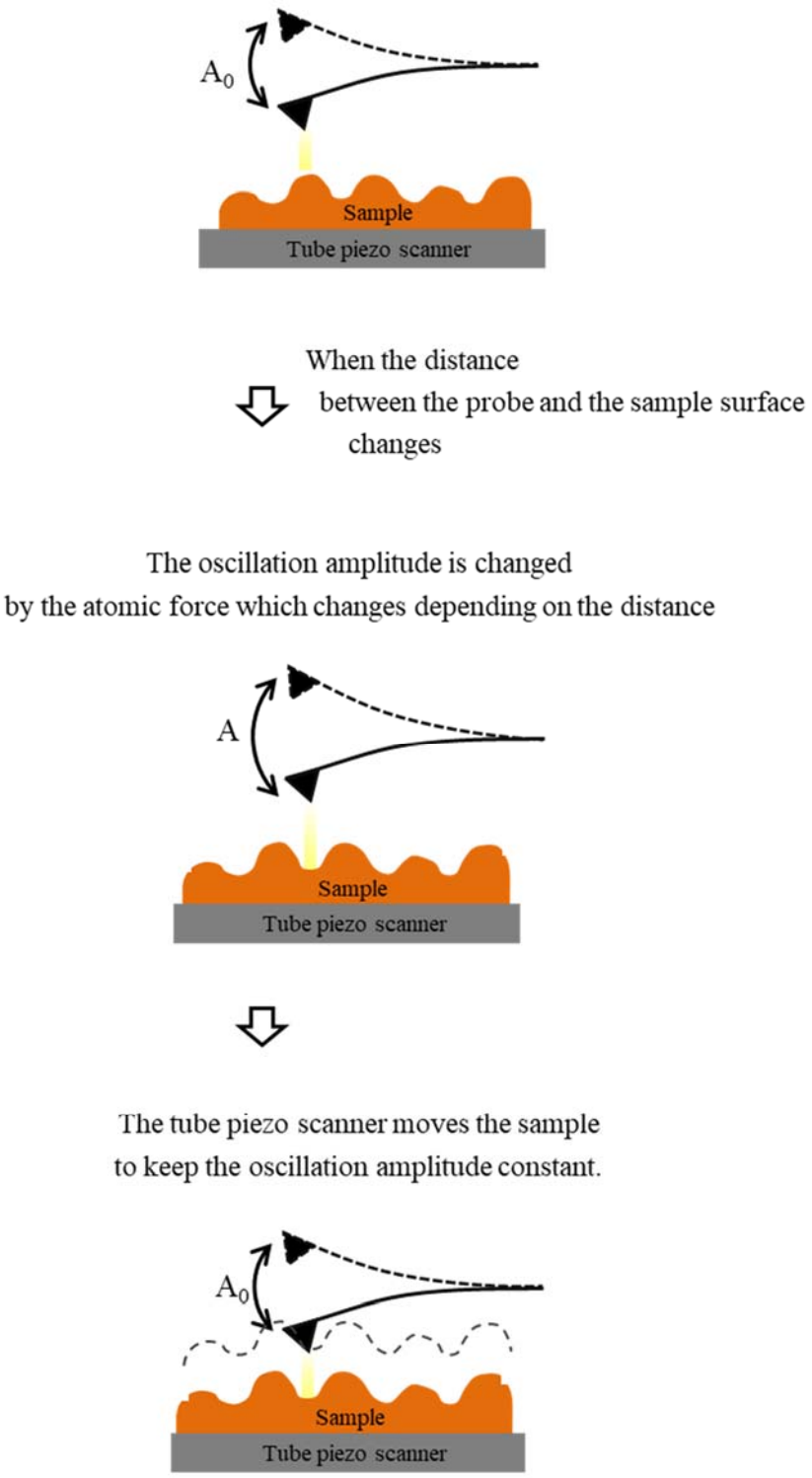

Figure 1.2.4 When the oscillation amplitude is changed by the atomic force, the tube piezo scanner moves the sample to keep the oscillation amplitude constant.

In FM control, the cantilever is mechanically oscillated at its resonance frequency. The oscillation amplitude is feedback regulated to keep a fixed length. Cantilever oscillation is modified by force pushing a nanometer-sized tip at the oscillating end, and the resonance frequency of cantilever oscillation shifts accordingly. When repulsive force is applied on the tip, the resonance frequency increases. When attractive force is present on the tip, the resonance frequency decreases. By monitoring the shift of resonance frequency, the force as weak as 10 pico newton can be determined, even in liquid. This is illustrated in Figure. 1.2.5.

In order to detect a smaller frequency shift, it is important that the Q value of the resonance peak of the cantilever oscillation is large. Therefore, it was originally used in a vacuum[26-28] where the Q value of the resonance peak is larger than in gas and liquid. However, in recent year, it has been possible to greatly reduce noise in the detection circuit[29], and to operate in air and liquid.

The topography is traced with regulation of the tip–surface distance by keeping the frequency shift at a prefixed setpoint as shown by Figure 1.2.6. Holding the frequency shift at the fixed setpoint also means that the atomic force acting between the probe tip and the sample surface is kept constant, as same as the oscillation amplitude is kept constant in AM-AFM. In FM control, to maintain the following three conditions, triple feedback loops are constructed.

1. The frequency of the cantilever oscillation is adjusted to be equal to the resonant frequency
2. The amplitude of the cantilever oscillation is kept constant
3. The position of the sample in the vertical direction is adjusted so that the resonance frequency shift Δf is constant.

In AM control, the only one feedback loop for adjusting the vertical position of the sample is operated so that the oscillation amplitude of the cantilever at a specific frequency is constant. Therefore, AM-AFM has a simpler device configuration, works more stably, and is easier to operate than FM-AFM. On the other hand, the advantage of FM-AFM is that the change in the cantilever oscillation caused by smaller atomic force can be detected, because the frequency shift can be detected more sensitive than the oscillation amplitude. As a result, FM-AFM has a spatial resolution of sub-nanometers in all directions. Its resolution is higher than AM-AFM.

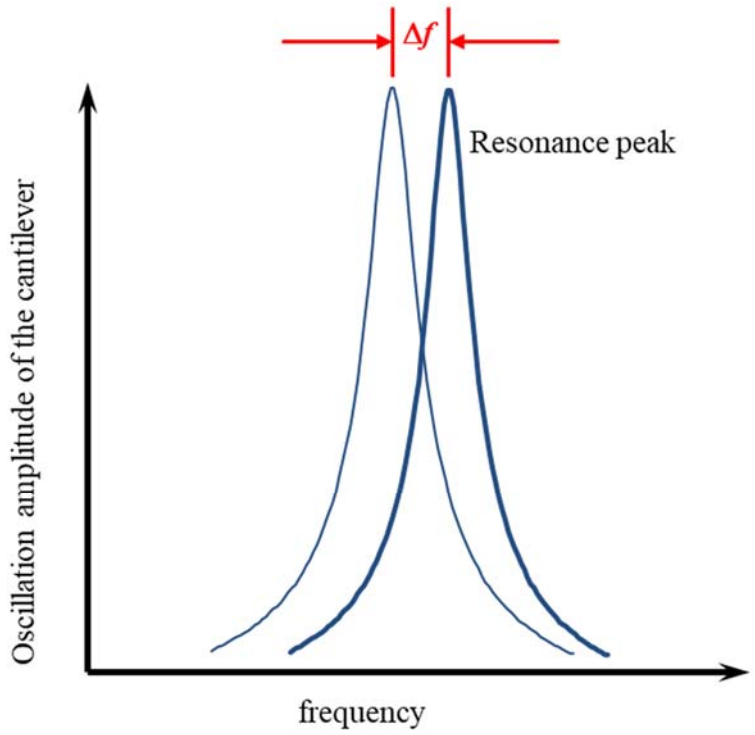

Figure 1.2.5 In FM-AFM, the cantilever is mechanically oscillated at its resonance frequency. Then the change in the frequency shift caused by the atomic force is monitored.

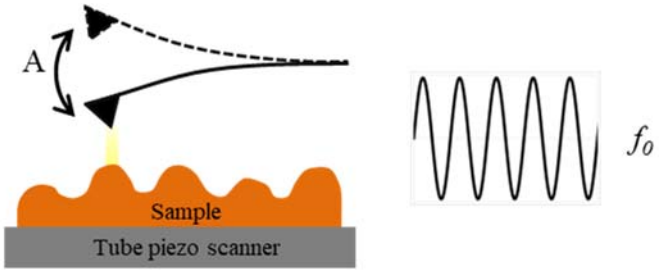

When the distance
between the probe and the sample surface
changes

The resonance frequency is changed
by the atomic force which changes depending on the distance

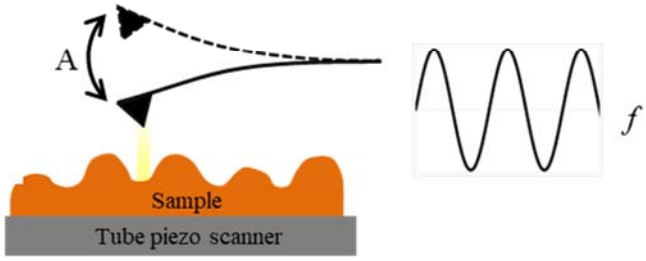

The tube piezo scanner moves the sample to keep the frequency shift constant.

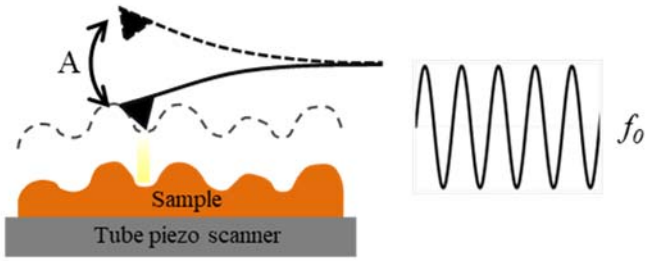

Figure 1.2.6 When the frequency shift is changed by the atomic force, the tube piezo scanner moves the sample to keep the oscillation amplitude constant.

Another definite advantage of FM-AFM is imaging local density distribution of the liquid modified over the solid by mapping the force distribution in the ZX plane.[33] In force mapping in the ZX plane, the oscillating cantilever is scanned vertically from the bulk liquid to the solid surface. The shift of resonance frequency is recorded as a function of the vertical coordinate to make one frequency-shift-distance curve. Then the tip laterally shifted and another vertical scan is conducted. By repeating the vertical scans on a plane perpendicular to the liquid-solid interface, force on the tip is mapped on the plane. Figure.1.2.7 shows a schematic diagram of force mapping in the ZX plane. Christoph Marutschke et al. reported a case about measuring the liquid structure of water in contact with Calcite by AM-AFM[34], but the data were less clear than those measured by FM-AFM[36-37]. Besides, Hagen Söngen et al. suggested three AFM equations that can be universally applied to analyze any dynamic AFM data[35]. Using these equations, a signal change reflecting the liquid structure of water in contact with Calcite could be clearly extracted from the signal measured by AM-AFM, but it required complicated calculations. Therefore, FM, which can be clearly evaluated from measured raw data, is more advantageous for measuring liquid structures.

A further advantage of FM-AFM is that forces can be determined from the frequency shift. The relationship between frequency shift and force is defined by Equation 1.2.1:[38]

$$\boldsymbol{F(z) = 2k_z \int_z^{\infty} \left(1 + \frac{A_0^{\frac{1}{2}}}{8\sqrt{\pi(t-z)}} \right) \Omega(t) - \frac{A_0^{\frac{3}{2}}}{\sqrt{2(t-z)}} \frac{d\Omega(t)}{dt} dt} \qquad 1.2.1$$

where k is the spring constant of the cantilever, F is the interaction force between the tip and the sample, A is the amplitude of the cantilever oscillation, and z is the closest

distance between the tip and the sample, ω_{res} is its unperturbed resonant frequency, $\Delta\omega$ is the change in the resonant frequency, and $\Omega(z) = \Delta\omega(z)/\omega_{res}$.

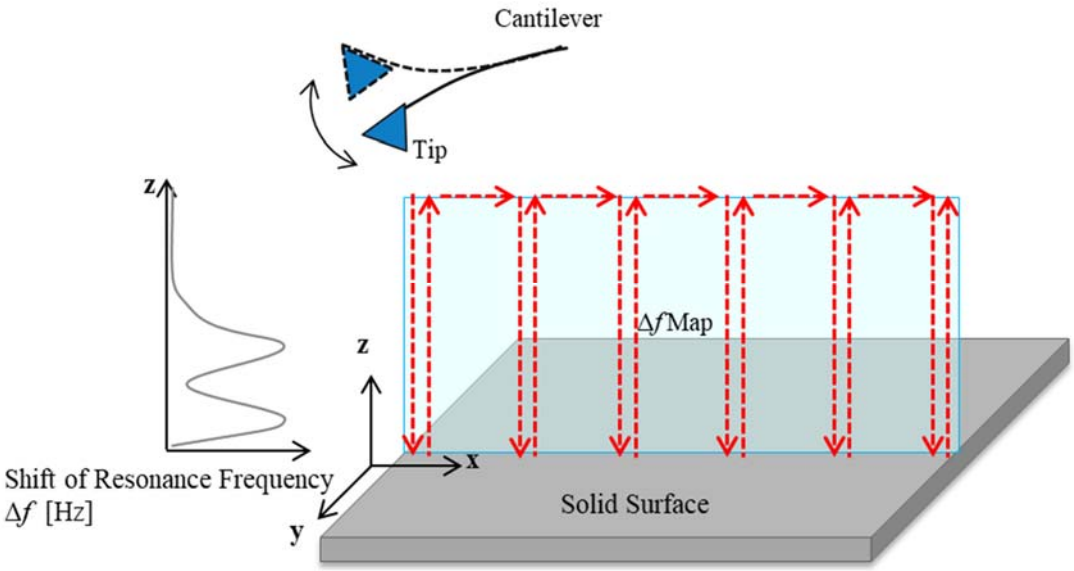

Figure 1.2.7 A schematic diagram of force mapping in the ZX plane

1.2.2 Pendulum-type friction tester

A pendulum-type friction tester designed by Norimune Soda is one of the representative instruments used to measure a dynamic friction coefficient. Figure 1.2.8 shows the configuration of the pendulum tester. In the pendulum type friction tester, a fulcrum of a pendulum is used as a boundary friction surface, and the oscillation amplitude of the pendulum is damped by the friction moment at the fulcrum of the pendulum. Figure 1.2.9 shows the fulcrum of the pendulum. Four balls (B) are fixed in an oil tank (A) by two, and a roller pin (C) fixed to the fulcrum of the pendulum is placed on the balls, and the testing machine is assembled so as to constitute four-point contact between the balls and the roller pins. The oil tank is filled with lubricating oil. Then the pendulum is moved away from a certain angle and oscillated naturally. The dynamic friction coefficient is calculated from the number of oscillation and the deflection angle in the damping process by Equation 1.2.2:

$$\boldsymbol{\mu = C \times \frac{\sum_{k=1}^{n}(A_0 - A_k)}{\sum_{k=1}^{n} k}} \qquad 1.2.2$$

where n is the number of recorded oscillations in each measurement run. A_0 is the initial amplitude of the pendulum oscillation, and A_k is the amplitude of the nth oscillation. C is a constant determined by the length of the pendulum and the weight of the fulcrum.

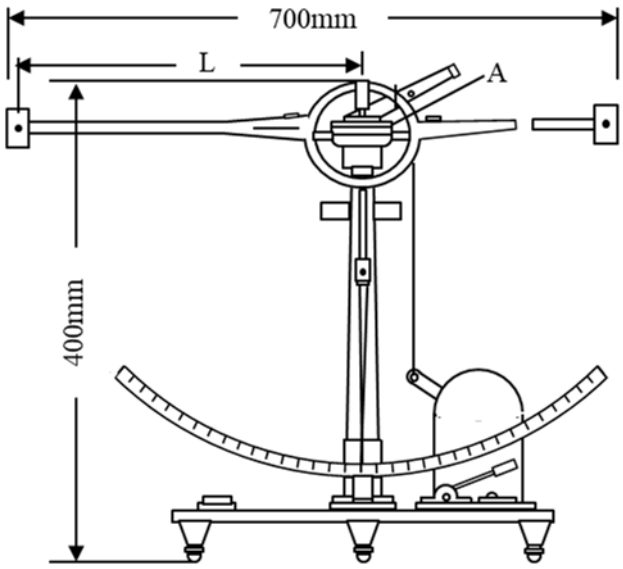

Figure 1.2.8 Configuration of the pendulum-type friction tester. The dynamic friction coefficient is calculated from the damping of the pendulum oscillation amplitude by the friction moment at the fulcrum of the pendulum.

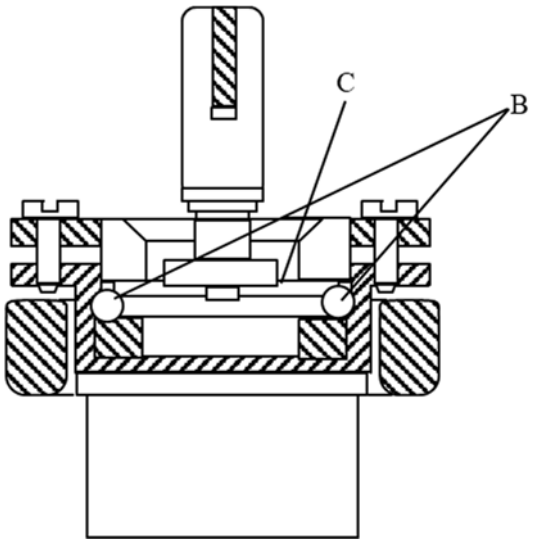

Figure 1.2.9 Fulcrum of the pendulum. Four balls (B) are fixed in an oil tank (A) by two, and a roller pin (C) fixed to the fulcrum of the pendulum is placed on the balls, and the testing machine is assembled so as to constitute four-point contact between the balls and the roller pins.

1.2.3 Ball on disk friction tester

Like the pendulum-type friction tester described in the previous subsection 1.2.2, a ball-on-disk tester is a typical tester for measuring the dynamic friction coefficient. Figure 1.2.10 shows the configuration of a ball-on-disk friction tester. The ball is set in a ball holder, and the holder is fixed to the tip of the arm. A disk is under the ball, and the sample is fixed on the disk. The arm is lowered, and the ball is pushed down to the position shifted from the rotation center on the sample. By attaching weights to the arm, the vertical load applied to the ball is adjusted. Then the disc is rotated, the arm is deflected in the horizontal direction by the frictional force between the ball and the sample. The deflection is detected by a displacement sensor to measure the frictional force. The dynamic friction coefficient is calculated by dividing the dynamic friction force by the normal load.

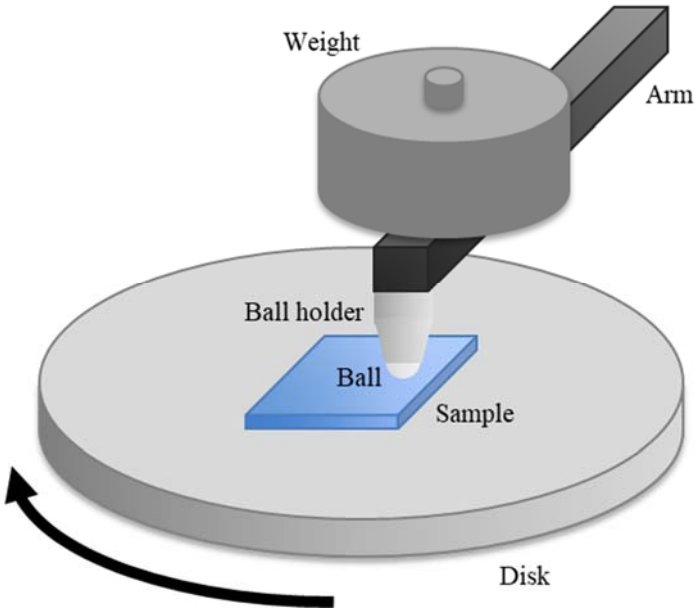

Figure 1.2.10 configuration of the ball-on-disk friction tester.

1.3 Reference

(1) Hardy, W. B.; Doubleday, I. Boundary Lubrication–The Paraffin Series. *Proc. Royal Soc. London., A*, 1922, 550–574.

(2) Allen, C. M.; Drauglis, E. Boundary Layer Lubrication: Monolayer or Multilayer. *Wear,* 1969, *14*, 363–384.

(3) Zhang, C. Understanding the wear and tribological properties of ceramic matrix composites. *In Advances in Ceramic Matrix Composites*, Ed. Low, I. M., 2014, Woodhead Publishing, 312–339.

(4) Grossiord, C.; Martin, J. M.; Mogne, T. L.; Palermo, Th. UHV friction of tribofilms derived from metal dithiophosphates. *Tribology Lett.*, 1998, *108-109*, 352-359.

(5) Grossiord, C.; Martin, J. M.; Mogne, T. L.; Palermo, Th. In situ MoS formation and selective transfer from MoDPT films. *Surface and Coatings Technology*, 1999, *6*, 171-179.

(6) Martin, J. M.; Grossiord, C.; Mogne, T. L.; Bec, S.; Tonck, A. The two-layer structure of Zndtp tribofilms Part I: AES, XPS and XANES analyses. *Tribology International*, 2001, *34*, 523-530.

(7) Martin, J. M.; Grossiord, C.; Mogne, T. L.; Igarashi, J. Transfer films and friction under boundary lubrication. *Wear*, 2000, *245*, 107-115.

(8) Martin, J. M.; Grossiord, C.; Mogne, T. L.; Igarashi, J. Combined in situ (ATR FT-IR) and ex situ (XPS) study of the ZnDTP-iron surface interaction. *Tribology Lett.*, 2003, *15-3*, 181-191.

(9) Feo, M. D.; Minfray, C.; Bouchet, M. I. De B.; Thiebaut, B.; Martin, J.M. MoDTC friction modifier additive degradation: Correlation between tribological performance and chemical changes. *RSC Adv.*, 2015, *5*, 93786-98796.

(10) Sahoo, R. R.; Biswas, S. K. Frictional response of fatty acids on steel. *Journal of Colloid and Interface Science*, 2009, *333*, 707-718.

(11) Lundgren, S. M.; Ruths, M.; Danerlöv, K.; Persson, K. Effects of unsaturation on film structure and friction of fatty acids in a model base oil. *Journal of Colloid and Interface Science*, 2008, *326*, 530-536.

(12) Buyanovskii, I. A. Boundary Lubrication by an Adsorption Layer. *Journal of Friction and Wear*, 2010, *31*, 33-47.

(13) Müller, T.; Yan, X.; Lee, S.; Perry, S. S.; Spencer, N. D. Lubrication Properties of a Brushlike Copolymer as a Function of the Amount of Solvent Absorbed within the Brush. *Macromolecuiles,* 2005, *38*, 5706–5713.

(14) Evans, K. O.; Biresaw, G. Quartz crystal microbalance investigation of the structure of adsorbed soybean oil and methyl oleate onto steel surface. *Thin Solid Films*, 2010, *519*, 900¬–905.

(15) Cann, P. M.; Spikes, H. A. In-Contact IR Spectroscopy of Hydrocarbon Lubricants. *Tribol. Lett.,* 2005, *19*, 289–297.

(16) Mangolini, F.; Rossi, A.; Spencer, N. D. Chemical Reactivity of Triphenyl Phosphorothionate (TPPT) with Iron: An ATR/FT-IR and XPS Investigation. *J. Phys. Chem.*, *C*, 2011 *115*, 1339–1354.

(17) Sasaki, K.; Inayoshi, N.; Tashiro, K. Development of new in situ observation system for dynamic study of lubricant molecules on metal friction surfaces by

two-dimensional fast-imaging Fourier-transform infrared-attenuated total reflection spectrometer. *Rev. Sci. Instrum.,* 2008, *79*, 123702.

(18) Bongaerts, J. H. H.; Day, J. P. R.; Marriott, C.; Pudney, P. D. A.; Williamson, A.-M. In situ confocal Raman spectroscopy of lubricants in a soft elastohydrodynamic tribological contact. *Appl. Phys. Lett.,* 2008, *104*, 014913.

(19) Watanabe, S.; Nakano, M.; Miyake, K.; Sasaki, S. Analysis of the Interfacial Molecular Behavior of a Lubrication Film of n-Dodecane Containing Stearic Acid under Lubricating Conditions by Sum Frequency Generation Spectroscopy. *Langmuir,* 2016, *32*, 13649–13656.

(20) Hirayama, T.; Torii, T.; Konishi, Y.; Maeda, M.; Matsuoka, T.; Inoue, K.; Hino, M.; Yamazaki, D.; Takeda, M. Thickness and density of adsorbed modifier layer on metal surface in lubricant by neutron reflectometry. *Tribol. Inernational,* 2012, *54*, 100–105.

(21) Wood, M. H.; Casford, M. T.; Steitz, R.; Zarbakhsh, A.; Welbourn, R. J. L.; Clarke, S. M. Comparative Adsorption of Saturated and Unsaturated Fatty Acids at the Iron Oxide/Oil Interface. *Langmuir,* 2015, *32*, 534–540.

(22) Hirayama, T.; Kawamura, R.; Fujino, K.; Matsuoka, T.; Komiya, H.; Onishi, H. Cross-Sectional Imaging of Boundary Lubrication Layer Formed by Fatty Acid by Means of Frequency-Modulation Atomic Force Microscopy. *Langmuir,* 2017, *33*, 10492–10500.

(23) Okubo, H.; Sasaki, S. Frequency-Modulation Atomic Force Microscopic Observation for Ultralow Frictional Solid–Liquid Interface of Diamond-Like Carbon in an Environmentally Friendly Oil. Tribology Lett., 2019, 67-3,.

(24) Bernat, S.; Armada, S.; Espallargas, N. Friction Mechanisms by Carboxylic Acids in Aqueous Lubricants. Tribology Lett., 2018, 66-83,.

(25) Dokukin, M. E.; Kuroki, H.; Minko, S.; Sokolov, I. AFM Study of Polymer Brush Grafted to Deformable Surfaces: Quantitative Properties of the Brush and Substrate Mechanics. Macromolecules, 2017, 50, 275‑282.

(26) Giessibl, F.J. Atomic Resolution of the Silicon (111)-(7x7) Surface by Atomic Force Microscopy Space. *Sience,* 1995, *267*, 68

(27) Fukui, K.; Onishi, H.; Iwasawa, Y. Atom-Resolved Image of the TiO2(110) Surface by Noncontact Atomic Force Microscopy. *Phys. Rev. Lett.,* 1997, *79*, 4202-4205

(28) Loppacher, Ch.; Bammerlin, M.; Guggisberg, M.; Meyer, E.; Güntherodt, H.-J.; Lüthi, R.; Schlittler, R.; Gimzewski, J.K. Forces with submolecular resolution between the probing tip and Cu-TBPP molecules on Cu(100) observed with a combined AFM/STM. *Appl. Phys.,* 2001, *A72*, S105-S108

(29) Fukuma, T.; Kobayashi, K.; Matsushige, K.; Yamada, H. True atomic resolution in liquid by frequency-modulation atomic force microscopy. *Appl. Phys. Lett.,* 2005, *87*, 034101

(30) Binnig, G.; Quate, C. F.; Gerber, Ch. Atomic Force Microscope. *Phys. Rev. Lett.,* 1986, *56*, 930

(31) Binnig, G.; Rohrer, H.; Gerber, Ch.; Weibel, E. Surface Studies by Scanning Tunneling Microscopy. *Phys. Rev. Lett.,* 1982, *49*, 57

(32) Binnig, G.; Rohrer, H.; Gerber, Ch.; Weibel, E. 7 × 7 Reconstruction on Si(111) Resolved in Real Space. *Phys. Rev. Lett.,* 1983, *50*, 120

(33) Kimura, K.; Ido S.; Oyabu, N.; Kobayashi, K.; Hirata, Y.; Imai, T,; Yamada, H. Visualizing water molecule distribution by atomic force microscopy. *J. Chem. Phys*., 2010, *132*, 194705

(34) Marutschke, C.; Walters, D.; Cleveland, J.; Hermes, I.; Bechstein, R.; Kühnle, A. Three-dimensional hydration layer mapping on the (10.4) surface of calcite using amplitude modulation atomic force microscopy. *Nanotechnology*, 2014, *25*, 335703

(35) Söngen, H.; Bechstein, R.; Kühnle, A.; Quantitative atomic force microscopy. *J. Phys.: Condens*. 2017, *29*, 274001

(36)Imada, H.; Kimura, K.; Onishi, H. Water and 2-Propanol Structured on Calcite (104) Probed by Frequency-Modulation Atomic Force Microscopy. *Langmuir*, 2013, *29*, 10744-10751

(37) Araki, Y.;Tsukamoto, K.; Takagi, R.; Miyashita, T.; Oyabu, N.; Kobayashi, K.; Yamada, H. Direct Observation of the Influence of Additives on Calcite Hydration by Frequency Modulation Atomic Force Microscopy. *Cryst. Growth Des.*, 2014, *14*, 6254-6260

(38) Sader, J E.; Jarvis, S P. Accurate formulas for interaction force and energy in frequency modulation force spectroscopy. *Appl Phys. Lett.*, 2004, *84*, 1801-1803.

Chapter 2 Poly-α-olefins containing phosphoric acid ester over sputtered iron films

2.1 Introduction

At the lubrication interface, the modifier molecules form a tribofilm on the solid surface and prevent direct contact between the solids, thereby contributing to reduction of friction and prevention of wear. Controlling the adsorption of modifier molecules on the solid surfaces is very important in improving the performance of lubricants.

In this chapter, a representative hydrocarbon lubricant in commerce, poly-α-olefin, is modified with different quantities of a phosphoric acid alkyl ester, one of frequently used modifiers as antifriction agent in real lubricants.[1] The antifriction agent forms a tribofilm of the reaction secondary product on the solid surface to prevent seizure and wear. The formed reaction coating is hard enough to be recognized as a solid and can be analyzed with a conventional AFM/SPM. However, the precursor adsorption film formed by the physical or chemical adsorption of modifier molecules on the solid surface as a preliminary step for this reaction was so soft and required the force sensitivity of the order of 10 pN achieved in FM-AFM to detect the layer induced force response. The presence or absence of modifier layers are probed on iron films using FM-AFM. The vertical as well as lateral distribution of the layers is visualized by mapping layer-induced force on the probing tip. Furthermore, the dynamic friction coefficient of steel–lubricant–steel interfaces is separately determined with a friction tester. The macroscopic friction property as a function of modifier quantity is compared with the nanometer-scale distribution of the modifier layers.

2.2 Materials

2.2.1 Lubricants

Non-polar poly-α-olefin (PAO) was modified with orthophosphoric acid oleyl ester (C18AP). The chemical structure of the two compounds is illustrated in Figure 2.2.1. PAO (Ineos, Durasyn164) containing decene trimers ($C_{30}H_{62}$) as the major component was purified with activated clay. The purified liquid possessed a dynamic viscosity of 4 mm^2 s^{-1} at 100 Cº. C18AP (Johoku Chemicals, JP-518) was a 1:1 mixture of the monoester and diester of the phosphoric acid. The modifier concentration was adjusted at 0.2, 2, 20, and 200 ppm to simulate that in real lubricants, ca. 200 ppm.

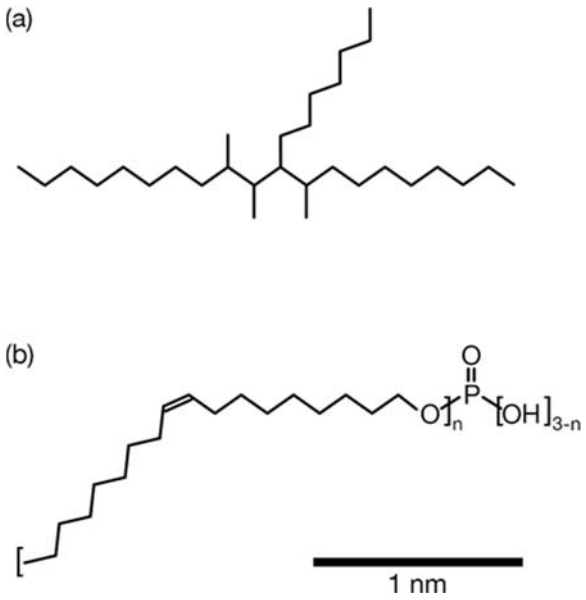

Figure 2.2.1 Lubricant. (a) decene trimer as the major component in the poly-α-olefin (PAO) used in this study. The longest (C_{20}) alkyl chain is depicted in the all-*trans* conformation. (b) orthophosphoric acid oleyl ester with *n*=1 or 2 (C18AP).

2.2.2 Iron films

Metallic iron was sputtered on silicon wafers to produce 50-nm thick films. The films were naturally oxidized in air at RT. Highly oriented pyrolytic graphite was compared with the iron films as a benchmark of solid with little or no chemical affinity to the phosphoric acid ester. Figure 2.2.2 presents the topographic images of the iron films observed in water. The scanning area is 500nm × 500nm, and bright colors represent higher parts and dark colors show lower parts. The surface roughness of the iron oxide film has Ra value is about 1.4 nm and Rz value is about 18 nm, which is flat enough to evaluate the interface between lubricants and the iron oxide.

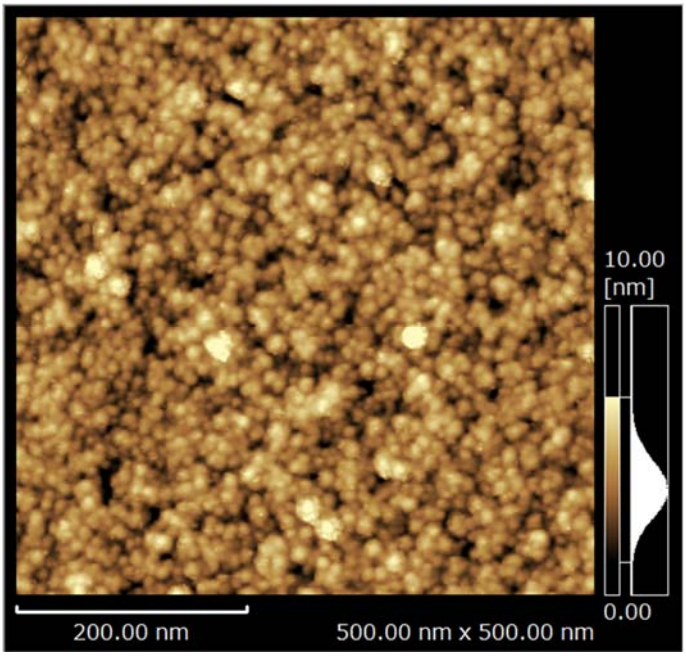

Figure 2.2.2 The topographic images of the iron films observed in water. The surface of the iron oxide film is flat enough to evaluate the interface between lubricants and the iron oxide.

2.3 Results and discussion

2.3.1 Analysis by FM-AFM

2.3.1.1 Methods

Frequency-modulation detection of force on the probing tip was enabled with a SPM-8100FM microscope (Shimadzu). In topographic imaging of iron films, the resonance oscillation of a silicon cantilever (Nanoworld, PPP-NCHAuD) was mechanically excited with a piezo-actuator. The nominal spring constant of the cantilevers was 42 N m^{-1}. The oscillation amplitude was regulated at a preset amplitude (A). When a lubricant-induced conservative force was loaded on the tip, the resonance frequency of cantilever oscillation (f) shifted accordingly. The topography of the scanned film was traced with regulation of the tip–surface distance by keeping the frequency shift (Δf) at a prefixed setpoint. The resonant frequency of the cantilevers was 100–140 kHz, and the quality factor of oscillation resonance was 2–3 in the lubricants. A typical spectrum of thermally induced cantilever oscillation is shown in Figure 2.3.1. Observed spectral density is presented with dots, and a Lorentzian function fitted the observed data was shown in red line. The application of the Lorentz function to the observed spectral density is described in detail in Section 2.7.1. An iron film or graphite wafer was fixed in a quartz petri dish placed on the microscope stage driven by a piezoelectric scanner. The dish was filled with the lubricant of 500 μl and then the cantilever assembly was put on top. Imaging scans were conducted at RT.

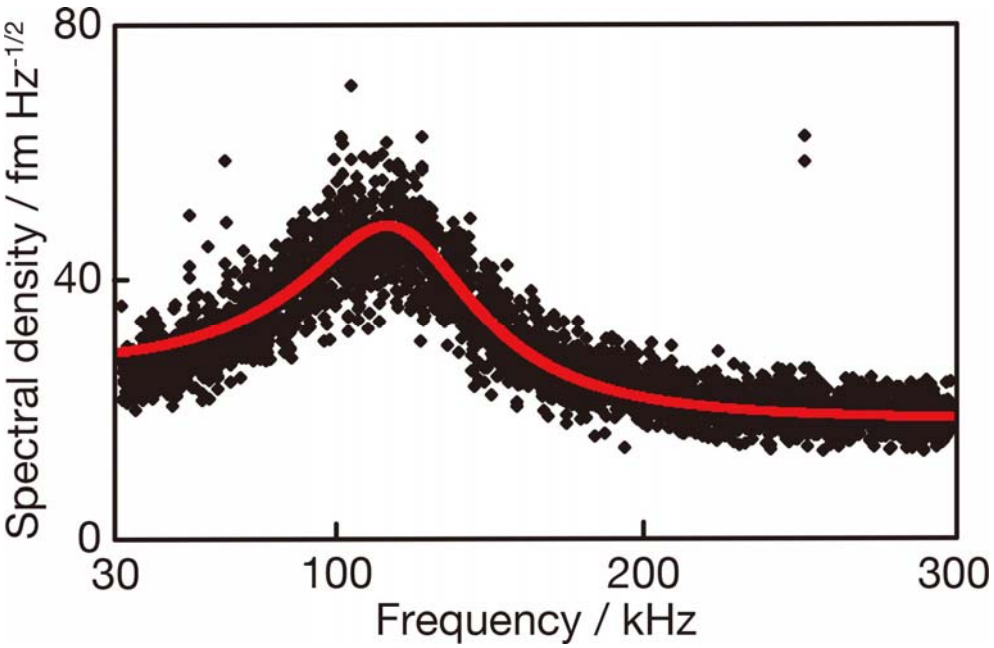

Figure 2.3.1 A typical spectrum of cantilever oscillation in PAO. Observed spectral density is presented with dots. A Lorentzian function (red line) fitted the observed data with a quality factor of 2 and a background spectral density of 18 fm $Hz^{-1/2}$

2.3.1.2 Iron film topography

Figure 2.3.2 presents the topographic images of the iron films observed in (a) pure PAO and (b) PAO containing 200 ppm of C18AP, which was the highest concentration evaluated in this study. The spherical grains were recognized in the images. The lateral and vertical dimensions of the grains were between 5 and 20 nm and between 1 and 3 nm, respectively. The grain sizes were identical in both the films. However, the grain topography was sharper in image (a) as compared with image (b) in Figure 2.3.2. The reduced sharpness in image (b) could not be attributed to the different shapes of the probing tip, although different cantilevers were used for acquiring the two topographic images. A second set of images that were obtained in the presence and absence of C18AP is shown in Figure 2.7.1 in the Supporting Information. The grains in the C18AP-containing lubricant again exhibited features with reduced sharpness.

The reproducible results suggest that the iron films were most likely covered by soft material such as adsorbed C18AP, which resulted in the grain topography being less sharp than that of the uncovered films. A magnified view of a portion of the topographic image is shown above each image to be easily able to compare the sharpness of the grain contours between the images.

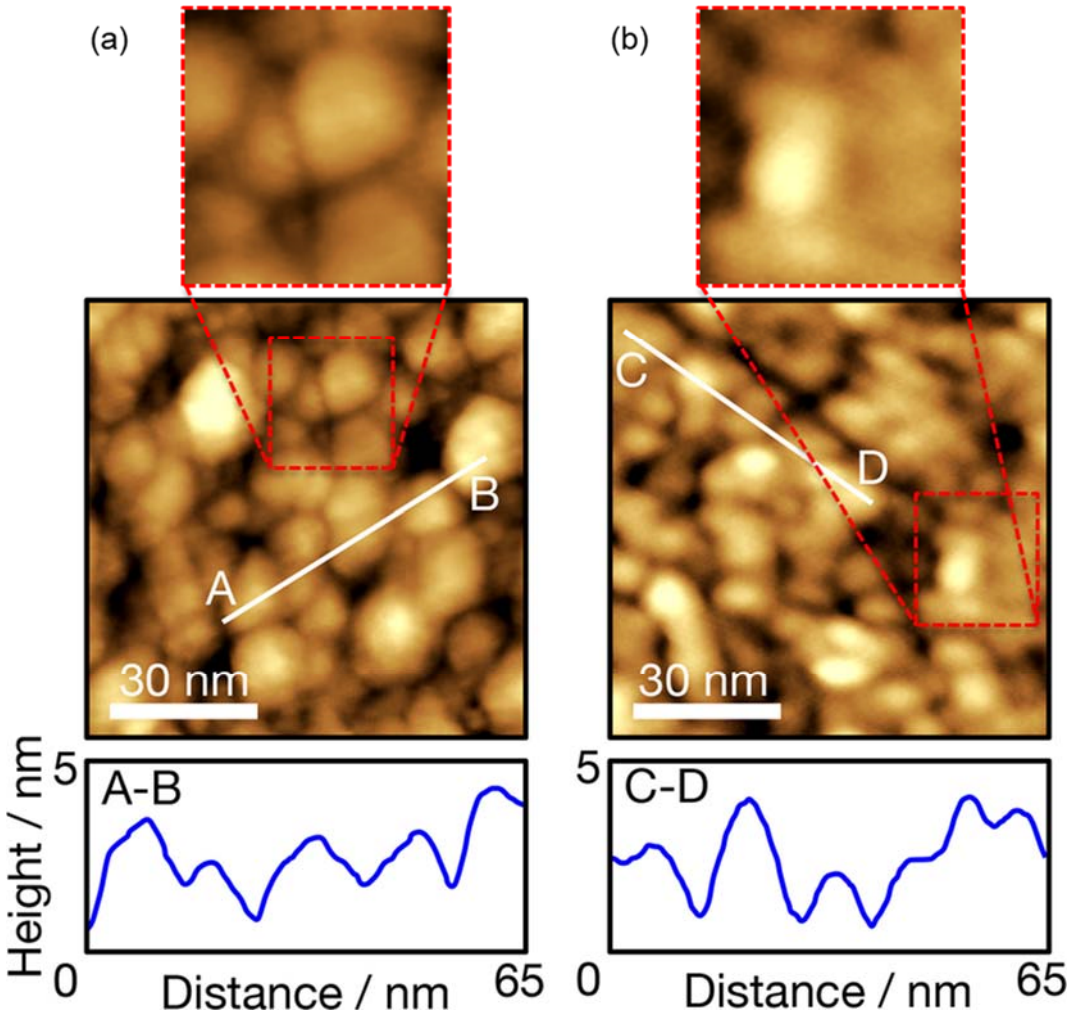

Figure 2.3.2 The topography of the iron films observed in the lubricants. The concentrations of C18AP were (a) 0 and (b) 200 ppm. Image size: 90 nm^2, peak-to-peak amplitude of cantilever oscillation: 2.0 nm, and frequency-shift set point: +83 Hz. The cross sections determined along the A-B and C-D lines are shown in the corresponding lower panels.

2.3.1.3 Force mapping

The difference in the topographic sharpness seen in Figure 2.3.2 suggests that the C18AP layers were deposited on the iron films. In the presence of C18AP on the films, the phosphoric acid end should be in contact with the naturally oxidized iron films, with an expansion of the $C_{18}H_{35}$ chains into the lubricant liquid. In this subsection, the mechanical response of the expanding chains is probed and mapped on the planes that are perpendicular to the iron films to verify C18AP deposition.

Figure 2.3.3 shows the frequency-shift maps that were observed in the lubricants containing different concentrations of C18AP. The oscillating cantilever was scanned vertically from the bulk lubricant to the iron film. The frequency shift as a function of the vertical coordinate was simultaneously recorded to obtain one frequency shift-distance curve composed of 250 pixels at one lateral position. We aborted the vertical scan when frequency shift reached a predetermined threshold (+600 Hz for the acquired maps in Figure 2.3.3); the cantilever was retracted into the lubricant by 10 nm to prevent extensive tip-to-surface contact. We repeatedly acquired 256 or 512 vertical scans along a 20 nm long lateral coordinate. One frequency-shift map was subsequently constructed on a plane perpendicular to the iron film with an acquisition time of 26 (51) seconds for 256 (512) scans per frame.

The observed frequency-shift map can be considered to be an approximate distribution of the lubricant-induced repulsive force on the tip. A repulsive force causes a positive frequency shift, though the relation between the force and frequency shift is nonlinear.[2] A large (small) value of frequency shift is denoted by a bright (dark) blue color in Figure 2.3.3, while areas outside the scanned range are shown in black. The brightest region at the base of each map represents the boundary between the lubricant liquid and iron film. The repulsive force on the tip increased

monotonically when it was moved deeper into this region, signifying tip-to-surface contact. The envelope of the brightest region was corrugated to trace the topography of the iron films. The lateral and vertical dimensions of the corrugation were typically 10 nm and 1–2 nm, respectively. The corrugations along these dimensions were consistent with the topographic images shown in Figure 2.3.2.

The frequency shift, *i.e.*, the force on the tip, was uneven in the vicinity of the iron film. Fourteen frequency shift-distance curves were obtained between the two dashed lines and averaged, as shown in the upper right panel of Figure 2.3.3. The zero tip-to-surface distance in the frequency shift-distance curve was defined at the coordinate of the vertical tip where frequency shift exceeded the threshold, +600 Hz. The averaged frequency shift-distance curve was then converted to a force-distance curve using the Sader-Jarvis formula[2] and is shown in the lower right panel of Figure 2.3.3. The signal-to-noise ratio in the converted curve showed a force sensitivity on the order of 10 pN in the PAO.

It was technically not easy to average the whole set of frequency shift curves in a map. The iron film surface, where tip-surface distance was defined to be zero, was not flat. The vertical scans were aborted in force mapping when frequency shift exceeded the preset value. However, the force on the tip was not constant at the aborted positions since the force is given by a weighed integration of frequency shift as formulated by Sader and Jarvis.[2] We recognized by visual inspection that the feature in the cross sections was almost homogeneous along the lateral coordinate even on the corrugated film surface. On this recognition, averaging a limited number of frequency shift curves, 14 curves in Figure 2.3.3, provided a reasonable way to improve the statistical reliability of representative curves on the examined interface.

Alternating dark and bright layers appeared in the map (Figure 2.3.3(a)) when we used pure PAO, suggesting that the film was covered by two or three PAO liquid layers. The distance between the neighboring maxima in the corresponding force curve was in a range of 0.6–0.7 nm. The liquid PAO layers were suggested to be separated by this distance over the iron film. The liquid-induced force pushing or pulling the tip apex is attributed to the local liquid density, though force–density relation is not straightforward. In a solvent-tip approximation,[3,4] the liquid molecules surrounding the apex generate the force in the form of free-energy gradient.

Liquid layers separated by 0.6–0.7 nm have been found in the force maps of organic liquids and assigned to the linear hydrocarbon chains that lie flat over the solid surface. *n*-Dodecane and *n*-hexadecane liquid in contact to a CH_3-terminated thiolate monolayer resulted in liquid layers separated by 0.56–0.58 nm.[5] *n*-Hexadecane exhibited a layer-to-layer distance of 0.6 nm and 0.6–0.4 nm on Cu films[6] and graphite wafers,[7,8] respectively. Oxygenated chains such as *n*-decanol,[9,10] *n*-dodecanol,[11] and tetraglyme ($CH_3(OCH_2CH_2)_4OCH_3$)[12] produced liquid layers separated by 0.5–0.6 nm on graphite. The carbon chain branching of the PAO used in this study is illustrated in Figure 2.2.1. The branched chain showed a layer-to-layer distance (0.6–0.7 nm) that was slightly larger than that observed in the linear-chain compounds mentioned above (0.4–0.6 nm). This result is not surprising as a heavily branched hydrocarbon such as 2,6,10,15,19,23-hexamethyltetracosane (squalane) has previously produced liquid layers separated by 0.6 nm on graphite.[13] A recent AFM study[14] reported averaged layer distances of 0.42 and 0.47 nm in a larger PAO, decene tetramers, on graphite and steal, respectively.

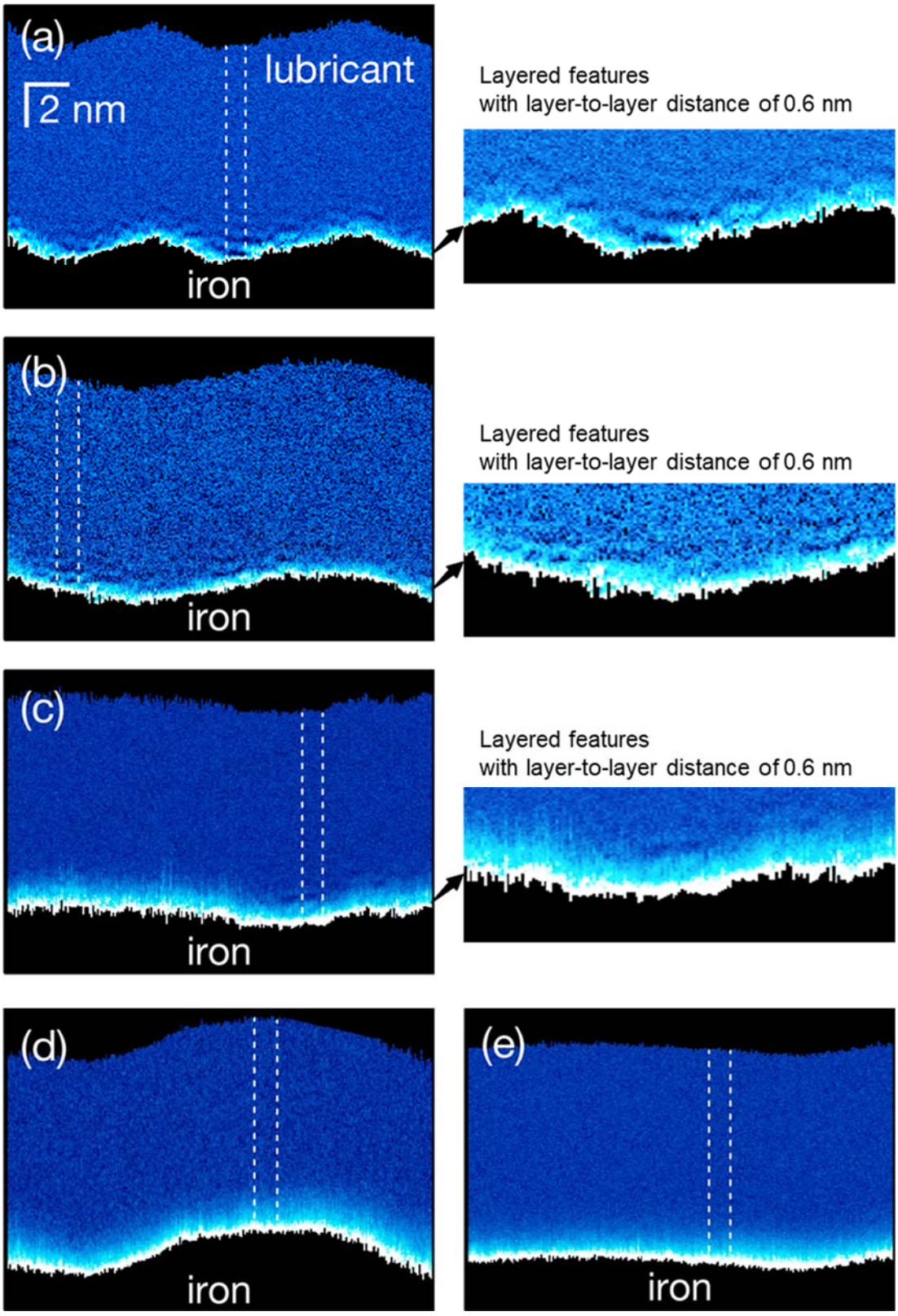
(a)
lubricant
2 nm
iron
Layered features
with layer-to-layer distance of 0.6 nm
(b)
iron
Layered features
with layer-to-layer distance of 0.6 nm
(c)
iron
Layered features
with layer-to-layer distance of 0.6 nm
(d)
iron
(e)
iron

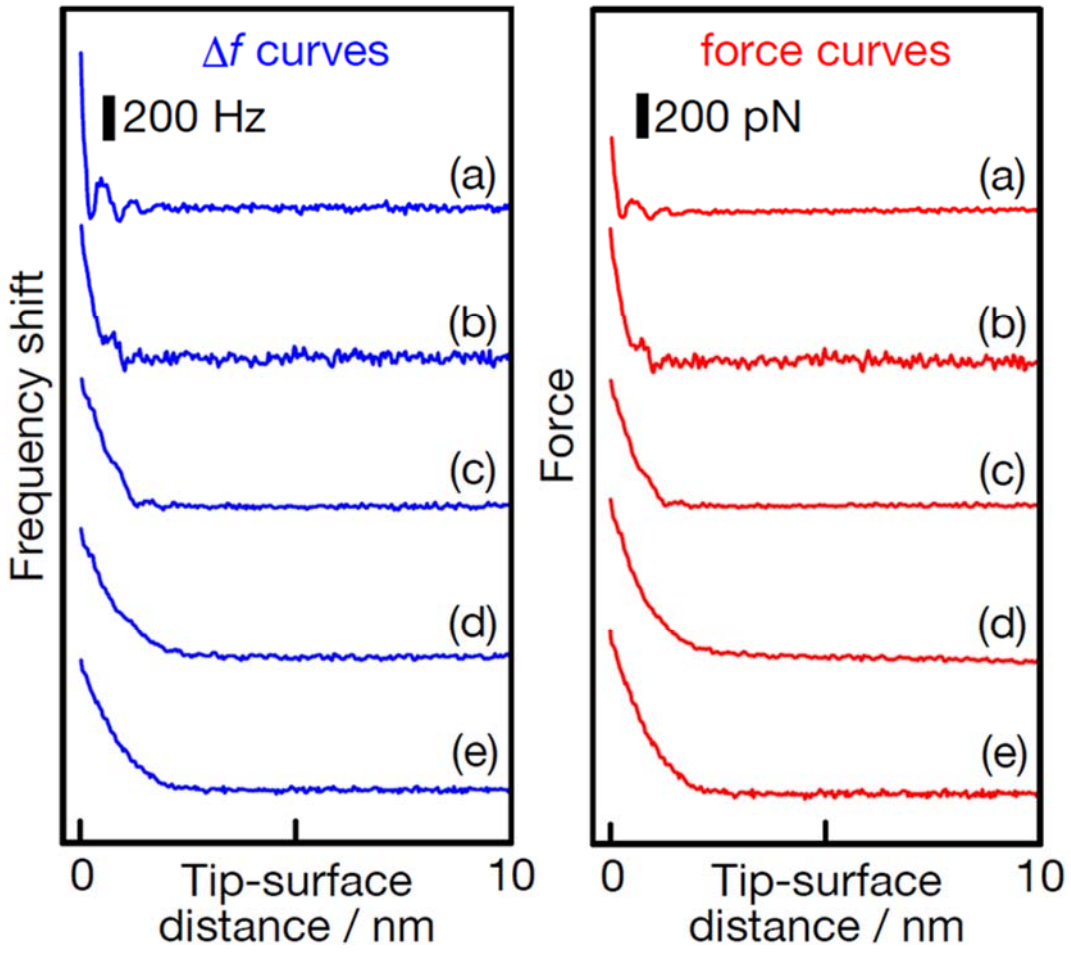

Figure 2.3.3 Lubricants over the iron films. The cross-sectional frequency shift distribution was mapped on a plane that was perpendicular to the film surface in the lubricants containing C18AP at (a) 0, (b) 0.2, (c) 2, (d) 20, and (e) 200 ppm. The amplitude of the cantilever oscillation was 0.4 nm. The aspect ratio of the lateral and vertical scales has been tuned unity in the maps. A large (or small) positive frequency shift is depicted using a bright (or dark) blue color. Fourteen frequency shift-distance curves situated between the two dashed lines were averaged, with the results shown in the left panel. The averaged frequency shift-distance curves were converted to force–distance curves as depicted in the right panel.

The layered force distribution weakened and in cases even disappeared when C18AP was added to PAO. The PAO layers intermittently remained in the map (Figure 2.3.3(b)) at a C18AP concentration of 0.2 ppm, while the layered feature almost disappeared in the map (Figure 2.3.3(c)) at a concentration of 2 ppm. The repulsive force on the tip monotonically decayed with increasing tip-to-surface distance in the areas where the layered feature disappeared. Here, the laterally heterogeneous layers of the lubricant modifier were visualized on a nanometer-scale resolution in space. The layered structure was completely removed by adding C18AP concentrations of 20 and 200 ppm, as shown in the maps in Figures 4(d) and (e). Multiple frequency-shift maps obtained to confirm that the layered structure was completely removed by adding C18AP concentrations of 20 and 200 ppm were shown in Figure 2.7.2 and Figure 2.7.3 in the Supporting Information, respectively.

The monotonically decaying force component increased with an increase in the C18AP concentration. The decay length, which was defined as the tip-to-surface distance resulting in zero force, was estimated to be 0.6, 0.9, and 2.0 nm corresponding to C18AP concentrations of 0.2, 2, and 20 ppm, respectively. A further increase in the concentration to 200 pm caused little extension in the decay length. This resulted in the two force curves at 20 and 200 ppm being identical. The identical force curves were a reflection of the C18AP layer that fully covered the iron films. Here we assume that the acid esters were anchored at the phosphoric acid end on the naturally oxidized iron films. Each adsorbed C18AP contains one or two $C_{18}H_{35}$ chains that extend into the lubricant liquid. The chains could not be as closely packed like the alkyl chains of alkylthiolates on a gold film because the C18AP used in this study was a mixture of the monoester and diester. The loosely packed chains have to be flexible and fluctuating in the lubricant. The force on the tip was fluctuating when

it was in contact with a fluctuating chain. The accumulation time at each vertical coordinate was typically 30 μs in our force mapping scans. Hence, the observed frequency shift represented the time-averaged force on the tip, and in turn reflected the time-averaged density distribution of the fluctuating chains. The observed curves decayed to zero force at a tip-to-surface distance of 2.0 nm at high C18AP concentrations. This distance is consistent with the $C_{18}H_{35}$ chain length depicted in Figure 2.2.1, wherein the two terminal carbon atoms are separated by 1.9 nm. The observed length saturated at 2.0 nm, which suggests that there was a monomolecular C18AP layer on the iron films. The under saturated layers generated at 0.2 and 2 ppm exhibited short decay lengths. The $C_{18}H_{35}$ chains in the unsaturated layers can be tilted to enable contact with the film surface to gain van der Waals energy. The tilted chains presented thin layers.

The molecular behavior of the lubricants estimated from the frequency-shift map is illustrated in Figure 2.3.4. The illustration of a molecule colored in yellow was drawn assuming that the molecule has an all-trans formation. In the case of all-trans, if the molecular structure of PAO is viewed sideways, it is the same as that of a single-chain hydrocarbon, such as hexadecane. Therefore, it is no wonder that PAO molecules form layer structure with layer-to-layer distances of 0.6-0.7 nm. In practice, however, there may be other forms than all-trans, and various forms may coexist. There is an energy difference of 0.8 kcal/mol (= 3kJ/mol) between all-trans formation and gauche formation of butane[15]. The thermodynamic behavior of molecules can be expressed by the Boltzmann distribution, so if the energy in the case of all-trans is E and the temperature is 300K, then the abundance ratio of all-trans to gauche can be calculated as follows.

$$\frac{\textbf{all trans}}{\textbf{gouache}} = e^{-\frac{E}{R\times 300}} \div e^{-\frac{E+3000}{R\times 300}} = e^{\frac{3000}{R\times 300}} = \mathbf{4.36} \qquad 2.3.1$$

Where R is molar gas constant, $R = 8.314 \left[\frac{J}{Kmol}\right]$

According to this result, in case of butane, all-trans accounts for 80% and gauche accounts for 20% in lubrication oil at 300K, the number of molecules forming the all-trans in the lubricating oil was not so large. In PAO, the abundance ratio of all-trans formation decreases because there are more c-c bonds than in butane. On the other hand, there is an experimental fact that the layer-to-layer distances were 0.6-0.7 nm. The moving velocity of the molecules relative to the scanning velocity of FM-AFM is overwhelmingly fast, so that the time-averaged information appears in the frequency-shift maps. Therefore, the layered feature with layer-to-layer distances were 0.6-0.7 nm suggests that many of the PAO molecules took the all-trans formation at that moment. There are several other examples in which liquid molecules lie parallel to the solid surface[8, 16]. Molecules with structures that generate chemical bonds with the solid surface, such as carboxylic acids and phosphates, may stand upright on the solid surface, but molecules without such structures are oriented to maximize the area of contact with the solid per molecule to increase the stability of each molecule. In the second layer, the molecules are oriented so as to maximize a contact area per molecule between molecules constituting the first layer and molecules constituting the second layer. In this repetition, a plurality of layers is formed. For this reason, it is predicted that molecules took all -trans formation in order to maximize the area of contact with the solid or the other molecules. The reason why the PAO molecule having a three-dimensional structure forms a layered structure having an interlayer distance of 0.6-0.7 nm is the same.

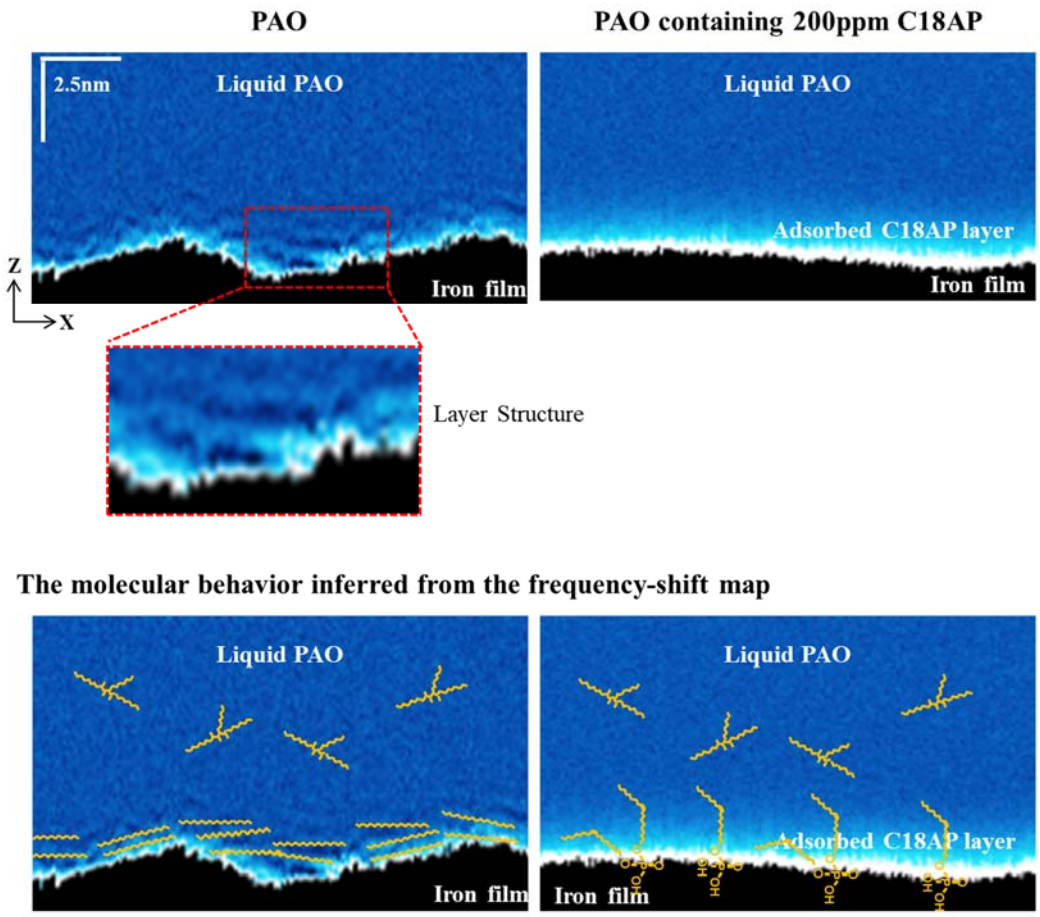

Figure 2.3.4 The molecular behavior estimated from the frequency-shift map

The alkyl chains in the alkylthiolate monolayers prepared on a gold film were closely packed to solidify the monolayers. The solidified monolayer created a static boundary with the organic solvents that could be traced during topographic imaging with FM-AFM.[5] We assume that the C18AP layers on the iron films were not solidified. Force mapping facilitated the quantification of the vertical and lateral distribution of the C18AP layers having a fluctuating, dynamic boundary with the liquid PAO. Fukuma and coworkers demonstrated the feasibility of AFM-based force mapping for estimating the time-averaged density distribution of the lipid head groups[17] and biofouling-resistant moieties[18] in water. Hirayama et al.[6] extended their method to include a hexadecane-based model lubricant that is more viscous than

water. In an earlier study by Moustafa et al.,[19] a bimodal AFM was exploited to visualize the lateral distribution of weakly adsorbed organic aggregates over graphite surfaces. Our present study provided the lateral and vertical distribution of the ester modifiers in the poly-α-olefin liquid.

A recent mapping study on a liquid ester lubricant with no modifier[20] reported the deposition of soft layers on a diamond-like carbon film following rubbing in a friction test, which was most likely a result of the tribochemical reactions of the lubricant. In the present study, the modifier distribution in a real lubricant was observed. The relation between the observed distribution of the modifier and the macroscopic friction property is examined in the final section of this paper.

Force mapping in the lubricants was further examined using graphite wafers to support the interpretation of C18AP layer deposition on the iron films. Graphite was considered to have little chemical affinity to the phosphoric acid ester. Figure 2.3.5 shows the frequency-shift maps that were observed in the absence and presence of C18AP. The freshly cleaved graphite wafer showed atomically flat terraces in the topographic images (not shown). The map (Figure 2.3.5(a)) captured in pure PAO shows that the envelope of the brightest colored region, which represents the physical topography of the wafer, was straight as expected. Three liquid layers appeared with layer-to-layer distances of 0.6–0.7 nm. The layered PAO liquid was seen both on the graphite and iron films. Figure 2.3.5(b) shows the frequency-shift map acquired in the presence of C18AP at 200 ppm. Three bright layers parallel to the graphite surface were still identifiable, indicating that the lubricant liquid was directly exposed to the graphite. The force mapping results shown in Figures 2.3.3 and 2.3.5 support our interpretation that the iron film was partially or fully covered by the C18AP layers depending on the concentration of C18AP in the bulk lubricant.

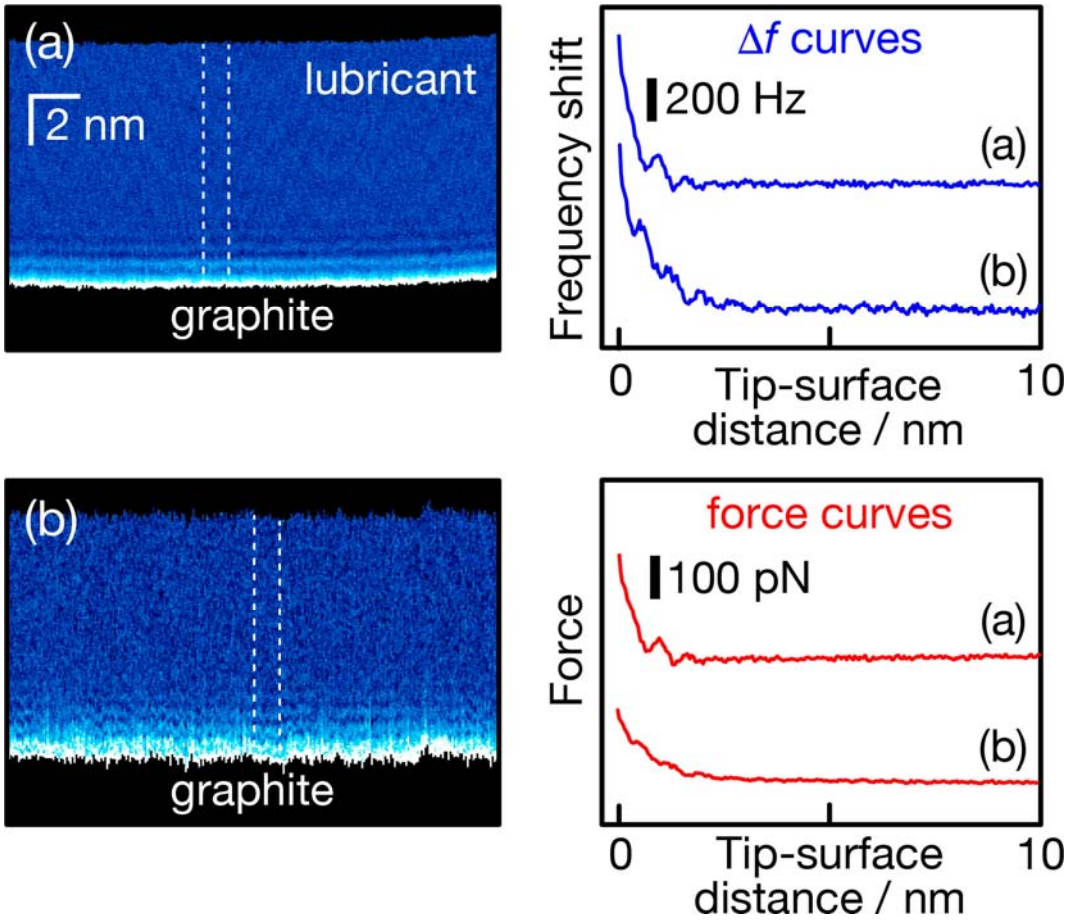

Figure 2.3.5 Lubricants over graphite. The frequency-shift maps were obtained for the lubricants with C18AP concentrations of (a) 0 and (b) 200 ppm. Fourteen frequency shift-distance curves situated between the two dashed lines were averaged, with the results shown in the upper right panel. The averaged frequency shift-distance curves were converted to force-distance curves, as depicted in the lower right panel. The cantilever oscillation amplitude: (a) 0.6 nm and (b) 0.4 nm.

In addition to the layered feature, a monotonically decaying force was to a limited extent identified in the C18AP-containing lubricant. The decay length was estimated to be ca. 2 nm though overlapped with the oscillatory force. A limited amount of C18AP might have been adsorbed on the graphite surface and/or the probing tip apex to produce the monotonically decaying force overlapping the oscillatory force coming

from PAO layers. Comparing ordinary silicon tips with tips coated or made of carbonaceous materials would be functional to interpret the monotonically decaying force recognized on graphite.

2.3.2 Evaluation of the friction coefficient by a pendulum-type friction tester

2.3.2.1 Methods

The dynamic friction coefficient at the sliding steel–lubricant–steel interfaces was evaluated using a pendulum-type friction tester (Narita Seiki).[21] A steel pendulum was freely oscillated with the fulcrum dipped in the lubricant (See the table of contents graphic). One oscillation was typically completed in 4 s. The amplitude of the pendulum oscillation was dampened because of the lubricated friction on the fulcrum. The initial amplitude A_0 was set at 0.5 radian, and the decayed amplitude A_k was recorded on the basis of the number of completed oscillations k until $A_k \leq 0.1$. The friction coefficient μ, which was averaged over one measurement ranging from A_0 to A_n, can be expressed by Equation 2.3.2:

$$\boldsymbol{\mu = C \times \frac{\sum_{k=1}^{n}(A_0 - A_k)}{\sum_{k=1}^{n} k}} \qquad 2.3.2$$

where n is the number of recorded oscillations in each measurement run. Using our tester, we calibrated the constant C to 3.2 according to the pendulum length and weight of the fulcrum. The friction coefficient increased with repeated oscillation cycles. Hence, a maximum of 20 measurement runs was conducted to trace the time course of the coefficient. The experiment with the pendulum-type friction tester was conducted by Teppei Tsujimoto of JXTG Nippon Oil & Energy Corporation.

2.3.2.2 Friction coefficient at different modifier concentrations

Figure 2.3.6 shows the evaluated coefficients in the lubricants containing C18AP concentrations of 0, 2, 20, and 200 ppm. The raw amplitudes A_k recorded in the individual runs are reported in Table 2.7.1, Table 2.7.2, Table 2.7.3, and Table 2.7.4

in the Supporting Information. The coefficient for pure PAO was 0.11 in run 1, rapidly increased to 0.34 in runs 4 - 13, and continued to increase up to 0.40 in runs 14–20. The friction increased with the sliding cycles in the modifier-free PAO, which resulted in the adhesion of the sliding steel surfaces. The coefficient for a C18AP concentration of 2 ppm similarly increased in runs 1 - 13 and subsequently remained constant between 0.33 and 0.34 in runs 14 - 20. The limited amount of C18AP caused a noticeable change in the friction at the sliding interface. The friction further decreased when the C18AP concentration increased to 20 ppm. The initial coefficient (0.12) was constant until run 5, increased in runs 6 - 17, and remained almost constant between 0.26 and 0.28 in runs 18 - 20. The addition of C18AP at 200 ppm, which was the largest concentration investigated, stabilized the coefficient between 0.11 and 0.10 in runs 1 - 10. The stable, low friction that was observed at this concentration is characteristic of the lubricants that have been successfully modified with polar compounds.

Compare the macroscopic friction results with the nanometer-scale force mapping results described in the previous section. In the absence of the modifier, layered PAO liquid was present on the iron film. The steal surfaces sliding in the fulcrum should also have been exposed to PAO and hence adhered. The time course of the friction coefficient was modified partially at a lower concentration (2 ppm), at which concentration the layered PAO feature almost disappeared in the force map on the film. The force map at 20 ppm showed a full coverage of the C18AP monolayer on the film. The macroscopic friction decreased in the lubricant with this modifier concentration. The force map was insensitive to further addition of C18AP, while the friction coefficient still descended at 200 ppm.

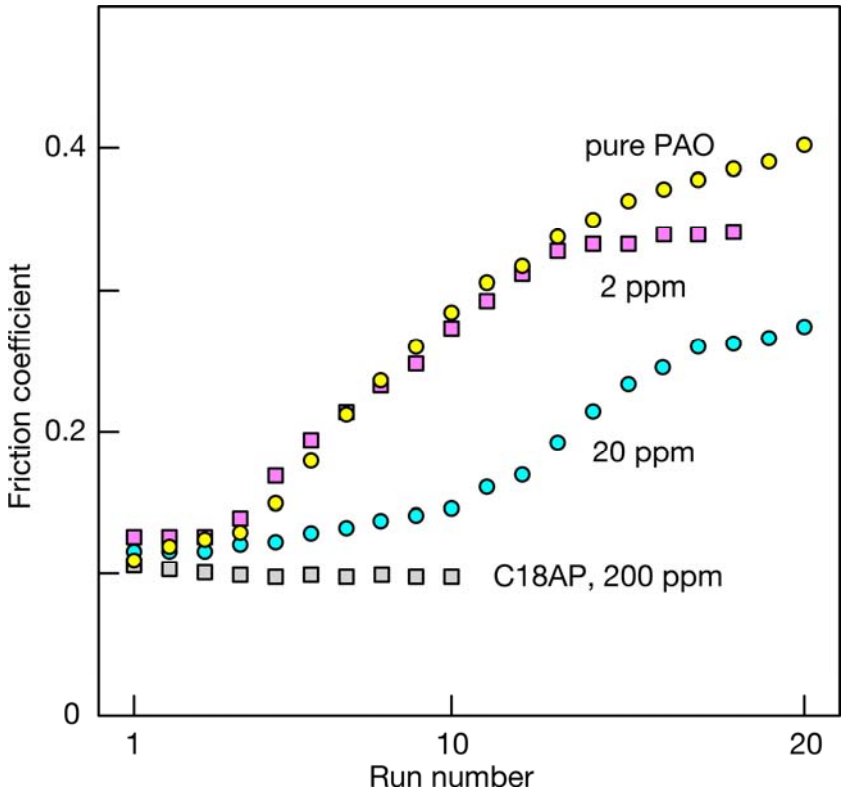

Figure 2.3.6 The friction coefficient of the steel–lubricant–steel interfaces that were evaluated using a pendulum-type friction tester. Lubricants containing C18AP concentrations of 0, 2, 20, and 200 ppm were tested.

The following Langmuir adsorption isotherm is used as one of the isothermal adsorption equations[22].

$$\boldsymbol{\theta = \frac{Kc}{1 + Kc}} \qquad 2.3.3$$

where θ is coverage, K is equilibrium constant and c is concentration of the modifier. This equation is derived on the basis of the following assumptions.

1. There are uniform adsorption sites on the solid surface, and only one molecule is adsorbed at each adsorption site.
2. Consider only monolayer adsorption.
3. There is no interaction between the adsorbed molecules.

4. The heat of adsorption does not depend on the coverage of modifiers on the solid surface.

Figure 2.3.7 (a) shows the graph where the horizontal axis represents concentration, the vertical axis represents coverage, and K is 1, 3, 5, 10, 20 ppm^{-1}, respectively. Figure 2.3.7 (b) shows an enlarged view of the area where the concentration ranges from 0 to 200 ppm. Each concentration (0.2 ppm, 2 ppm, 20 ppm, 200 ppm) examined in this study was indicated by a dashed red line and red circle in Figure2.3.7. Both experiments with FM-AFM and the pendulum-type friction tester in this study showed that C18AP was scarcely adsorbed at a concentration of 0.2 ppm, partially adsorbed at 2 ppm and the surface was completely covered with C18AP monolayer at 20 ppm and 200 ppm. Assuming that the adsorption of C18AP on the iron oxide film follows Langmuir adsorption isotherm, if K is 1 ppm^{-1}, the coverage at concentration of 2 ppm and 20 ppm is too small. And if K is 10 ppm^{-1} or 20 ppm^{-1}, the coverage at concentration of 2 ppm is too large. From the adsorption state at each concentration used in this study, K was estimated to be about from 3 ppm^{-1} to 5 ppm^{-1}.

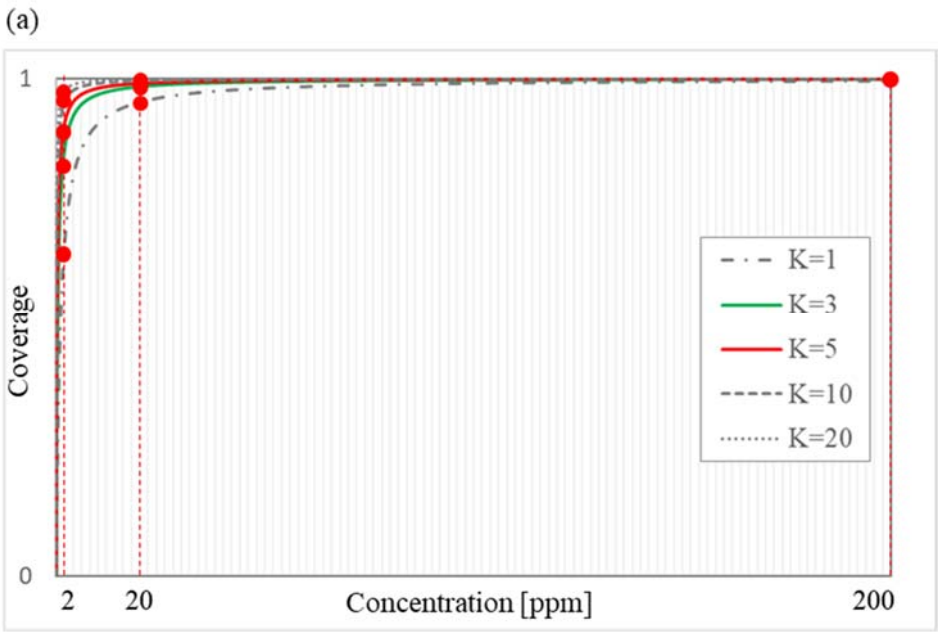

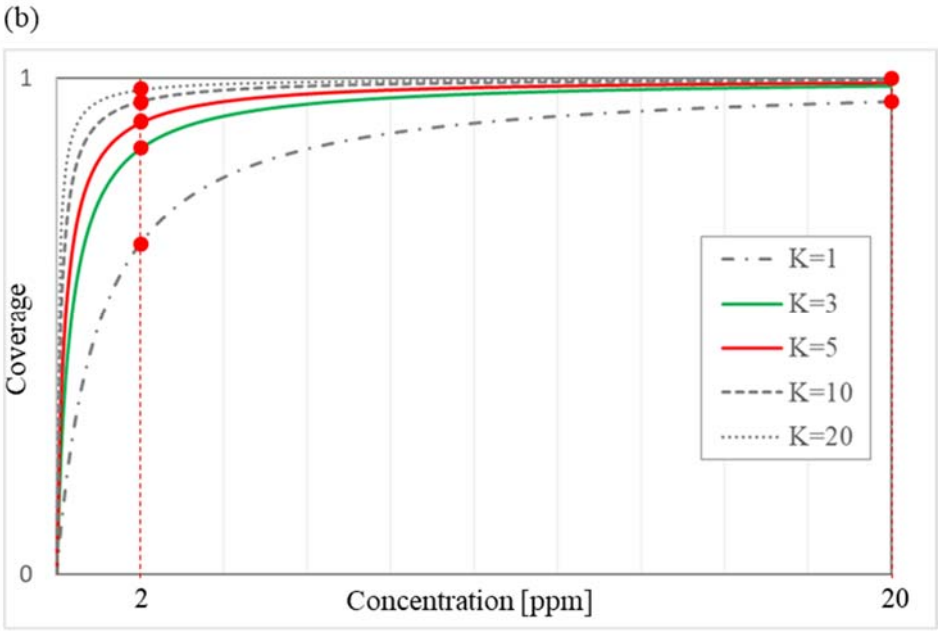

Figure 2.3.7 Graph with concentration on the horizontal axis and coverage on the vertical axis drawn from Langmuir adsorption isotherm. The equilibrium constant K is assumed to be 1, 3, 5, 10, 20 ppm^{-1}, respectively.

We infer that the two sets of experimental results are qualitatively related, even though one was observed at the sliding steel–lubricant–steel interface and the other at the static lubricant–iron boundary. A C18AP monolayer that completely covers the surface of a solid in a static environment is a requirement for the modification of the friction property in the sliding condition. The excess modifier in the bulk lubricant may have been additionally required to produce phosphorus-containing tribolayers on the sliding fulcrum interface, leading to the stable low friction achieved at 200 pm.

Our approach that proposes force mapping with FM-AFM provides a unique opportunity for characterizing modifier-containing lubricants. The presence of PAO-induced layers indicates that the solid surface under investigation was directly exposed to the lubricant. The surface was covered with flexible moieties of the modifier fluctuating in the lubricant liquid when the force on the probing tip

monotonically decayed as a function of the tip-to-surface distance. The vertical distribution of the monotonically decaying force was a reflection of the thickness of the modifier layer deposited on the surface. The dynamic friction coefficient at the real sliding interfaces having macroscopic dimensions responded to the nanometer-scale distribution of the modifier layer when mechanically probed by the AFM tip.

One potential advantage of the AFM-based method for modifier characterization is the nanometer-scale resolution of the lateral coordinates over the solid surface. The other operando methods mentioned in Section 1.1 Back ground provide the mass, chemical structure, or layer thickness of the deposited modifier averaged over a millimeter-sized lubricant–solid interface. Real modifier layers can be heterogeneous, particularly in the presence of two or more modifiers. Rubbing the layers may induce further heterogeneity to produce tribolayers. AFM-based force mapping is a standalone technique for *locally* characterizing the lubricant modifiers in the buried interfaces.

2.4 Young's modulus calculated from the force curve

In this subsection, the Young's modulus of the C18AP adsorption layer was evaluated from the measured force curve. Attempts to calculate Young's modulus by applying a theoretical contact model to force-sample deformation curves obtained from force curves have been made in previous studies[23-25], and Young's modulus was calculated from the force curve measured in Contact Mode. The force curve in the contact mode is effective for a sample with a Young's modulus of several MPa to several hundred MPa, because it can detect the force in the order of μN. On the other hand, the Young's modulus of the precursors C18AP layer formed by physical or chemical adsorption on the iron oxide film as a preliminary step to form the reaction coating was predicted to be smaller. Therefore, this method was applied to the force curve measured by frequency modulation in order to evaluate the Young's modulus of the precursors C18AP layer. Because the force curve measured by the frequency modulation is superior in the force sensitivity compared with the force curve in Contact Mode, it was expected that a smaller Young's modulus could be evaluated.

In order to calculate Young's modulus, a theoretical contact model is applied to a force curve measured with AFM. An appropriate theoretical model must be chosen from the shape of the indenter and the shape of the measured force curve. Typical theoretical contact models used in this method are Hertz, DMT[26], Sneddon[27], and JKR[28-30] model. The shape of indenter is assumed as sphere in Hertz and JKR model, and cone in Sneddon model, respectively. The Hertz and Sneddon models do not consider the effect of the adsorption force between the probe and the sample. In JKR model, Young's modulus is calculated from the adsorption force between the probe and the sample.

In this experiment, in order to evaluate the interface between the PAO containing C18AP and the iron film, the force curve was measured in the lubricating oil. Therefore, the adsorption force between the probe and the sample was not shown in the force curve. And the probe shape was a cone. Therefore, Sneddon model was applied to the force curve. Figure 2.4.1 shows a schematic diagram of a conical indenter in contact with a plane assumed in Sneddon model.

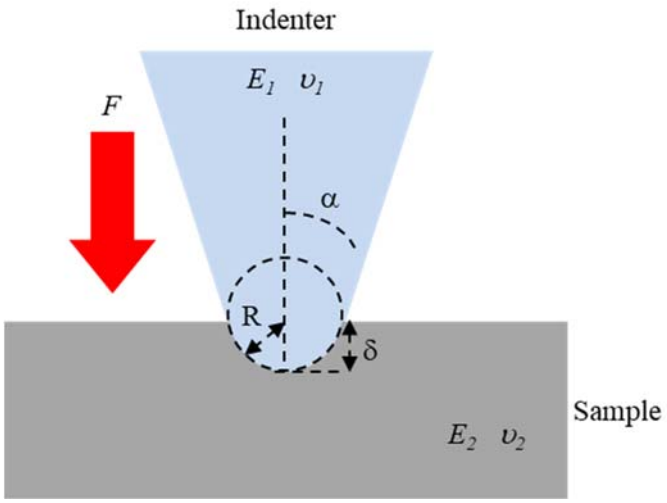

Figure 2.4.1 Schematic diagram of a conical indenter in contact with a plane assumed in Sneddon model.

As shown in Figure 2.4.1, when the conical indenter comes into contact with the surface of the plane sample under the force F, the sample deformation δ is given by Equation 2.4.1:

$$\boldsymbol{F = \frac{2}{\pi} E^{*}(\tan\alpha)\delta^{2}} \qquad 2.4.1$$

where E^* is the composite Young's modulus and α is the half-vertex angle of the conical indenter. The composite Young's modulus E^* is calculated by Equation 2.4.2 using the Young's modulus E_1 of the indenter, the Young's modulus E_2 of the sample, Poisson's ratio v_1 of the indenter, and the Poisson's ratio v_2 of the sample.

$$\frac{\mathbf{1}}{\boldsymbol{E^*}} = \frac{\mathbf{1} - \boldsymbol{v_1^2}}{\boldsymbol{E_1}} + \frac{\mathbf{1} - \boldsymbol{v_2^2}}{\boldsymbol{E_2}} \qquad 2.4.2$$

Assuming that the Young's modulus of the cantilever is much larger than that of the sample, Equation 2.4.2 is approximated as Equation 2.4.3:

$$\boldsymbol{E^*} = \frac{\boldsymbol{E_2}}{\mathbf{1} - \boldsymbol{v_2^2}} \qquad 2.4.3$$

Putting Equation 2.4.3 into Equation 2.4.1 yields:

$$\boldsymbol{F} = \frac{\mathbf{2}}{\boldsymbol{\pi}} \frac{\boldsymbol{E_2}\mathbf{tan}\boldsymbol{\alpha}}{\mathbf{1} - \boldsymbol{v_2^2}} \boldsymbol{\delta^2} \qquad 2.4.4$$

In order to calculate the Young's modulus from the measured force curve, the force curve was converted into a load-deformation curve (F-δ curve), and the F-δ curve of the Sneddon theoretical model was fitted to the F-δ curve obtained from the force curve. In this case, we assumed that C18AP layers adsorbed on the iron film is sufficiently soft and the Z displacement was equal to the sample deformation. The force curve measured at the interface between PAO containing 200 ppm C18AP and the iron film was used for this analysis. Since the material of the cantilever used is Si with Young's modulus of about 185 GPa, and the adsorption film of C18AP is expected to be sufficiently soft, it is reasonable to apply Equation 2.4.4. First, the logarithm of both sides of Equation 2.4.4 is:

$$\mathbf{log_{10}}\,\boldsymbol{F} = \mathbf{2}\,\mathbf{log_{10}}\,\boldsymbol{\delta} + \mathbf{log_{10}}\frac{\mathbf{2}\boldsymbol{E_2}\mathbf{tan}\boldsymbol{\alpha}}{\boldsymbol{\pi}\left(\mathbf{1} - \boldsymbol{v_2^2}\right)} \qquad 2.4.5$$

In Equation 2.4.5, F and δ have a linear relationship, and the regression line can be calculated by applying the least squares method to the experimental results. Figure 2.4.2 shows $\log_{10}$(Force)-$\log_{10}$(Deformation) graph calculated from the experimental

results, and its regression line. The theoretical slope of the regression line is 2, and If the intercept of the regression line is b, E_2 can be calculated as follows:

$$E_2 = \frac{\pi(1-\upsilon_{2)}^2}{2\tan\alpha}10^b \qquad 2.4.6$$

Here, the force curve measured in PAO containing 200ppm C18AP shown in Figure2.3.3(e) was used for this analysis. As the results, b was 8.1769 and E_2 was 545 MPa in this analysis.

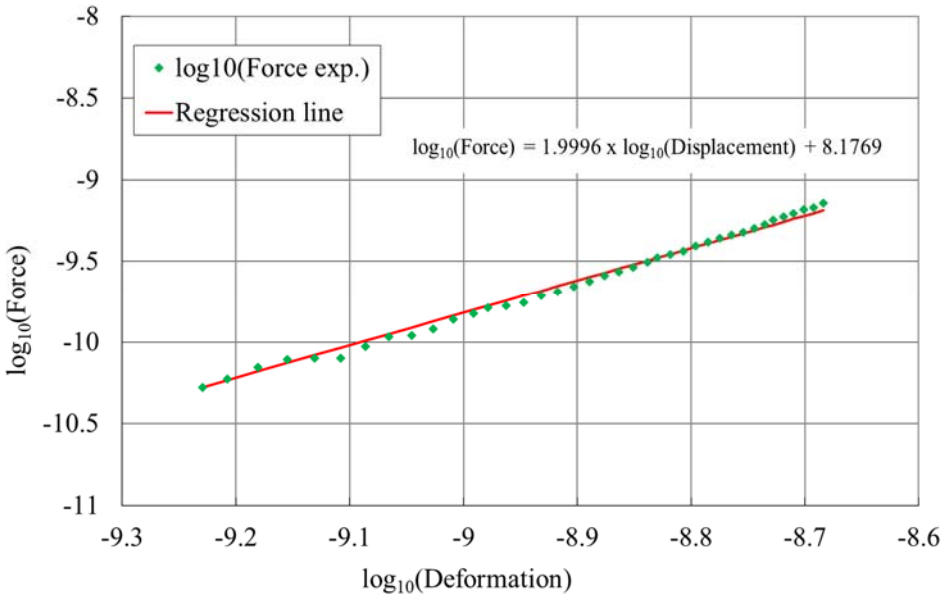

Figure 2.4.2 $\log_{10}$(Force)-$\log_{10}$(Deformation) graph calculated from the experimental results, and its regression line.

Figure 2.4.3 shows the *F*-δ curve obtained from the force curve and the theoretical curve obtained by putting intercept b calculated from the regression line in Figure 2.4.2 into Equation 2.4.6. The experimental values are in good agreement with the theoretical curves, so it can be concluded that the Sneddon model was applied appropriately in order to evaluate Young's modulus. On the other hand, Young's modulus of about 500 MPa is equivalent to that of high density polyethylene and

polytetrafluoroethylene. Considering that the oscillating cantilever can move into the C18AP adsorption layer while oscillating, the Young's modulus calculated from the force curve is expected to be higher than the actual value. This is thought to be due to the influence of the iron film. In the end, the actual Young's modulus was not confirmed in this study. However, from the experiments up to the previous subsection, it was found that there was a liquid adsorption layer composed of C18AP. The Young's modulus of this layer was determined, even though it was recognized that there was a defect in the evaluation method. Considering the effect of the iron film below C18AP adsorption layer on this result, the Young's modulus of C18AP adsorption layer may be able to be evaluated.

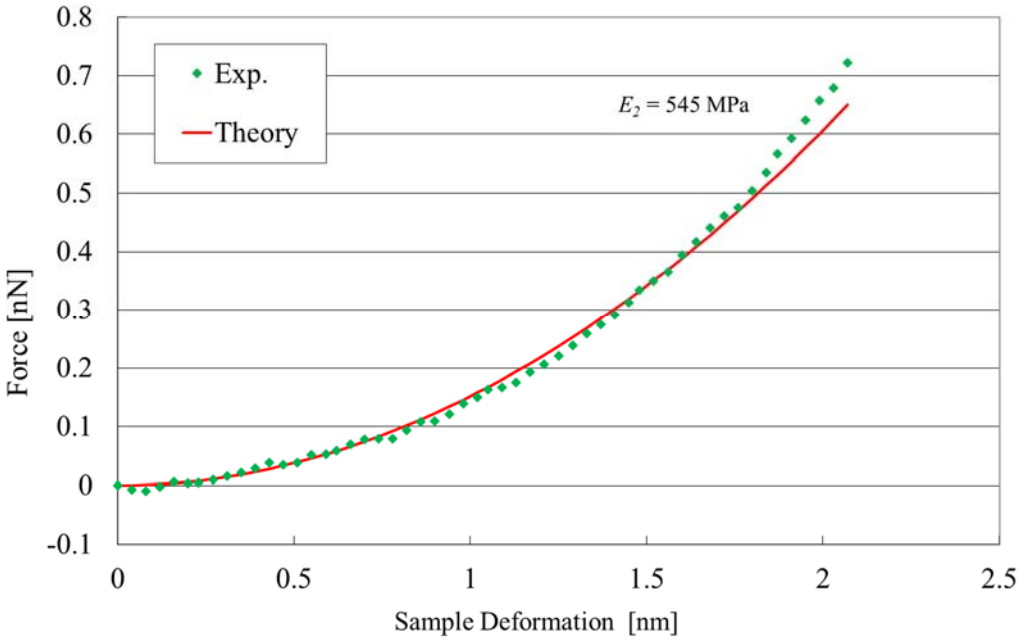

Figure 2.4.3 *F*-δ curve obtained from the force curve and the theoretical curve obtained by putting intercept b calculated from the regression line in Figure 2.4.2 into Equation 2.4.6.

Núria Gavara et al. reported on the correction of the influence from the hard substrate in estimating the Young's modulus of the thin sample using atomic force

microscopy tips.[31] The influence from the hard substrate can be corrected by the following equation.

$$F = \frac{2}{\pi}\frac{E_2 \tan\alpha}{1-0.5^2}\delta^2 \times \left\{1 + 1.7795\frac{2\tan\alpha}{\pi^2}\frac{\delta}{h} + 16(1.7795)^2(\tan\alpha)^2\frac{\delta^2}{h^2} + O\left(\frac{\delta^3}{h^3}\right)\right\} \quad 2.4.7$$

where F is the applied force, δ is sample deformation, α is the half-vertex angle of the conical indenter, h is the thickness of the sample, and Poisson's ratio υ was assumed to be 0.5.

The F and δ data sets in the F-δ curve shown in Figure 2.4.3, transformed from the force curve measured in PAO containing 200 ppm of C18AP, were substituted into Equation 2.4.7 to calculate Young's modulus E_2. The film thickness was assumed to be 2 nm. The relationship between the sample deformation and Young's modulus is shown in Figure 2.4.4. When the sample deformation is small, the Young's modulus is close to that calculated by the Sneddon model. As the sample deformation approached the film thickness of 2nm, the Young's modulus decreased to about 100 MPa, the same as the rubber.

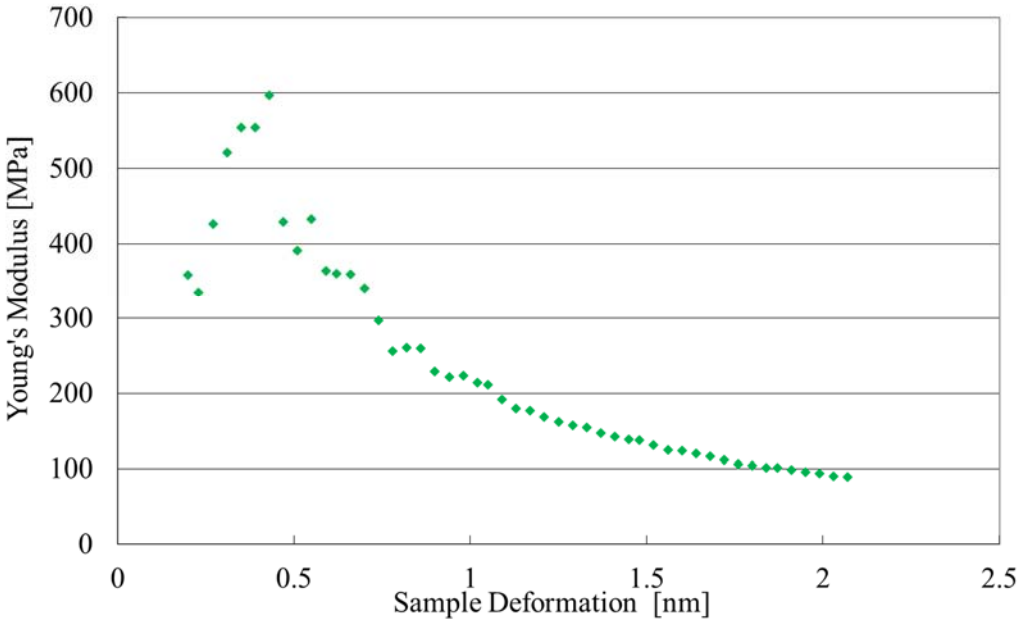

Figure 2.4.4 Relationship between the sample deformation and Young's modulus

2.5 Conclution

We demonstrated the feasibility of using FM-AFM for mechanically probing a lubricant–solid interface, C18AP-containing PAO covering the iron films. We mapped the lubricant-induced force on the probing tip two-dimensionally on a plane that was perpendicular to the lubricant–iron interface and thus achieved a force sensitivity and spatial resolution on the order of 10 pN and 10 pm, respectively. We propose the following conclusions after interpretation of the observed force maps. The PAO was directly exposed to the naturally oxidized iron film in the absence of the C18AP modifier, and it exhibited a few liquid layer parallel to the film surface with a layer-to-layer distance of 0.6–0.7 nm. C18AP, if any in the lubricant, was adsorbed with its phosphoric acid end anchored to the films. There was fluctuation of the $C_{18}H_{35}$ chains of C18AP in the lubricant. The force maps reflected the time-averaged density distribution of the fluctuating chains and monotonically decayed to zero force at a tip-to-surface distance of 2 nm when a monomolecular layer of C18AP was completed. The PAO liquid layers were intermittently removed in the lubricants containing C18AP concentrations of 0.2 and 2 ppm; they completely disappeared at 20 and 200 ppm. The iron film that was completely covered with the C18AP layer produced topographic images with reduced sharpness according to its fluctuating, dynamic boundary with the lubricant. The dynamic friction coefficient of the sliding steel–lubricant–steel interfaces, which was separately determined using the friction tester, decreased with increasing the coverage of the monomolecular C18AP on the iron film.

The mechanical probing with FM-AFM combined with friction test offers a promising technique for bridging nanometer-scale lubricant distribution and sliding friction in the macroscopic dimensions.

2.6 Reference

(1) Lubricant Modifiers, Chemistry and Applications. Second edition. Ed. Rudnick, L. R., 2009, Culinary and Hospitality Industry Publications Services.

(2) Sader, J. E.; Jarvis, S. P. Accurate formulas for interaction force and energy in frequency modulation force spectroscopy. *Appl. Phys. Lett.,* 2004, *84*, 1801−1803.

(3) Reischl, B.; Watkins, M.; Foster, A. Free Energy Approaches for Modeling Atomic Force Microscopy in Liquids. *J. Chem. Theory Comput.,* 2013, *9*, 600–608.

(4) Amano, K.; Suzuki, K.; Fukuma, T.; Takahashi, O.; Onishi, H., The Relationship between Local Liquid Density and Force Applied on A Tip of Atomic Force Microscope: A Theoretical Analysis for Simple Liquids. *J. Chem. Phys.,* 2013, *139*, 224710.

(5) Hiasa, T.; Kimura, K.; Onishi, H., Two-Dimensional Distribution of Liquid Hydrocarbons Facing Alkanethiol Monolayers Visualized by Frequency Modulation Atomic Force Microscopy. *Coll. Surf. A,* 2012, *396*, 203-207.

(6) Hirayama, T.; Kawamura, R.; Fujino, K.; Matsuoka, T.; Komiya, H.; Onishi, H., Cross-Sectional Imaging of Boundary Lubrication Layer Formed by Fatty Acid by Means of Frequency-Modulation Atomic Force Microscopy. *Langmuir,* 2017, *33*, 10492–10500.

(7) Gosvami, N. N.; Sinha, S. K.; Hofbauer, W. O'Shea, S. J. Solvation and squeeze out of hexadecane on graphite. *J. Chem. Phys*., 2007, *126*, 214708.

(8) Pham Van L.; Kyrylyuk, V.; Polesel-Maris, J.; Thoyer, F.; Lubin, C.; Cousty, J. Experimental three-dimensional description of the liquid hexadecane/graphite interface. *Langmuir,* 2009, *25*, 639–642.

(9) Hiasa, T.; Kimura, K.; Onishi, H., Cross-Sectional Structure of Liquid 1-Decanol over Graphite. *J. Phys. Chem. C,* 2012, *116*, 26475–26479.

(10) de Beer, S.; Wennink, P.; van der Weide-Grevelink, M.; Mugele, F. Do epitaxy and temperature affect oscillatory solvation forces? *Langmuir,* 2010, *26*, 13245–13250.

(11) Hofbauer, W.; Ho, R. J.; Hairulnizam, R.; Gosvami, N. N.; O'Shea, S. J., Crystalline structure and squeeze-out dissipation of liquid solvation layers observed by small-amplitude dynamic AFM. *Phys. Rev. B,* 2009, *80*, 134104.

(12) Minato, T.; Araki, Y.; Umeda, K.; Yamanaka, T.; Okazaki, K.; Onishi, H.; Abe, T.; Ogumi, Z., Interface Structure between Tetraglyme and Graphite, *J. Chem. Phys.,* 2017, *147*, 124701.

(13) Gosvami, N. N.; Sinha, S. K.; O'Shea, S. J. Squeeze-out of branched alkanes on graphite. *Phys. Rev. Lett.,* 2008, *100*, 076101.

(14) Krass, M.-D.; Krämer, G.; Dellwo, U.; Bennewitz, R. Molecular Layering in Nanometer-Confined Lubricants. *Tribo. Lett.,* 2018, *66*, 87.

(15) Allinger, N. L.; Gava, M. P.; Jongh, D. C.; Johnson, C. .R.; Lebel, N. A.; Stevens, C. L. ORGANIC CHEMISTRY. *Worth Publishers, Inc*., 1971.

(16) Hiasa, T.; Kimura, K.; Onishi, H. Polesel-Maris, J.; Thoyer, F.; Lubin, C.; Cousty, J. Cross-Sectional Structure of Liquid 1-Decanol over Graphite. J. Phys. Chem., C, 2012, 116, 26475–26479.

(17) Asakawa, H.; Yoshioka, S.; Nishimura, K.; Fukuma, T. Spatial Distribution of Lipid Headgroups and Water Molecules at Membrane/Water Interfaces Visualized by Three-Dimensional Scanning Force Microscopy. *ACS Nano,* 2012, *6*, 9013–9020.

(18) Molino, P. J.; Yang, D.; Penna, M.; Miyazawa, K.; Knowles, B. R.; MacLaughlin, S. ; Fukuma, T.; Yarovsky, I.; Higgins, M. J. Hydration Layer Structure of Biofpuling-Resistant Nanoparticles. *ACS Nano,* 2018, *12*, 11610–11624.

(19) Moustafa, A. M. A.; Huang, J.; McPhedran, K. N.; Zeng, H.; El-Din, M. G. Probing the Adsorption of Weak Acids on Graphite Using Amplitude Modulation−Frequency Modulation Atomic Force Microscopy. *Langmuir,* 2015, *31*, 3069–3075.

(20) Okubo, H.; Sasaki, S., Frequency-Modulation Atomic Force Microscopic Observation for Ultralow Frictional Solid–Liquid Interface of Diamond–Like Carbon in an Environmentally Friendly *Oil. Tribo. Lett.,* 2019, *67*, 3.

(21) Norimune Soda (1911-1995), a mechanical engineer in Japan, originally designed the tester that the authors used in this study.

(22) Atkins, T.; Paula, J de. Atkins' PHYSICAL CHEMISTRY Tenth Edition. *Oxford University Press*, 2014.

(23) Wang, D.; Fujinami, S.; Nakajima, K.; Niihara, K.; Inukai, S.; Ueki, H.; Magario, A.; Noguchi, T.; Endo, M.; Nishi, T. Production of a cellular structure in carbon nanotube/natural rubber composites revealed by nanomechanical mapping. *Carbon*, 2010, *48*, 3708.

(24) Wang, D.; Fujinami, S.; Nakajima, K.; Nishi, T. True Surface Topography and Nanomechanical Mapping Measurements on Block Copolymers with Atomic Force Microscopy. *Macromolecules*, 2010, *43*, 5521.

(25) Wang, D.; Nakajima, K.; Fujinami, S.; Shibasaki, Y.; Wang, J. -Q.; Nishi, T. Characterization of morphology and mechanical properties of block copolymers using atomic force microscopy: Effects of processing conditions. *Polymer*, 2012, *53*, 1960.

(26) Derjaguin, B. V.; Muller, V. M.; Toporov, Y.P. Effect of contact deformations on the adhesion of particles. *Colloid. Interf. Sci.*, 1975, *53*, 314.

(27) Sneddon, I. N. The relation between load and penetration in the axisymmetric boussinesq problem for a punch of arbitrary profile. *Int. J. Eng. Sci.*, 1965, *3*, 47.

(28) Johnson, K. L.; Kendall, K.; Roberts, A. D. Surface Energy and Contact of Elastic Solids. *Proc. Roy. Soc. Lond.*, 1971, *A*, 324301.

(29) Maugis, D.; Barquins, M. Adhesive contact of a conical punch on an elastic half-space. *J. Phys. Lett.*, 1981, *42*, L95.

(30) Sun, Y.; Akhremitchev, B.; Walker, G. C. Using the adhesive interaction between atomic force microscopy tips and polymer surfaces to measure the elastic modulus of compliant samples. *Langmuir*, 2004, *20*, 5837-5845

(31) Gavara, N.; Chadwick, R. S. Determination of the elastic moduli of thin samples and adherent cells using conical atomic force microscope tips. *Nature Nanotech.*, 2012, *7*, 733-736

2.7 Supporting Information

2.7.1 The application of the Lorentz function to the observed spectral density

By fitting the Lorentz function to the power spectrum of the cantilever acquired by the spectrum analyzer, the oscillation amplitude of the cantilever under measurement with FM-AFM and the noise level of the system can be obtained.

Assuming that the thermal oscillation of the cantilever is a harmonic oscillation, the motion equation is as follows.

$$\boldsymbol{m\ddot{z} + \frac{m\omega_0}{Q}\dot{z} + m\omega_0^2 z = f(t)} \qquad 2.7.1$$

where $f(t)$ is the force that causes thermal oscillation, m is the mass of the cantilever, k is the spring constant, ω_0 is the resonance angular frequency of the cantilever, and Q is the Q value of the cantilever. Fourier transform of both sides of Equation 2.7.1 gives the following equation.

$$\boldsymbol{\frac{Z(\omega)}{F(\omega)} = \frac{1}{m(\omega_0^2 - \omega^2) + {im\omega_0\omega}/{Q}} = H(\omega)} \qquad 2.7.2$$

Further, the spectrum density of the displacement $|Z(\omega)|^2$ and the transfer function $H(\omega)$ satisfy the following relation according to the first fluctuation-dissipation theorem:

$$\boldsymbol{|Z(\omega)|^2 = -\frac{4k_BT}{\omega}\mathrm{Im}[H(\omega)]} \qquad 2.7.3$$

where k_B is the Boltzmann constant, T is the temperature, and Im[$H(\omega)$] is the imaginary component of $H(\omega)$. Putting Equation 2.7.2 into Equation 2.7.3 yields:

$$Z(\omega) = \sqrt{\frac{4k_BT}{Qk\omega_0}\frac{1}{\left(1-\left({}^{\omega}/_{\omega_0}\right)^2\right)^2+\left({}^{\omega}/_{\omega_0 Q}\right)^2}} \qquad 2.7.4$$

Putting $\omega=2\pi f$ into Equation 2.7.4 yields:

$$Z(f) = \sqrt{\frac{2k_BT}{\pi Qkf_0}\frac{1}{\left(1-\left({}^{f}/_{f_0}\right)^2\right)^2+\left({}^{f}/_{f_0 Q}\right)^2}} \qquad 2.7.5$$

The spectrum density of the displacement δ_z in the displacement detection system of the AFM is the sum of the sensor noise density n_{sensor} and the thermal noise density $Z(f)$:

$$\delta_z = \sqrt{n_{sensor}^2+\frac{2k_BT}{\pi Qkf_0}\frac{1}{\left(1-\left({}^{f}/_{f_0}\right)^2\right)^2+\left({}^{f}/_{f_0 Q}\right)^2}} \qquad 2.7.6$$

In addition, the voltage noise density δV, the displacement detection sensitivity S_{sensor}, and the displacement noise density δ_z have the following relationships.

$$\delta V = S_{sensor}\delta_z \qquad 2.7.7$$

Assuming that the sensor noise density n_{sensor} in the measured frequency range is white noise with a uniform intensity in all frequency bands, δV is calculated from Euation 2.7.6 and Equation 2.7.7 as follows:

$$\begin{aligned}\delta V &= \sqrt{S_{sensor}^2 n_{sensor}^2 + S_{sensor}^2 Z(f)^2} \\ &= \sqrt{\delta V_{sensor}^2 + \delta V_{peak}^2 \frac{1}{Q^2\left(1-\left({}^{f}/_{f_0}\right)^2\right)^2+\left({}^{f}/_{f_0}\right)^2}}\end{aligned} \qquad 2.7.8$$

where

$$\boldsymbol{\delta V_{peak} = S_{sensor}\sqrt{\frac{2k_B TQ}{\pi k f_0}}} \qquad 2.7.9$$

$$\boldsymbol{S_{sensor} = \delta V_{peak}\sqrt{\frac{\pi k f_0}{2k_B TQ}}} \qquad 2.7.10$$

δV_{peak} and Q can be obtained by fitting Equation 2.7.8 to the measured thermal oscillation spectrum using the Levenberg-Marquardt method. So S_{sensor} can be calculated from Equation 2.7.10.

2.7.2 Iron film topography in lubricants

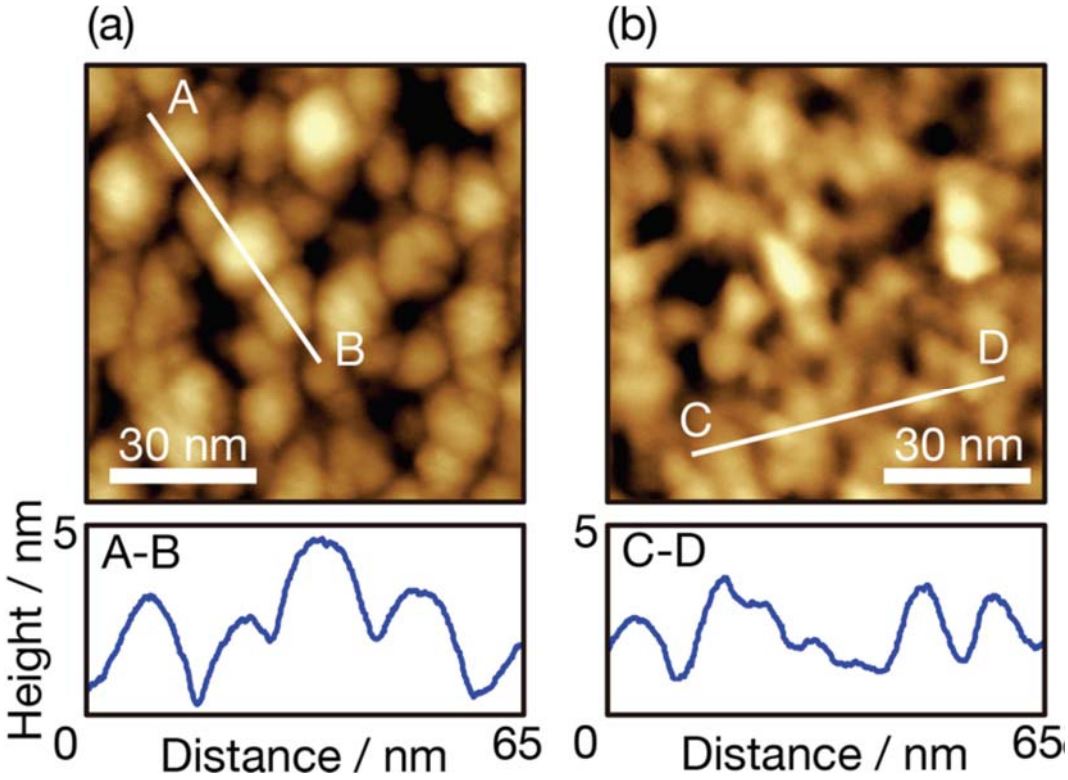

Figure 2.7.1 The topography of iron films observed in lubricants. The concentration of C18AP was (a) 0 and (b) 200 ppm. Image size: 90 nm square. Peak-to-peak amplitude of cantilever oscillation (A): 2.0 nm. Frequency-shift (Δf) setpoint: +83 Hz. Cross sections determined along the A-B and C-D lines are shown in the corresponding lower panels. Image (a) was observed with the cantilever that was used for determining the topographic image shown in Figure 2.3.2(a) of the main text. Image (b) was determined with another cantilever.

2.7.3 Force Mapping

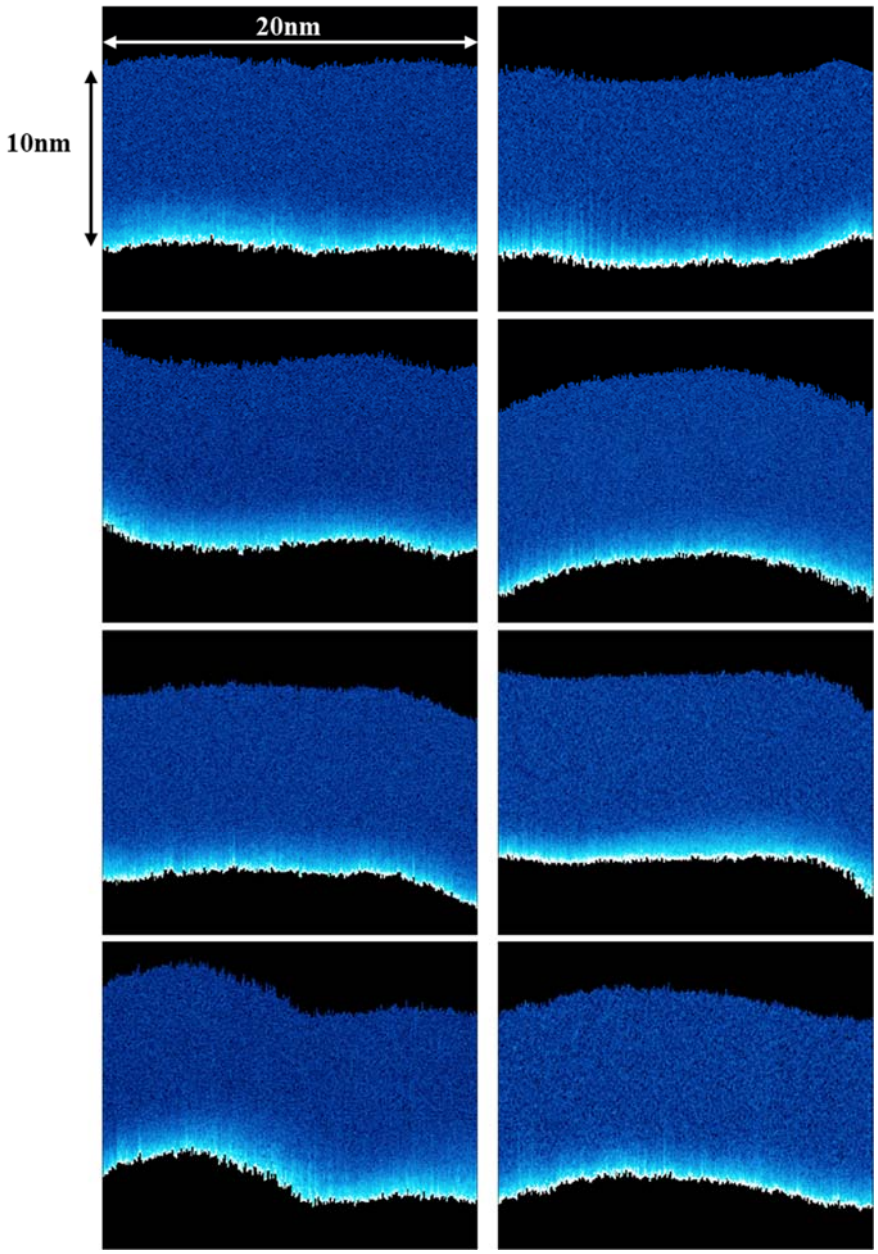

Figure 2.7.2 Lubricants over the iron films. The cross-sectional frequency shift distribution was mapped on a plane that was perpendicular to the film surface in the lubricants containing C18AP at 20 ppm. The amplitude of the cantilever oscillation was 0.4 nm. The aspect ratio of the lateral and vertical scales has been tuned unity in the maps. A large (or small) positive frequency shift is depicted using a bright (or dark) blue color.

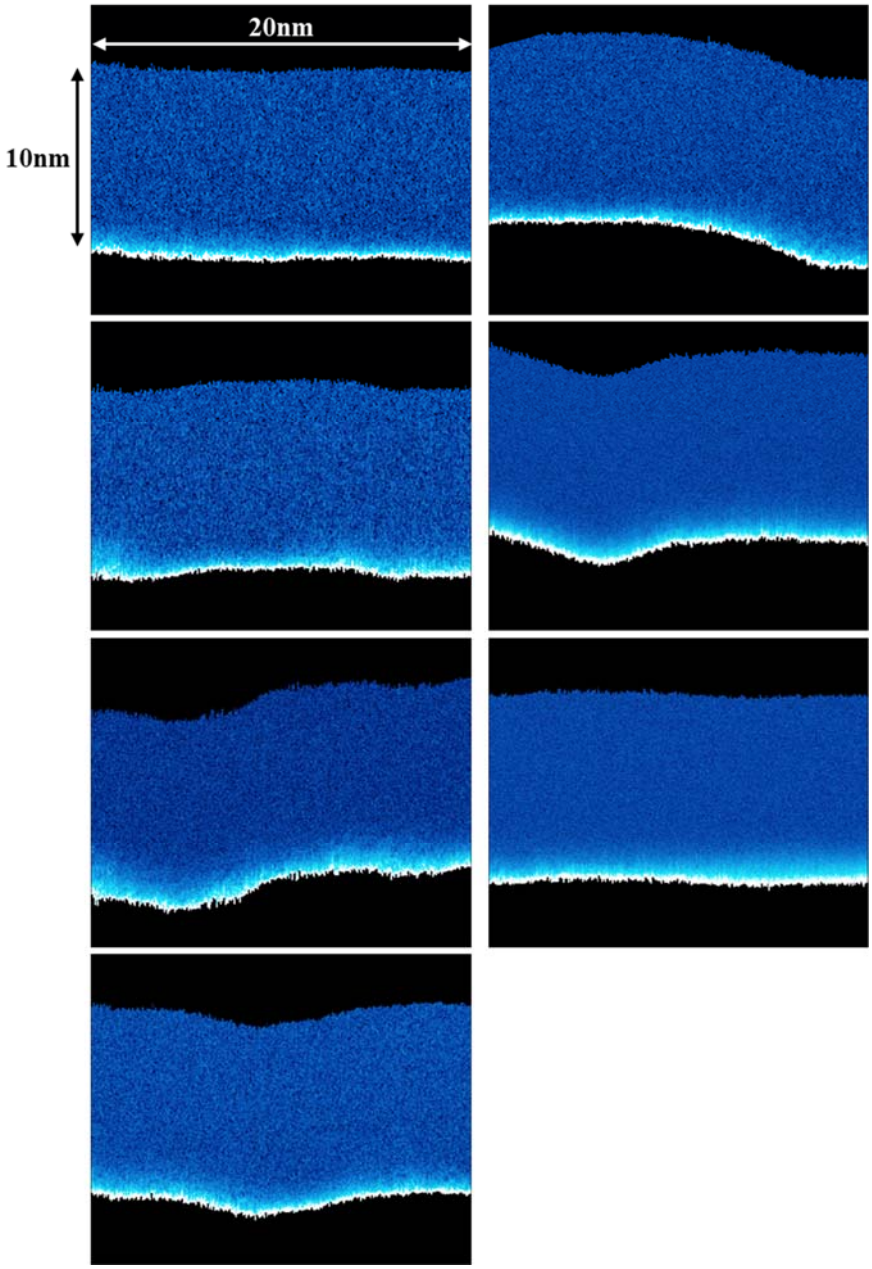

Figure 2.7.3 Lubricants over the iron films. The cross-sectional frequency shift distribution was mapped on a plane that was perpendicular to the film surface in the lubricants containing C18AP at 200 ppm. The amplitude of the cantilever oscillation was 0.4 nm. The aspect ratio of the lateral and vertical scales has been tuned unity in the maps. A large (or small) positive frequency shift is depicted using a bright (or dark) blue color.

2.7.4 Friction test results

Table 2.7.1 Pendulum amplitudes in pure PAO.

	A0	A1	A2	A3	A4	A5	A6	A7	A8	A9	A10	A11	n
run1	0.500	0.460	0.425	0.390	0.355	0.320	0.285	0.250	0.220	0.185	0.150	0.115	11
run2	0.500	0.465	0.425	0.390	0.355	0.315	0.280	0.240	0.205	0.170	0.130		10
run3	0.500	0.465	0.430	0.390	0.350	0.310	0.270	0.225	0.180	0.135			9
run4	0.500	0/460	0.420	0.380	0.340	0.300	0.255	0.205	0.155				8
run5	0.500	0.455	0.415	0.370	0.325	0.270	0.215	0.150					7
run6	0.500	0.450	0.400	0.340	0.280	0.210	0.130						6
run7	0.500	0.440	0.380	0.310	0.230	0.140							5
run8	0.500	0.430	0.360	0.280	0.190								4
un9	0.500	0.425	0.345	0.255	0.160								4
run10	0.500	0.415	0.330	0.235	0.130								4
run11	0.500	0.410	0.315	0.215	0.105								4
run12	0.500	0.405	0.305	0.195									3
run13	0.500	0.395	0.290	0.180									3
run14	0.500	0.395	0.285	0.165									3
run15	0.500	0.390	0.275	0.155									3
run16	0.500	0.385	0.270	0.150									3
run17	0.500	0.385	0.265	0.140									3
run18	0.500	0.380	0.260	0.135									3
run19	0.500	0.380	0.255	0.130									3
run20	0.500	0.375	0.250	0.120									3

Table 2.7.2 Pendulum amplitudes in PAO containing C18AP of 2 ppm.

	A0	A1	A2	A3	A4	A5	A6	A7	A8	A9	A10	n
run1	0.500	0.455	0.415	0.380	0.340	0.300	0.265	0.225	0.190	0.150	0.115	10
run2	0.500	0.465	0.420	0.380	0.340	0.305	0.265	0.225	0.185	0.145	0.110	10
run3	0.500	0.465	0.420	0.385	0.345	0.305	0.265	0.225	0.180	0.140		9
run4	0.500	0.460	0.420	0.380	0.335	0.290	0.240	0.190	0.135			8
run5	0.500	0.455	0.410	0.255	0.300	0.235	0.170	0.100				7
run6	0.500	0.450	0.390	0.330	0.260	0.185	0.170					6
run7	0.500	0.440	0.375	0.305	0.225	0.145						5
run8	0.500	0.435	0.365	0.285	0.205	0.120						5
un9	0.500	0.430	0.350	0.265	0.180							4
run10	0.500	0.420	0.335	0.245	0.145							4
run11	0.500	0.415	0.320	0.225	0.125							4
run12	0.500	0.410	0.310	0.205	0.100							4
run13	0.500	0.405	0.295	0.185								3
run14	0.500	0.400	0.290	0.185								3
run15	0.500	0.400	0.290	0.185								3
run16	0.500	0.395	0.290	0/180								3
run17	0.500	0.395	0.290	0.180								3
run18	0.500	0.395	0.285	0.180								3

Table 2.7.3 Pendulum amplitudes in PAO containing C18AP of 20 ppm.

	A0	A1	A2	A3	A4	A5	A6	A7	A8	A9	A10	n
run1	0.500	0.465	0.425	0.390	0.355	0.320	0.280	0.245	0.210	0.170	0.135	10
run2	0.500	0.465	0.425	0.390	0.355	0.320	0.280	0.245	0.210	0.170	0.135	10
run3	0.500	0.465	0.430	0.390	0.355	0.320	0.285	0.245	0.210	0.170	0.125	10
run4	0.500	0.465	0.430	0.390	0.355	0.315	0.280	0.240	0.195	0.150	0.105	10
run5	0.500	0.470	0.430	0.390	0.350	0.310	0.270	0.230	0.180	0.135		9
run6	0.500	0.465	0.425	0.385	0.345	0.305	0.260	0.215	0.170	0.120		9
run7	0.500	0.465	0.425	0.385	0.340	0.300	0.250	0.205	0.155	0.110		9
run8	0.500	0.465	0.420	0.380	0.335	0.290	0.240	0.190	0.140			8
un9	0.500	0.465	0.420	0.375	0.330	0.280	0.235	0.175	0.120			8
run10	0.500	0.465	0.415	0.370	0.320	0.270	0.215	0.155				7
run11	0.500	0.455	0.410	0.360	0.305	0.250	0.190	0.125				7
run12	0.500	0.455	0.405	0.350	0.290	0.225	0.160					6
run13	0.500	0.450	0.395	0.330	0.265	0.185	0.110					6
run14	0.500	0.440	0.375	0.305	0.225	0.145						5
run15	0.500	0.440	0.365	0.285	0.200	0.115						5
run16	0.500	0.435	0.355	0.265	0.175							4
run17	0.500	0.430	0.345	0.255	0.155							4
run18	0.500	0.430	0.345	0.250	0.155							4
run19	0.500	0.430	0.340	0.245	0.150							4
run20	0.500	0.425	0.335	0.240	0.140							4

Table 2.7.4 Pendulum amplitudes in PAO containing C18AP of 200 ppm.

	A0	A1	A2	A3	A4	A5	A6	A7	A8	A9	A10	A11
run1	0.500	0.470	0.435	0.405	0.370	0.335	0.300	0.270	0.235	0.200	0.165	0.135
run2	0.500	0.465	0.435	0.400	0.370	0.340	0.310	0.275	0.245	0.215	0.180	0.150
run3	0.500	0.465	0.430	0.400	0.370	0.340	0.310	0.280	0.250	0.220	0.190	0.160
run4	0.500	0.465	0.430	0.400	0.370	0.340	0.310	0.280	0.250	0.225	0.195	0.165
run5	0.500	0.470	0.440	0.405	0.375	0.345	0.315	0.285	0.255	0.225	0.195	0.170
run6	0.500	0.465	0.430	0.400	0.370	0.340	0.310	0.280	0.250	0.225	0.195	0.165
run7	0.500	0.465	0.435	0.405	0.375	0.345	0.315	0.285	0.255	0.225	0.195	0.165
run8	0.500	0.460	0.430	0.400	0.370	0.340	0.310	0.280	0.250	0.225	0.195	0.165
un9	0.500	0.465	0.435	0.405	0.375	0.345	0.315	0.285	0.255	0.225	0.195	0.170
run10	0.500	0.564	0.435	0.405	0.375	0.345	0.315	0.285	0.255	0.225	0.195	0.170

	A12	A13	n
run1	0.100		12
run2	0.115		12
run3	0.130		12
run4	0.135	0.105	13
run5	0.140	0.110	13
run6	0.140	0.110	13
run7	0.140	0.110	13
run8	0.135	0.110	13
un9	0.140	0.110	13
run10	0.140	0.110	13

Chapter 3 Poly-α-olefins containing carboxylic acids over crystalline iron oxide

3.1 Introduction

The usefulness of imaging the adsorption layers of modifier molecules to solid surfaces was demonstrated in Chapter 2. The phosphoric acid alkyl ester is a modifier classified as an abrasion preventing agent, and forms a protective film comprising a secondary compound by sliding to prevent wear. In Chapter 2, the precursor adsorption films formed by the physical or chemical adsorption of modifier molecules on the solid surface as a preliminary step in the formation of secondary compounds were observed.

In this chapter, the adsorption film of oiliness agents, which are typical modifiers as well as antifriction agents, were evaluated. Oiliness agents are effective at relatively low temperatures (Around room temperature) and under low loads. Therefore, the adsorption state of the modifier molecules can be captured in a more realistic environment as compared with the case of the antifriction agent. The oiliness agent is generally widely used modifiers and have been extensively studied to improve their performance. Whether the modifier adsorption layer is monolayer or multi-layers has also been discussed for a long time.[1, 2, 3] And Hardy et al. have shown that the friction reduction effect depends on the molecular weight of modifier molecules.[4] The results of friction tests using an LB film substrate reported by F. P. Bowden et al. in 1950 show that the initial friction coefficient is the same regardless of whether the film is a monolayer or a multi-layer film, and that the multi-layer film has higher wear resistance[5]. In addition to the studies mentioned here, there have been many other studies on the adsorption film of the oiliness agent and its friction-reducing effect.[7-8], and several studies were introduced here. However, there is few analyses to visualize it, although the adsorption layers of modifier molecules are an important point for improving performance. In this chapter, a representative hydrocarbon lubricant in

commerce, poly-α-olefin, is modified with different quantities of carboxylic acids, some of frequently used modifiers as the oiliness agent in real lubricants. The presence or absence of modifier layers are probed on iron oxide single-crystalline wafers using FM-AFM. The vertical as well as lateral distribution of the layers is visualized by mapping layer-induced force on the probing tip. Furthermore, the temperature dependence of the modifier adsorption layers on the iron oxide single-crystalline wafer is verified by probing under heating. Then the dynamic friction coefficient of steel–lubricant–iron oxide single-crystalline wafer interfaces is separately determined with a ball on disk friction tester. The macroscopic friction property as a function of temperature is compared with the nanometer-scale distribution of the modifier layers.

3.2 Materials

3.2.1 Lubricants

Six kinds of model lubricants were prepared. Non-polar PAO was used as the base oil. Five kinds of carboxylic acids (oleic acid, stearic acid, caprylic acid, 2-Ethylhexanoic acid, elaidic acid) with different molecular structures were used as modifiers. The chemical structure of the lubricants component is illustrated in Figure 3.2.1. PAO (Ineos, Durasyn164) containing decene trimers ($C_{30}H_{62}$) as the major component was purified with activated clay. The purified liquid possessed a dynamic viscosity of 4 mm^2 s^{-1} at 100 C^o. Oleic acid, stearic acid and elaidic acid contain eighteen carbon atoms. Stearic acid is a saturated fatty acid with a linear single chain hydrocarbon. Oleic acid and elaidic acid has a double bond between carbon atoms with cis and trans conformation, respectively. Caprylic acid is a linear fatty acid with eight carbon atoms. 2-Ethylhexanoic acid has eight carbon atoms as same as caprylic acid, but the structure is more complex.

One of the five carboxylic acids was added to the base oil with a fixed concentration of 1 mmol/kg. In addition to these five lubricants containing an modifier, pure PAO was also used as a lubricant in this study.

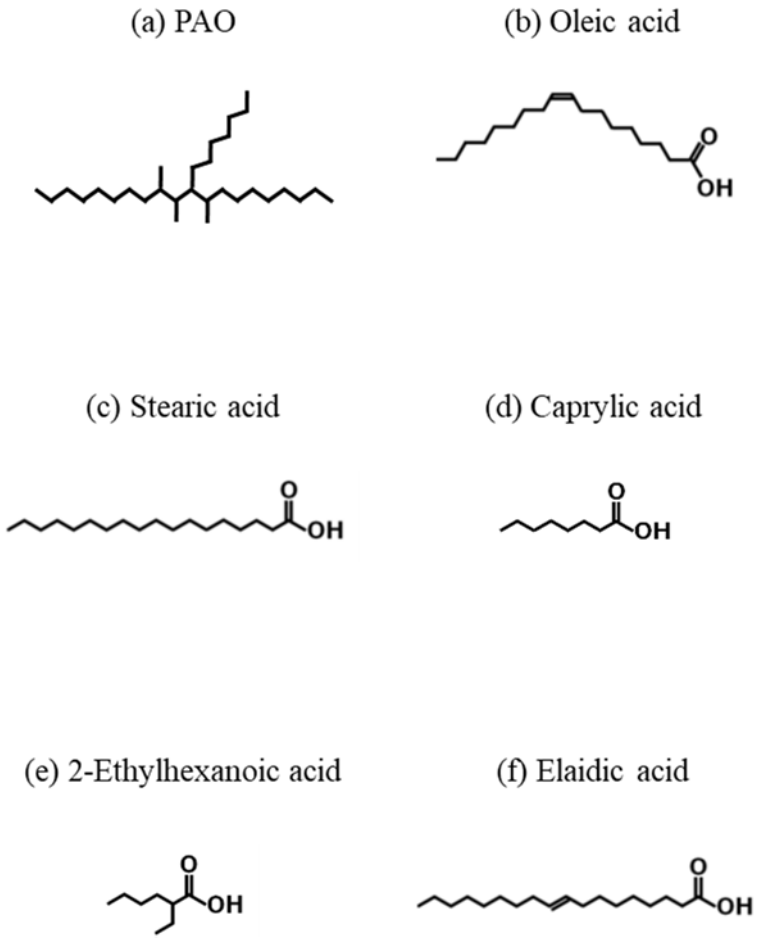

Figure 3.2.1 Lubricant. (a) decene trimer as the major component in the poly-α-olefin (PAO) used in this study. The longest (C_{20}) alkyl chain is depicted in the all-*trans* conformation. (b) oleic acid, (c) stearic acid, (d) caprylic acid, (e) 2-Ethylhexanoic acid, (f) Elaidic acid

3.2.2 Iron oxide single-crystalline wafers

Fe_2O_3 (0001) single-crystalline wafers were used as a model of oxidized steal. The iron oxide single-crystalline wafer has the crystal structure shown in Figure.3.2.2. A topographic image of the crystalline wafer is shown in Figure.3.2.3. The crystalline wafers provided atomically more flat topography than the iron film used for the experiments discussed in Chapter 2, which was convenient for highly precise measurements around the lubricant-metal interfaces. The crystalline wafers were annealed in air at 1073 K for 1 hour to smooth the surface. The surface treatment of the single-crystalline wafers was carried out by Akira SASAHARA of Kobe University.

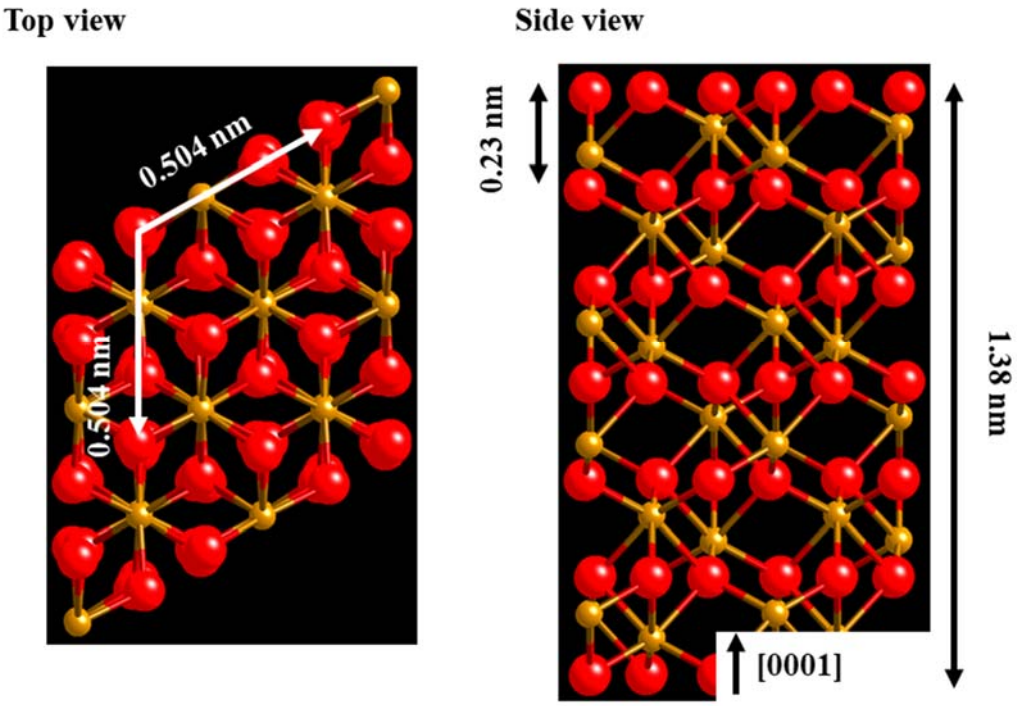

Figure 3.2.2 The crystal structure of the iron oxide single-crystalline wafer

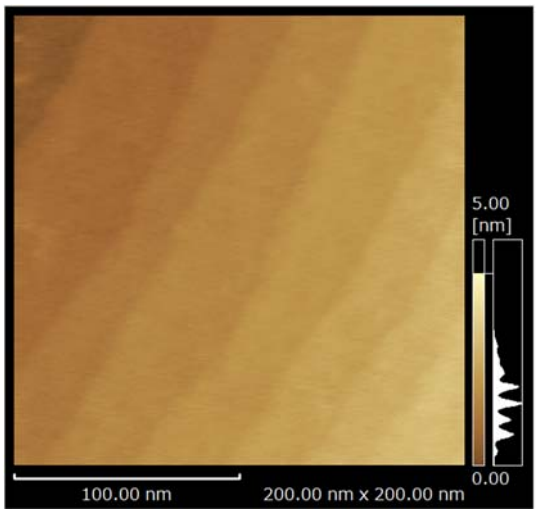

Figure 3.2.3 Topographic image of the iron oxide single-crystalline wafer. The crystalline wafers provided atomically flat topography

3.3 Results and discussion

3.3.1 Analysis by FM-AFM in room temperature

3.3.1.1 Methods

Frequency-modulation detection of force on the probing tip was enabled with an SPM-8100FM microscope (Shimadzu). In topographic imaging of iron oxide single-crystalline wafers, the resonance oscillation of a silicon cantilever (Nanoworld, PPP-NCHAuD) was mechanically excited with a piezo-actuator. The nominal spring constant of the cantilevers was 42 N m^{-1}. The oscillation amplitude was regulated at a preset amplitude (A). When a lubricant-induced conservative force was loaded on the tip, the resonance frequency of cantilever oscillation (f) shifted accordingly. The topography of the scanned wafers was traced with regulation of the tip–surface distance by keeping the frequency shift (Δf) at a prefixed setpoint. The resonant frequency of the cantilevers was 100–140 kHz, and the quality factor of oscillation resonance was 2–3 in the lubricants. A typical spectrum of thermally induced cantilever oscillation is shown in Figure 2.3.1. An iron oxide single-crystalline wafer was fixed in a quartz petri dish placed on the microscope stage driven by a piezoelectric scanner. The dish was filled with the lubricant of 500 μl and then the cantilever assembly was put on top. Imaging scans were conducted at RT.

3.3.1.2 Iron oxide single-crystalline wafer topography

Figure 3.3.1 represents topographic images of the iron oxide single-crystalline wafers observed in (a) pure PAO, (b) PAO containing oleic acid, (c) PAO containing stearic acid and (d) PAO containing caprylic acid. The topographic images are consisted of 512 × 512 pixels, and bright colors represent higher parts and dark colors show lower parts. First, scanning was performed in a narrow area from 200 nm × 200 nm to 500 nm × 500 nm, and then scanning was performed again at the same position by expanding the scanning area to 500 nm × 500 nm to 1800 nm × 1800 nm. In (a) pure PAO, there was no deposition on the scanned area. On the other hand, in (b) PAO containing oleic acid and (c) PAO containing stearic acid, something having a height of 0.61 nm and 1.82nm was deposited on the scanned area.

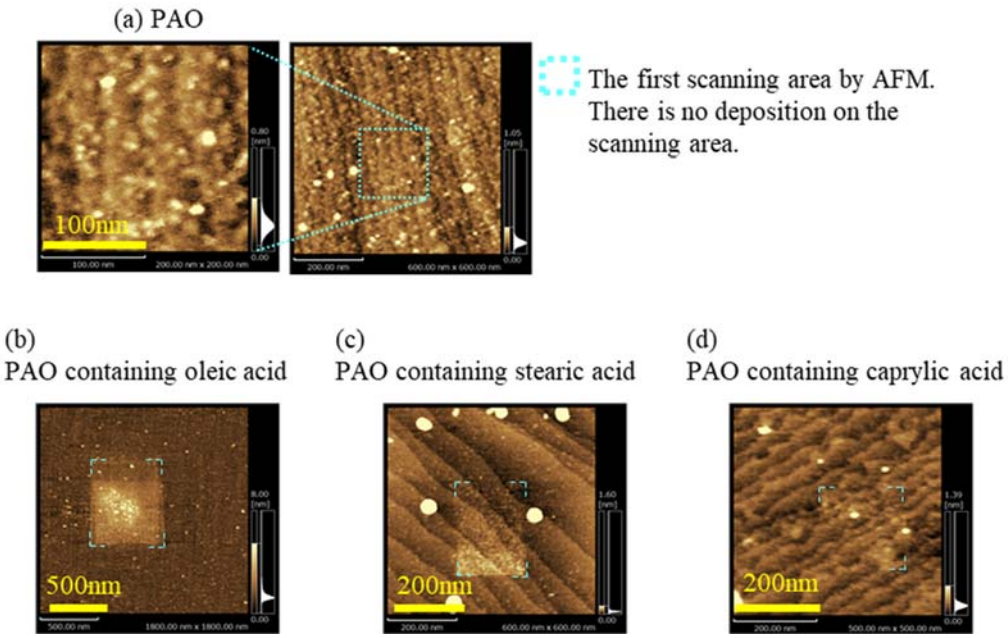

Figure 3.3.1 The topographic images of the iron oxide single-crystalline wafers observed in lubricants. Lubricants were (a) PAO, (b) PAO containing oleic acid, (c) PAO containing stearic acid, (d) PAO containing caprylic acid, peak-to-peak amplitude of cantilever oscillation: 4.0 nm, and frequency-shift set point: +33 Hz.

The cross sections determined along the A-B, C-D and E-F lines are shown below the corresponding images in Figure3.3.2. The cross sections represent the average on the white line including ten lines. In (d) PAO containing caprylic acid, thinner deposits were observed compared to (b) and (c). These results suggest that the deposition was derived from modifiers and a pseudo-sliding of AFM scanning promoted adsorption of modifiers to the iron oxide single-crystalline wafers.

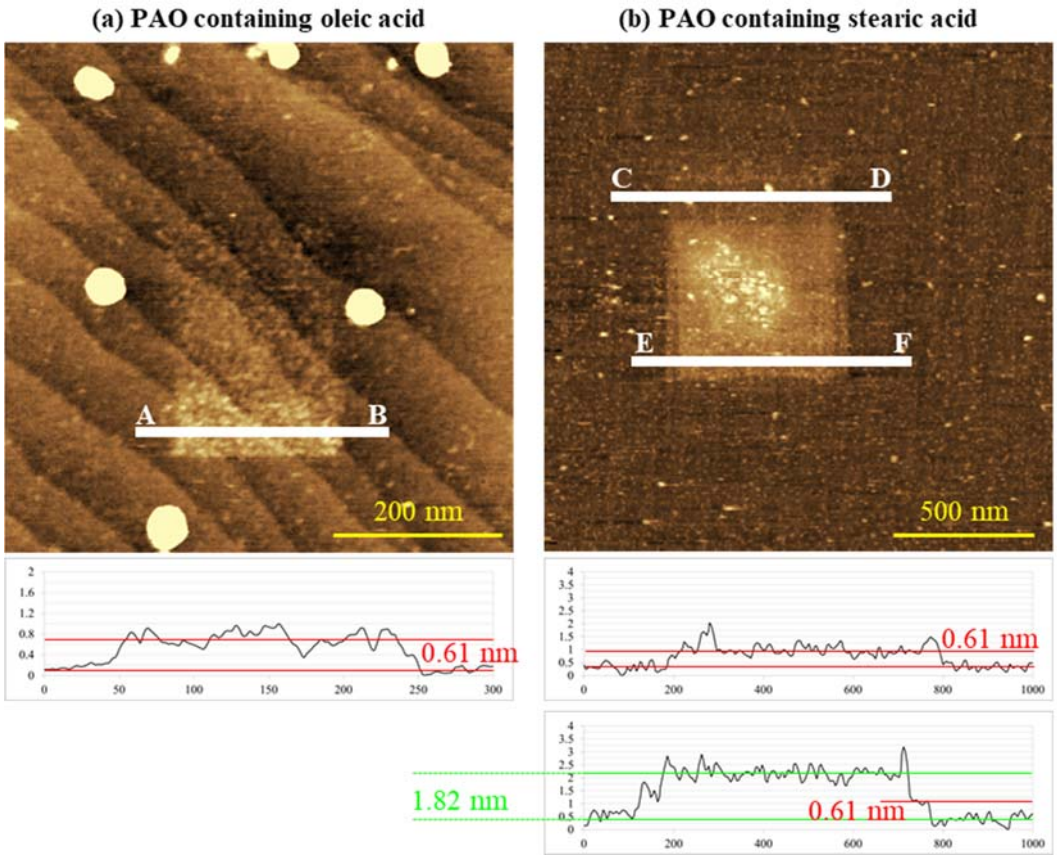

Figure 3.3.2 The topographic images of the iron oxide single-crystalline wafers observed in (a) PAO containing oleic acid, (b) PAO containing stearic acid, and the cross sections determined along the A-B, C-D and E-F lines are shown below the corresponding images. The height of deposition is 0.61 nm and 1.82nm in (a) PAO containing oleic acid, and 0.61 nm in (b) PAO containing stearic acid.

Next, it was confirmed how much this adsorption was promoted by the AFM scanning. Figure. 3.3.3 shows the topographic images of the same position on the iron oxide single-crystalline wafer measured in PAO containing stearic acid 10 times continuously. The first image is at the upper left, the next image is below it, and the column changes from the fifth image. The 3rd column includes the 9th and 10th images. The topographic images are consisted of 512 × 512 pixels, and bright colors represent higher parts and dark colors show lower parts. The scanning was performed in 200 nm × 200 nm. The adsorption gradually increased from the first image to 10th image.

After 10 scans, another 10 scans were performed. The result is shown in Figure 3.3.4. Comparing these images, it can be seen that the deposition greatly increased from the first to the t10th image, but hardly increased from the 10th to the 20th image.

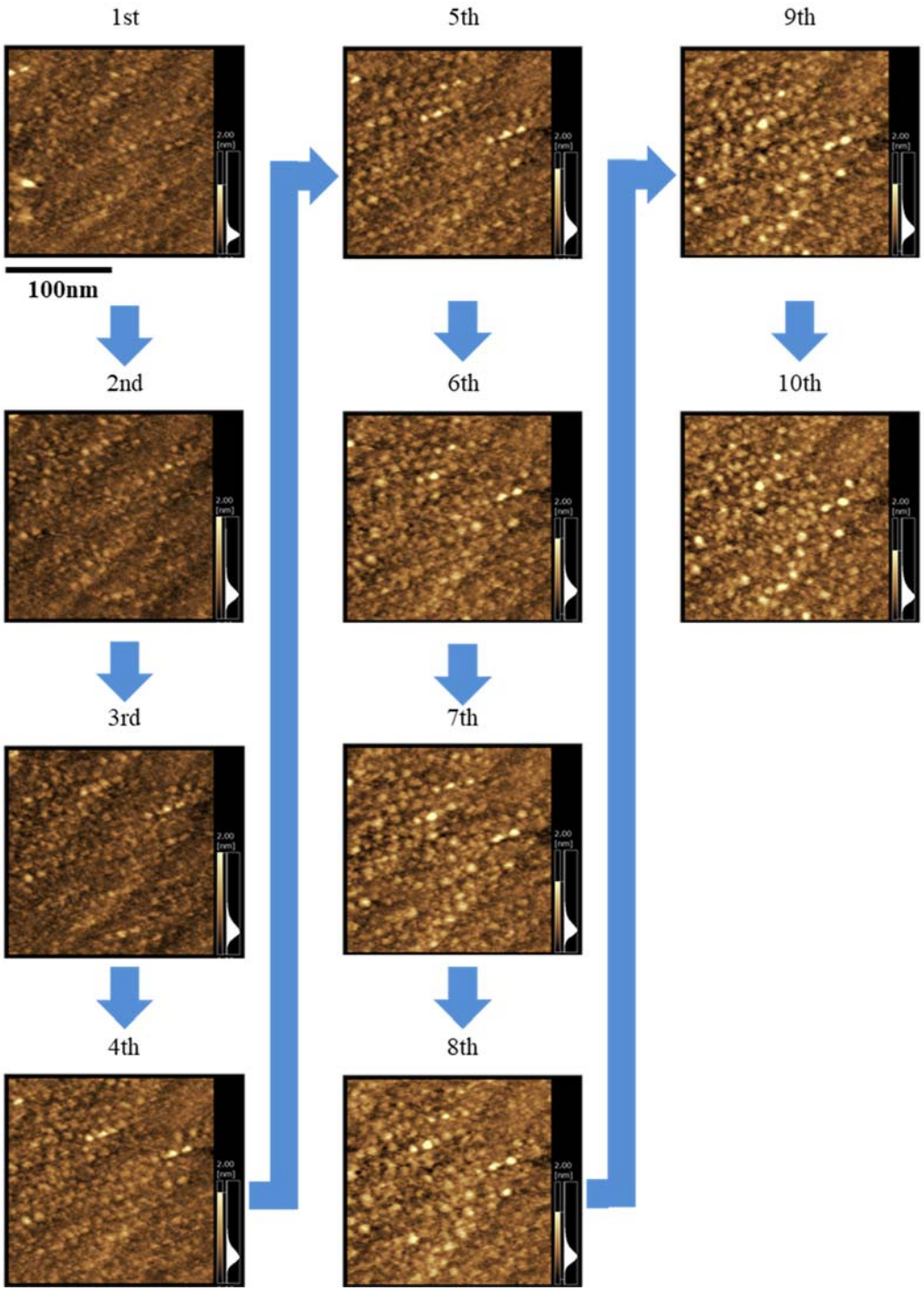

Figure 3.3.3 The topographic images of the iron oxide single-crystalline wafer measured 10 consecutive times at the same position. Peak-to-peak amplitude of cantilever oscillation: 4.0 nm, and frequency-shift set point: +33 Hz.

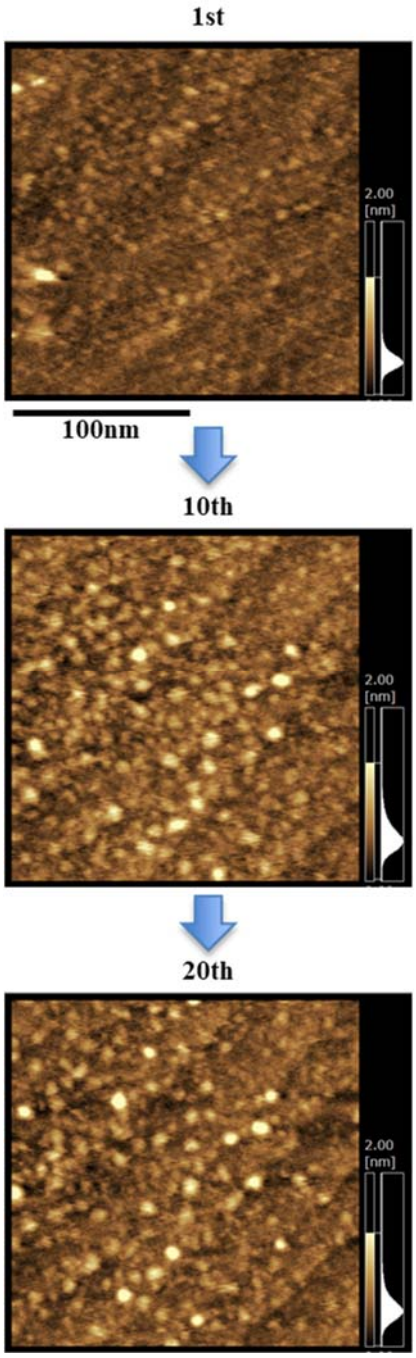

Figure 3.3.4 The topographic images of the same position on the iron oxide single-crystalline wafer measured in PAO containing stearic acid 20 times continuously. The first image is shown above, the 10th image is shown in the center, and the 20th image is shown below. Peak-to-peak amplitude of cantilever oscillation: 4.0 nm, and frequency-shift set point: +33 Hz.

Figure 3.3.5 shows a topographic image measured in the same position as previous scans in a larger scan area 600 nm × 600 nm after 20 times scans. There is more deposition only in the scanned area than the other areas. The height of the depositions ranged from 0.58 nm to 1.96 nm shown in Figure 3.3.6. These results indicate that AFM scanning promotes the adsorption of the modifier to the iron oxide wafer, and the adsorption has an upper limit.

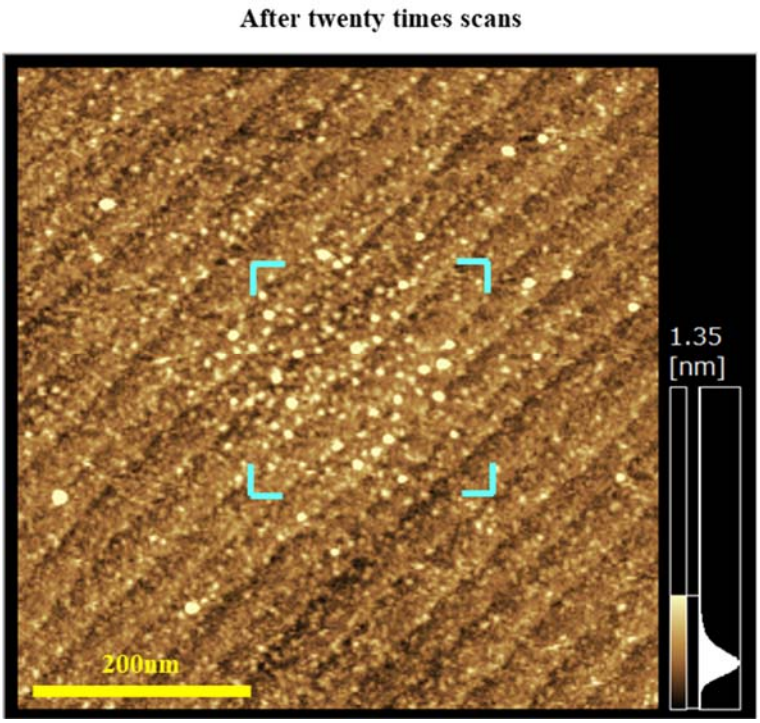

Figure 3.3.5 A topographic image measured in the same position as previous scans in a larger scan area after 20 times scans. There is more deposition only in the scanned area than the other areas. Peak-to-peak amplitude of cantilever oscillation: 4.0 nm, and frequency-shift set point: +33 Hz.

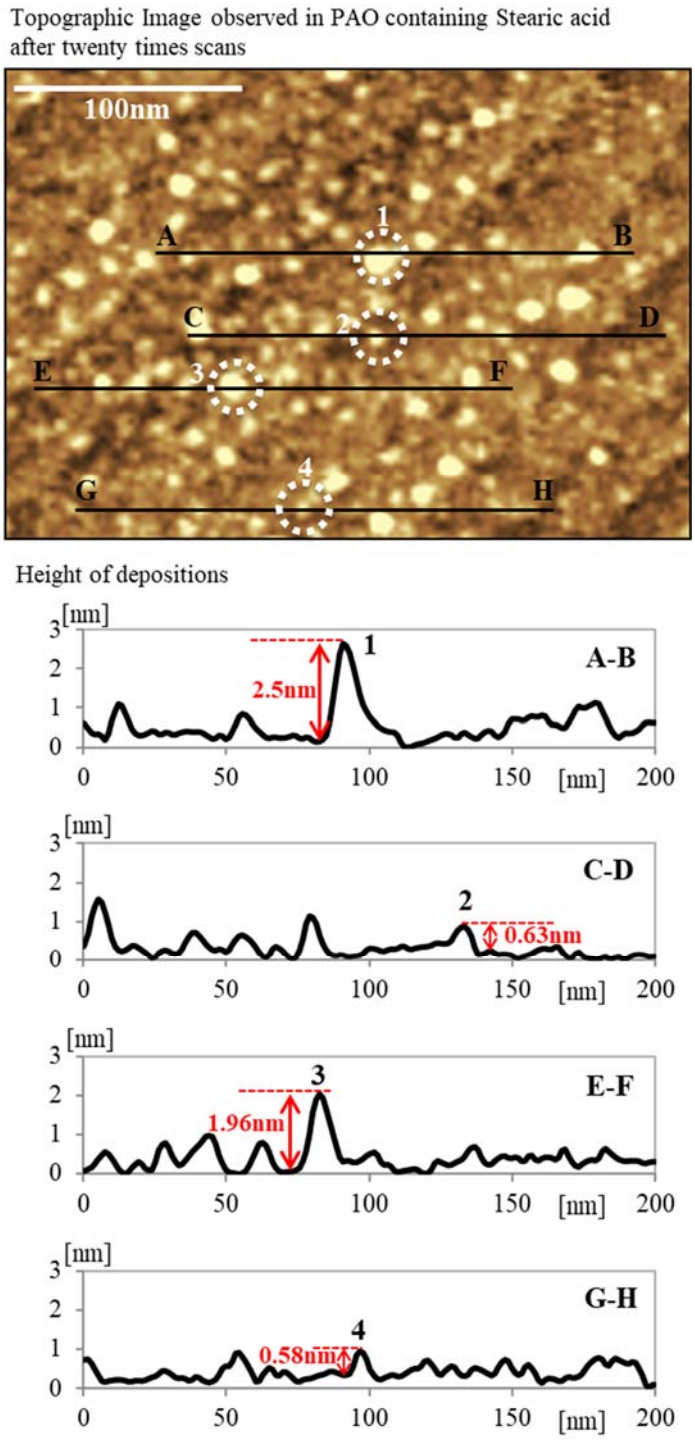

Figure 3.3.6 A topographic image observed in PAO containing Stearic acid after twenty times scans, and cross section profiles determined along the A-B, C-D, F-F and G-H lines are shown below the image. There were some depositions having a height of 0.58 nm to 1.96 nm.

The molecular behavior inferred from these topographic images is shown in Figure 3.3.7. The polar groups of the modifier molecules were chemically adsorbed on the iron atoms of the iron oxide wafer. The parts where the modifier molecules were densely adsorbed were observed as protrusions with the same height as the length of the modifier molecules. In the areas where the modifier molecules were sparsely adsorbed were observed as low protrusions. In addition, the adsorption of modifier molecules is not uniform due to the effect of the atomic state of the wafer surface.

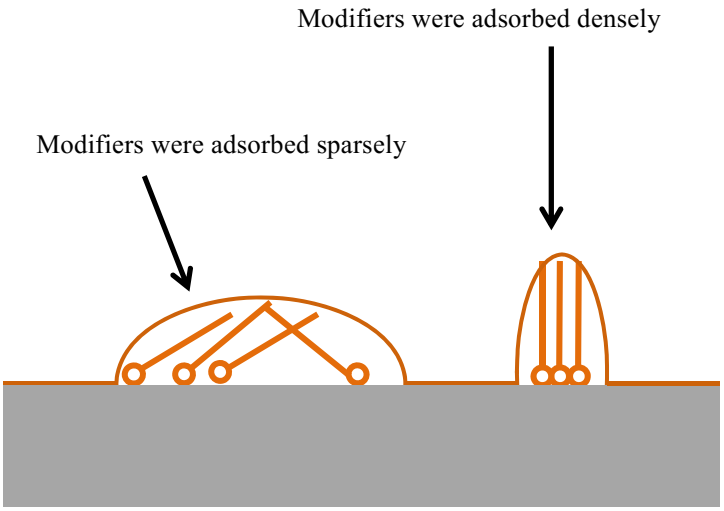

Figure 3.3.7 The molecular behavior inferred from these topographic images

3.3.1.3 Force mapping

In previous subsection, the modifier molecules strongly adsorbed on the iron oxide single-crystalline wafer were observed, and it was confirmed that the modifier molecules adsorption to the iron oxide single-crystalline wafers was promoted by a pseudo-sliding of AFM scanning. In this subsection, the mechanical response of the expanding chains is probed and mapped on the planes that are perpendicular to the iron oxide single-crystalline wafers to verify the modifier molecules flexibly adsorbed on the iron oxide single-crystalline wafers.

Figure 3.3.8 shows the frequency-shift maps observed on the iron oxide single-crystalline wafer immersed in (a) pure PAO, (b) PAO containing oleic acid, (c) PAO containing stearic acid and (d) PAO containing caprylic acid. The oscillating cantilever was scanned vertically from the bulk lubricant to the iron oxide single-crystalline wafers. The frequency shift as a function of the vertical coordinate was simultaneously recorded to obtain one Δf-distance curve composed of 256 pixels at one lateral position. The vertical scan was aborted when Δf reached a predetermined threshold (+600 Hz for the acquired maps (a), (b), +700 Hz for the acquired maps (c), +300 Hz for the acquired maps (d) in Figure 3.3.8); the cantilever was retracted into the lubricant by 5 nm to prevent extensive tip-to-surface contact. 256 vertical scans along a 10 nm long lateral coordinate were acquired repeatedly. One Δf map was subsequently constructed on a plane perpendicular to the iron oxide single-crystalline wafer with an acquisition time of 26 seconds for 256 scans per frame. Bright color represents large positive frequency shift. Dark blue color shows small positive or even negative frequency shifts, while areas outside the scanned range are shown in black.

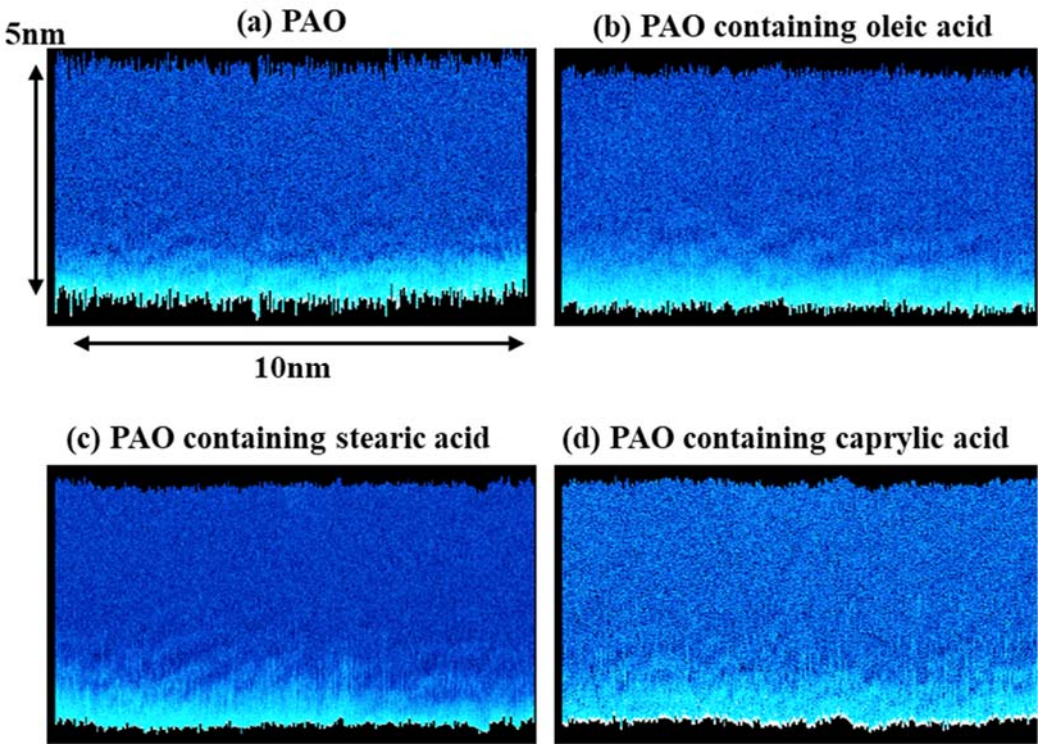

Figure 3.3.8 Lubricants over the iron oxide single-crystalline wafer. The cross-sectional frequency shift distribution was mapped on a plane that was perpendicular to the wafer surface in PAO containing (a) no modifier, (b) oleic acid, (c) stearic acid, (d) caprylic acid. The amplitude of the cantilever oscillation was 0.4 nm. The aspect ratio of the lateral and vertical scales has been tuned unity in the maps. A large (or small) positive frequency shift is depicted using a bright (or dark) blue color.

The layer structure was observed in all cases. In each case, the layer-to-layer distances were measured at four different positions, as shown in Figure 3.3.9. Four frequency shift-distance curves shown in the panel below each image are the average profile curve on the white lines containing 10 lines. Two layers were clearly confirmed in each frequency shift-distance curve. The layer-to-layer distance on each curve was measured, and the average of these four values is shown in table 3.3.1.

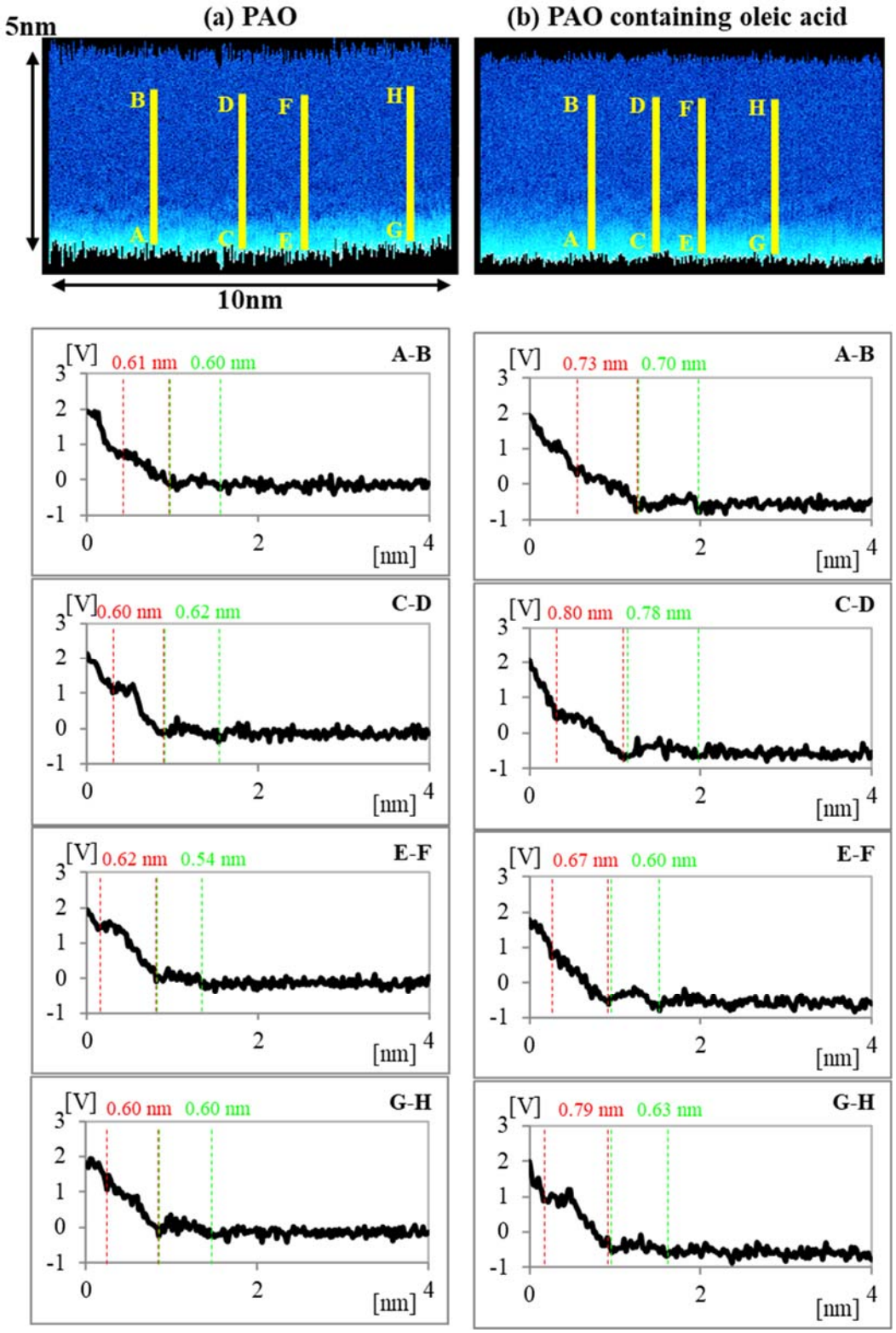
(a) PAO
(b) PAO containing oleic acid
5nm
10nm
A
B
C
D
E
F
G
H
A-B
C-D
E-F
G-H
[V]
[nm]
0.61 nm
0.60 nm
0.73 nm
0.70 nm
0.60 nm
0.62 nm
0.80 nm
0.78 nm
0.62 nm
0.54 nm
0.67 nm
0.60 nm
0.60 nm
0.60 nm
0.79 nm
0.63 nm

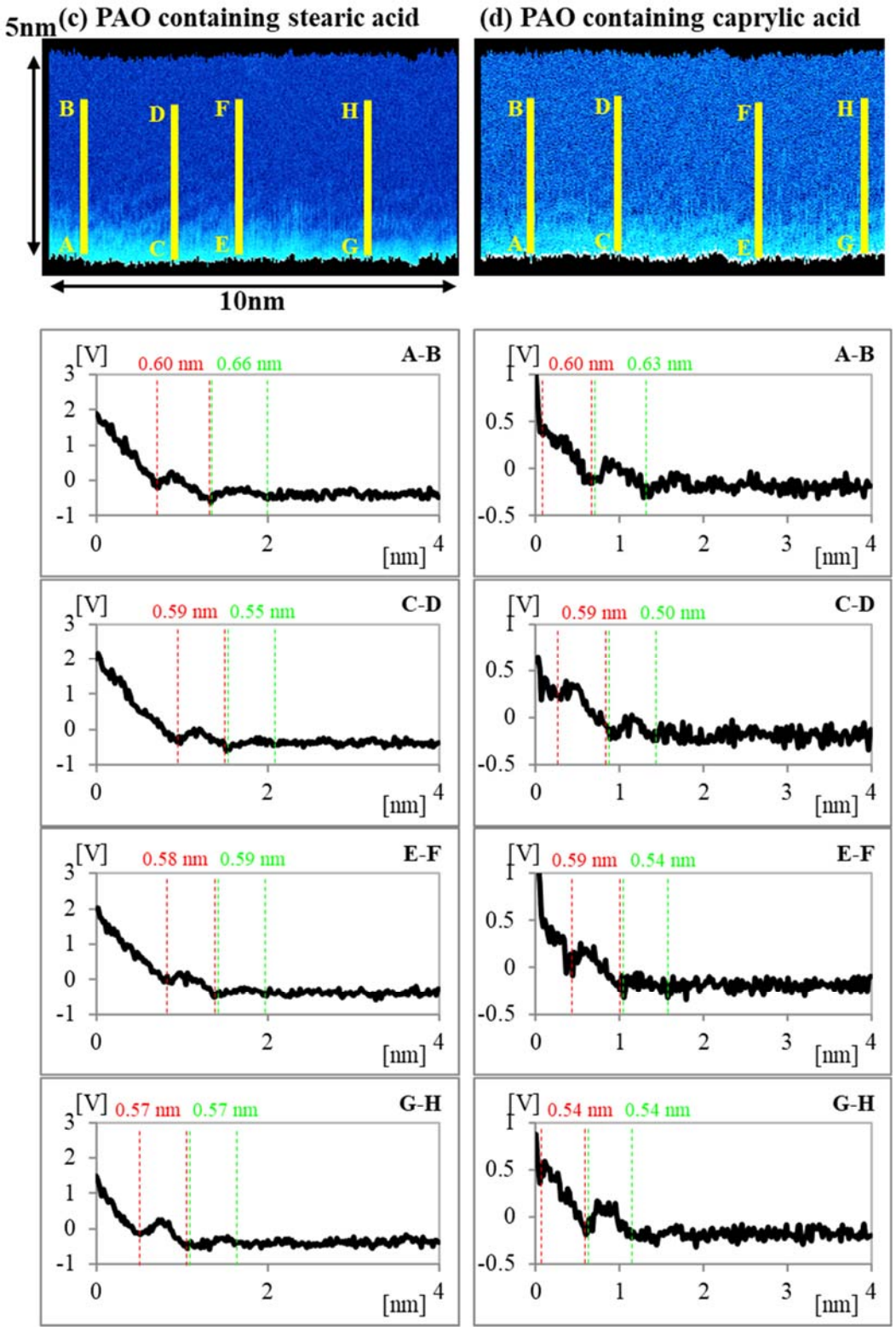

Figure 3.3.9 The cross-sectional frequency shift distribution and frequency shift -distance curves in PAO containing (a) no modifier, (b) oleic acid, (c) stearic acid, (d)

caprylic acid. The amplitude of the cantilever oscillation was 0.4 nm. The aspect ratio of the lateral and vertical scales has been tuned unity in the maps. A large (or small) positive frequency shift is depicted using a bright (or dark) blue color. Sixteen frequency shift –distance curves shown in the panel below the images are the average profile curve on the white lines containing 10 lines. The distance between the first and second layer is written in red. The distance between the second and third layer is written in green.

Table 3.3.1 The average of the layer-to-layer distances measured at four different positions.

	First - Second	Second - Third
PAO	0.61 nm	0.59 nm
PAO containing oleic acid	0.75 nm	0.68 nm
PAO containing stearic acid	0.59 nm	0.59 nm
PAO containing caprylic acid	0.58 nm	0.56 nm

The layer-to-layer distances was about 0.6 nm in the observed map except for PAO containing oleic acid. Layer-to-layer distances around 0.6 nm have been observed earlier studies, where single-chain hydrocarbons like hexadecane were put on atomically flat solids. The thickness of single-chain hydrocarbons is expected to be 0.6 nm. Therefore, the layer-to-layer distances of 0.6 nm suggested single-chain hydrocarbons of PAO, stearic acid and caprylic acid molecules lying flat on the surface. In PAO containing oleic acid, the layer-to layer distance was 0.72 nm and tended to be longer than in the other lubricants. The reason for longer distance between layers is that oleic acid molecules have a bent structure and are larger on the short side of the molecule than stearic acid or caprylic acid molecules which have a

linear chain. These results suggested that the layer structure was constructed not only by PAO molecules but also by modifier molecules. The molecular behavior inferred from the frequency-shift maps is shown in Figure 3.3.10. As illustrated in Chapter 2, the illustrations of a molecule colored in yellow were drawn assuming that the molecule has an all-trans formation. The local unevenness seen in the topographic image was adsorption promoted by AFM scanning, i.e., pseudo sliding. Since these frequency-shift maps were measured without sliding, it is not surprising that the adsorption layers were uniformly distributed.

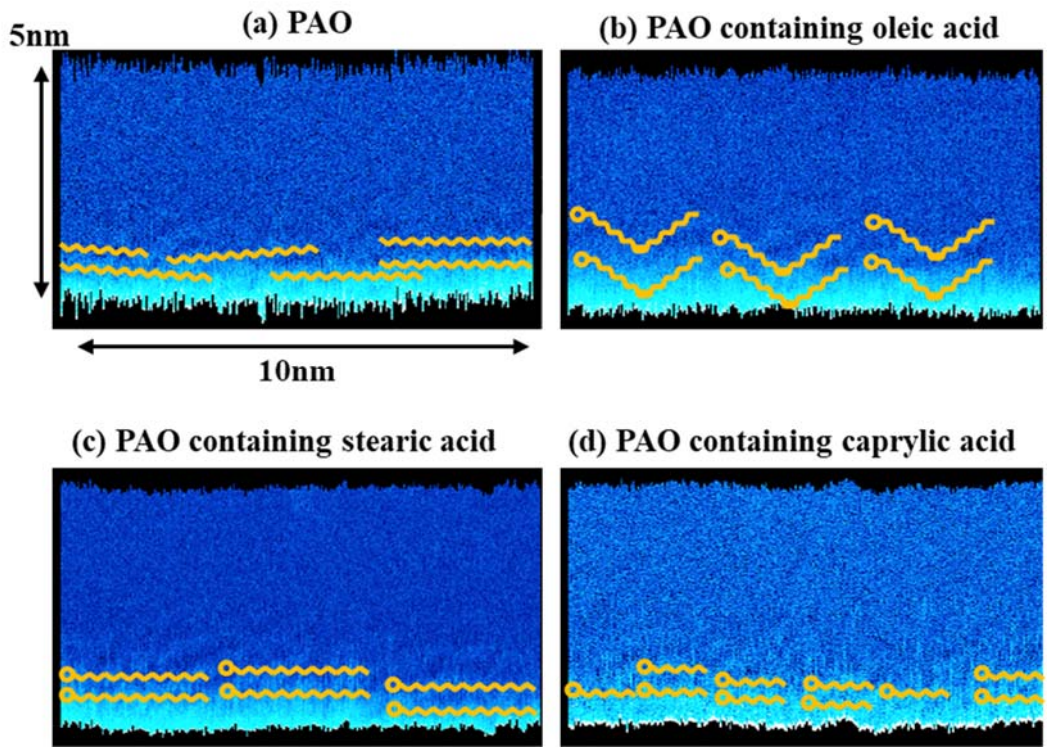

Figure 3.3.10 The molecular behavior inferred from these images of frequency shift

In the previous experiments in this subsection, the structure of the liquid lubricants at the interface between lubricants and the iron oxide single-crystalline wafers was observed. Since the behavior of the modifier molecules just above the solid surface is considered to be important at the lubrication interface, the frequency shift distribution

image on the plane perpendicular to the surface of iron oxide single-crystalline wafer was measured by scanning the oscillation probe in a region closer to the iron oxide single-crystalline wafers than in the previous experiments. The relationship of the scanning region of the previous experiments and the subsequent experiments is shown in Figure 3.3.11. In the previous experiment in this subsection, area 1 was scanned, and in the subsequent experiments, area 2 was scanned.

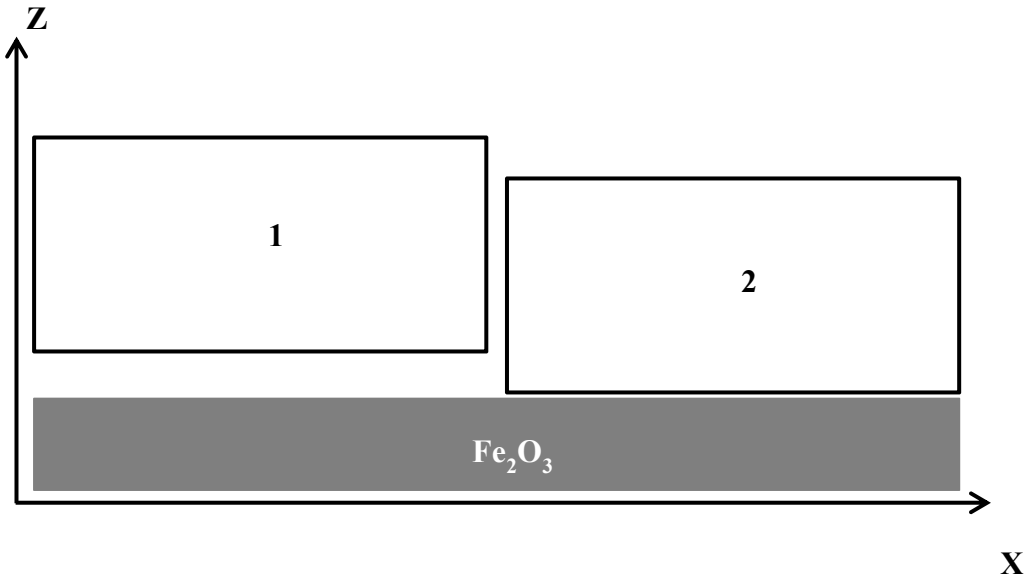

Figure 3.3.11 The scanning area in the previous experiments and in the subsequent experiments.

Figure 3.3.12 shows the frequency-shift maps observed on the iron oxide single-crystalline wafer immersed in pure PAO. The oscillating cantilever was scanned vertically from the bulk PAO to the iron oxide single-crystalline wafers. The frequency shift as a function of the vertical coordinate was simultaneously recorded to obtain one frequency shift-distance curve composed of 256 pixels at one lateral position. The vertical scan was aborted when the probe reached an end of scan range in z direction, and the cantilever was retracted into PAO by 5 nm. 256 vertical scans

along a 10 nm long lateral coordinate were acquired repeatedly. One frequency-shift map was subsequently constructed on a plane perpendicular to the iron oxide single-crystalline wafer with an acquisition time of 26 seconds for 256 scans per frame. Bright color represents large positive frequency shift. Dark blue color shows small positive or even negative frequency shifts, while areas outside the scanned range are shown in black. When the tip moved from the PAO liquid to the iron oxide surface, force on the tip modulated somehow as shown with bright or less bright blue colors. Finally, when the tip approaches the surface, large repulsive force is present due to tip-surface contact, as shown by the very bright color at the bottom of image. So, the boundary of the very bright area and blue-colored area represents the PAO-solid interface. If the PAO liquid density was uniform over the interface, force on the tip, that is blue-color strength should be uniform. However, this was not the case. Force on the tip was modulated to show layered feature parallel to the interface. The layered force modulation evidenced layered modulations of PAO liquid density.

The observed layered modulations could be interpreted with liquid PAO molecules lying parallel to the interface. The layer-to-layer distances was 0.6 nm in the observed map. Layer-to-layer distances around 0.6 nm have been observed earlier studies, where single-chain hydrocarbons like hexadecane were put on atomically flat solids. The thickness of single-chain hydrocarbons is expected to be 0.6 nm. Figure 3.3.13 shows the molecular behavior inferred from the frequency-shift map observed on the iron oxide wafer immersed in the pure PAO.

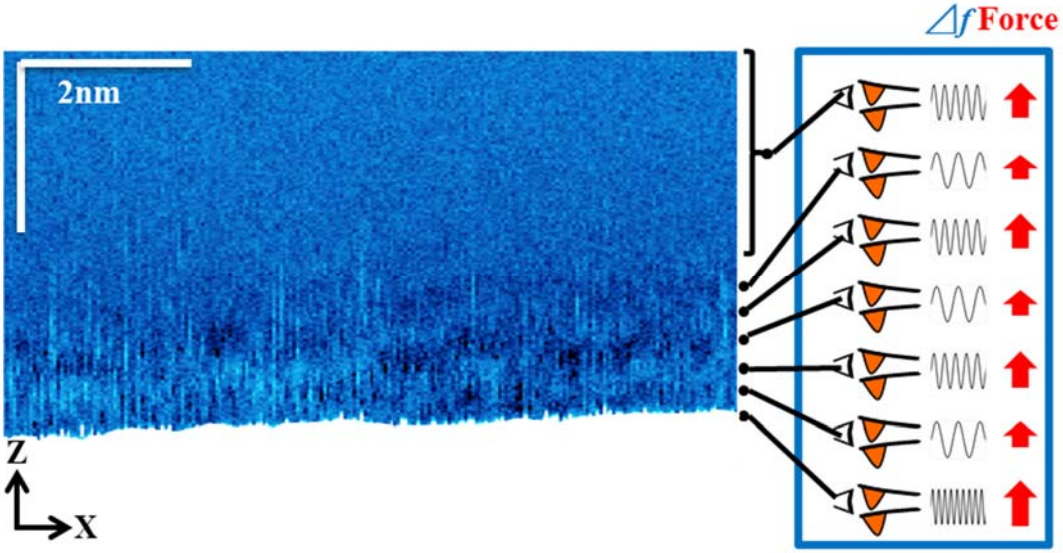

Figure 3.3.12 Frequency-shift map observed on the iron oxide wafer immersed in the pure PAO. The amplitude of the cantilever oscillation was 0.4 nm. The aspect ratio of the lateral and vertical scales has been tuned unity in the maps. A large (or small) positive frequency shift is depicted using a bright (or dark) blue color.

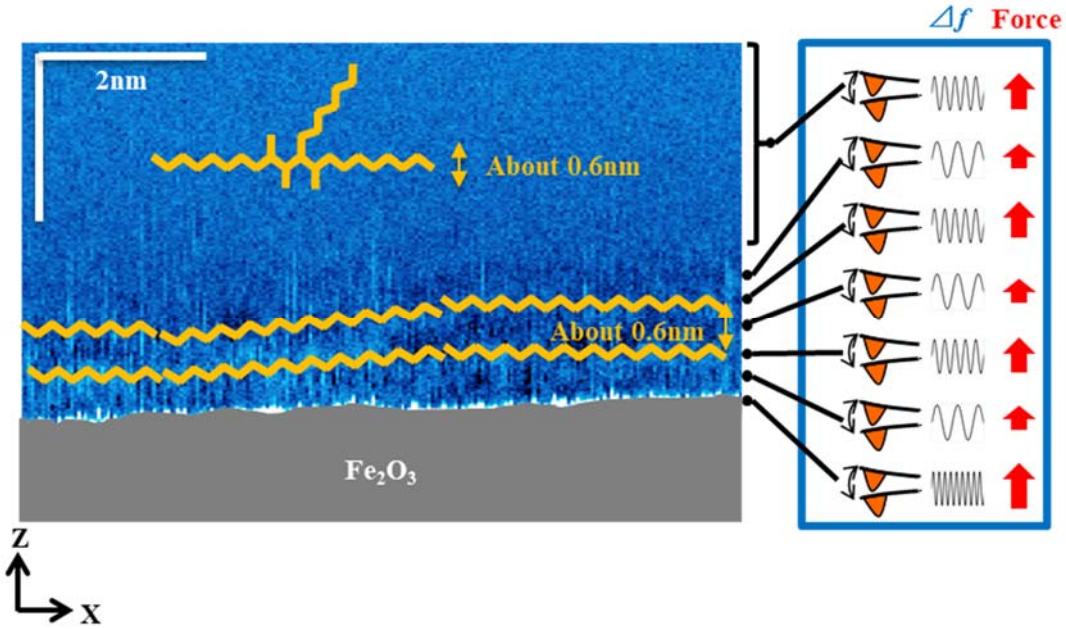

Figure 3.3.13 The molecular behavior inferred from the frequency-shift map observed on the iron oxide wafer immersed in the pure PAO.

What happened with an modifier, two-ethyl-hexanoic acid. Figure 3.3.14 shows the frequency-shift maps observed on the iron oxide single-crystalline wafer immersed in the PAO containing two-ethyl-hexanoic acid. The layered feature recognized in the pure PAO has gone. Instead, repulsive force appeared as shown by more bright colors in the proximity to the interface. The very bright color at the bottom again indicated the liquid-solid interface. Disappeared layers suggested the PAO liquid was not directly exposed to the iron oxide.

The size of two-ethyl-hexanoic acid is projected on the observed frequency-shift map. When we assume that the acid molecules were chemically adsorbed on the iron oxide, the two alkyl tails, one containing five carbon atoms and the other with three carbon atoms, should be in the lubricant liquid. The alkyl chains should fluctuate in the lubricant liquid to produce repulsive force when being in contact to the tip apex. The length of repulsive force was about 1 nm. This length corresponds to the molecular length of the acid. Based on these considerations, we claim here that the iron oxide was covered by a monolayer of two-ethyl-hexanoic acid molecules. The presence or absence of the monolayer, as well as its thickness, was visualized in frequency-shift mapping. Figure 3.3.15 shows the molecular behavior inferred from the frequency-shift map observed on the iron oxide wafer immersed in the PAO containing two-ethyl-hexanoic acid.

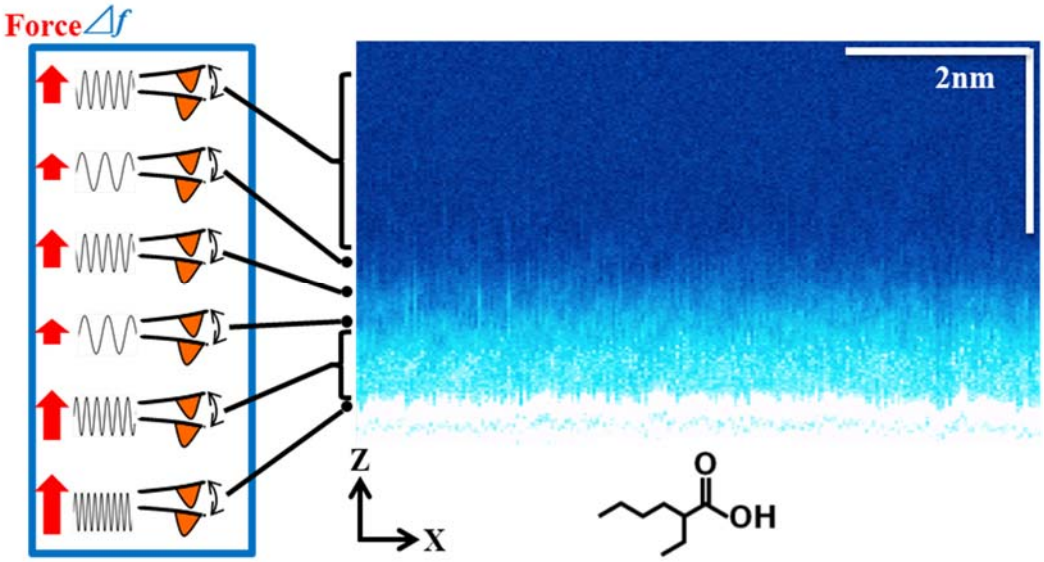

Figure 3.3.14 Frequency-shift map observed on the iron oxide wafer immersed in the PAO containing two-ethyl-hexanoic acid. The amplitude of the cantilever oscillation was 0.4 nm. The aspect ratio of the lateral and vertical scales has been tuned unity in the maps. A large (or small) positive frequency shift is depicted using a bright (or dark) blue color.

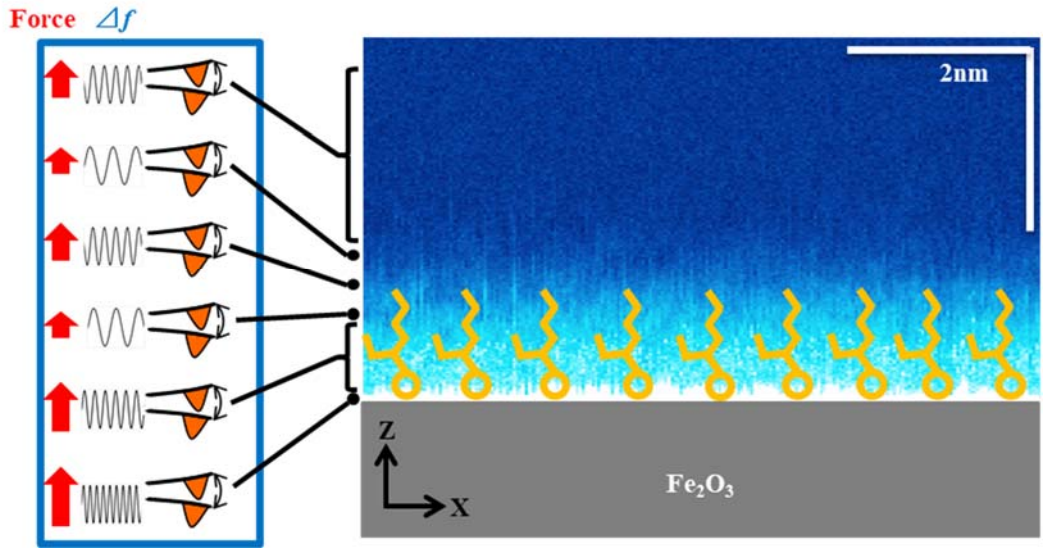

Figure 3.3.15 The molecular behavior inferred from the frequency-shift map observed on the iron oxide wafer immersed in the PAO containing two-ethyl-hexanoic acid.

Figure 3.3.16 shows a frequency-shift map observed in the lubricant containing oleic acid. The map was similar to what was observed with the hexanoic acid. The layered feature coming from PAO was weakened, and repulsive force shown by more bright colors appeared in the proximity to the interface. This is a sign of the iron oxide covered by adsorbed oleic acid molecules. One issue to be interpreted is the thickness of the region where the repulsive force appeared. The thickness was 1 nm or less, while an oleic acid has a alkyl chain of 17 carbon atoms. The length of the chain is much longer than that in two-ethyl-hexanoic acid.

One possible picture is shown in Figure 3.3.17. Oleic acid was chemically adsorbed with its polar group on the iron oxide to form a densely packed monolayer. The monolayer was rigid enough to be recognized as a solid. Only the end of the chains fluctuated in the lubricant present the repulsive force to the tip.

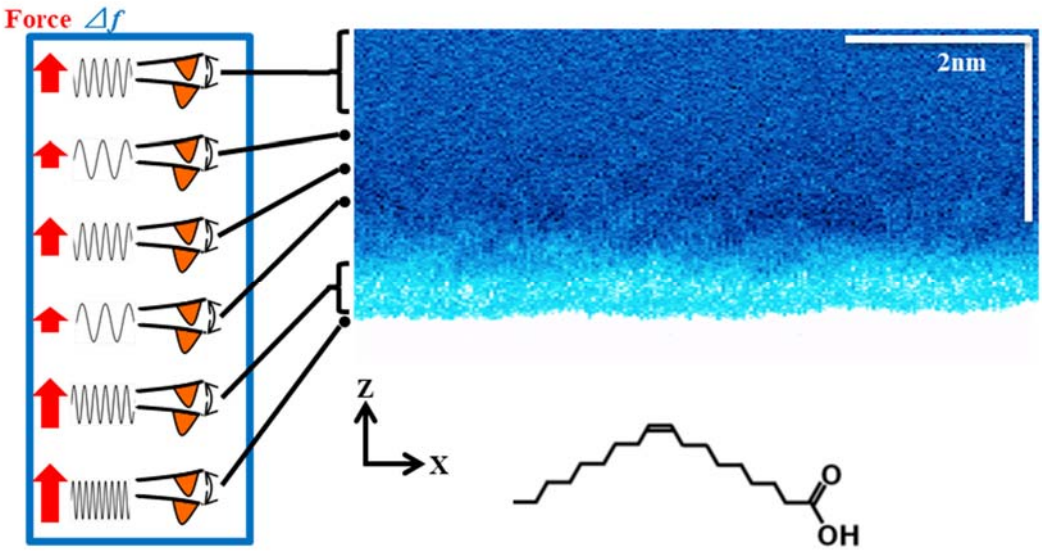

Figure 3.3.16 Frequency-shift map observed on the iron oxide wafer immersed in the PAO containing oleic acid. The amplitude of the cantilever oscillation was 0.4 nm. The aspect ratio of the lateral and vertical scales has been tuned unity in the maps. A large (or small) positive frequency shift is depicted using a bright (or dark) blue color.

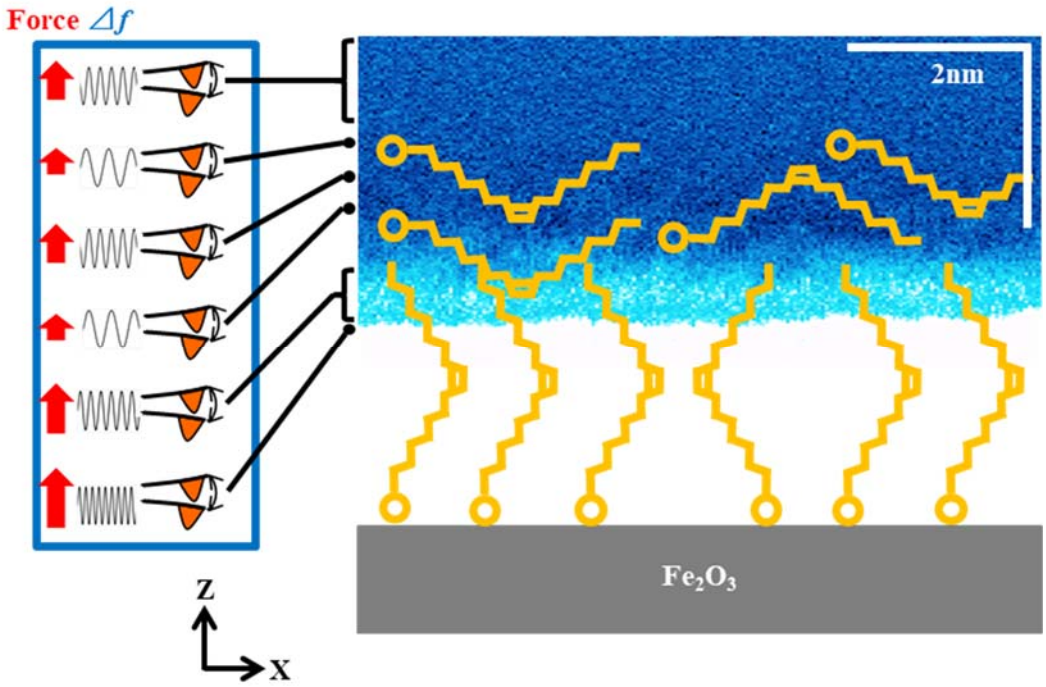

Figure 3.3.17 The molecular behavior inferred from the frequency-shift map observed on the iron oxide wafer immersed in the PAO containing oleic acid.

As with the three lubricants mentioned above, a total of six lubricants were examined. The results are summarized in Figure 3.3.18, which shows frequency-shift map observed on the iron oxide wafer immersed in the PAO containing (a) no modifier, (b) two-ethyl-hexanoic acid, (c) oleic acid, (d) stearic acid, (e) elaidic acid, (f) caprylic acid. The layered features with layer-to-layer distance of 0.6 nm were most clearly recognized in the pure PAO, weakly recognized in PAO containing oleic, stearic and elaidic acids, respectively, and were absent in the presence of two-ethyl-hexanoic acid. In the previous experiments, it was confirmed that these layered features were constructed not only by PAO molecules but also by modifier molecules. Furthermore, as seen in PAO containing two-ethyl-hexanoic acid and oleic acid respectively, in PAO containing modifiers, repulsive force shown by more bright colors appeared in the proximity to the interface. As considered for the results of PAO

containing 2-ethyl-hexanoic acid and oleic acid respectively, this repulsive force is expected to be the contact force from the end of the alkyl chains of the modifier molecules chemically adsorbed on the surface of the iron oxide single-crystalline wafer, and the alkyl chains fluctuated in the lubricant. From the difference in molecular structure between five kinds of modifiers, it is predicted about this repulsive force as follows. Stearic acid was adsorbed on the iron oxide to form the most densely packed monolayer. Even the end of the alkyl chain was rigid enough to be recognized as a solid, so the layer of repulsive force shown in light blue color at the bottom of the frequency-shift map was thin and not uniform. Because oleic acid molecule and elaidic acid molecule have a double bond between carbon atoms and caplylic acid molecule is shorter than stearic acid molecule, they formed less densely packed monolayer than stearic acid. As the result, the end of their alkyl chain was more flexible than it of stearic acid, and the probe could penetrate the monolayer at a longer distance. Two-ethyl-hexanoic acid has a more complex structure than the other five. So it could not form a densely packed monolayer, then the probe could penetrate the monolayer at the distance as long as the molecular length. S. Loehle et al. evaluated the adsorption of stearic, oleic, and linoleic acids on iron oxide surfaces using MD simulations and reported that the main adsorption mechanism of fatty acids on iron oxide surfaces is chemisorption by carboxyl groups. In addition, it was reported that stearic acid, a saturated fatty acid, forms a close-packed monolayer, and double carbon bonds of unsaturated fatty acids oleic and linoleic acid prevent the formation of close-packed monolayers[6]. The frequency shift image in this study also supports it. Figure 3.3.19 shows the molecular behavior inferred from these frequency-shift maps observed on the iron oxide single-crystalline wafers immersed in six kinds of lubricants. The iron oxide single-crystalline wafers were described in these frequency-shift maps. They were drawn back counting from the end of the

molecules. For example, in the case of stearic acid, there is a light blue layer on the left side of the frequency-shift map indicating the contact resistance force from the end of the stearic acid molecules fluctuated in the lubricant. But there is no light blue layer on the right side, and it indicates that the end of the stearic acid molecules was rigid enough to be recognized as a solid. Since all the stearic acid molecules have the same length, assuming the wafer surface was horizontal, the light blue layer on the left should be below the boundary between the blue and white regions on the right. But it was upper the boundary. Therefore, it must be considered that the wafer surface was inclined.

The frequency shift images indicated that stearic acid in the carboxylic acids used in this study forms the most densely packed monolayer. Among carboxylic acids, stearic acid has been reported to provide the best tribological behavior compared with other carboxylic acids such as oleic acid and elaidic acid[7, 8, 9]. That is, it can be seen that the more densely packed monolayer has a higher friction reduction effect.

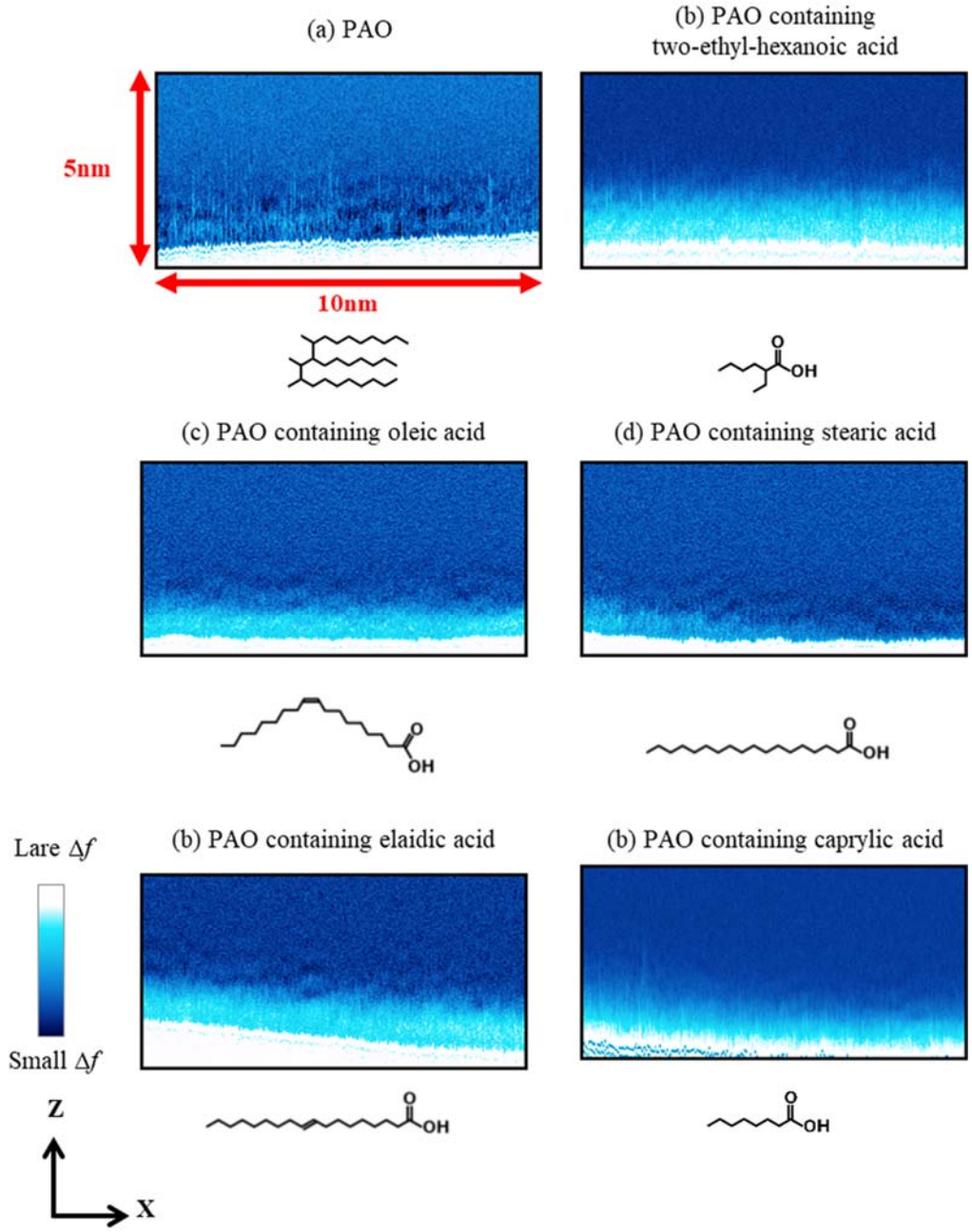

Figure 3.3.18 Frequency-shift map observed on the iron oxide wafer immersed in the PAO containing (a) no modifier, (b) two-ethyl-hexanoic acid, (c) oleic acid, (d) stearic acid, (e) elaidic acid, (f) caprylic acid. The amplitude of the cantilever oscillation was 0.4 nm. The aspect ratio of the lateral and vertical scales has been tuned unity in the maps. A large (or small) positive frequency shift is depicted using a bright (or dark) blue color.

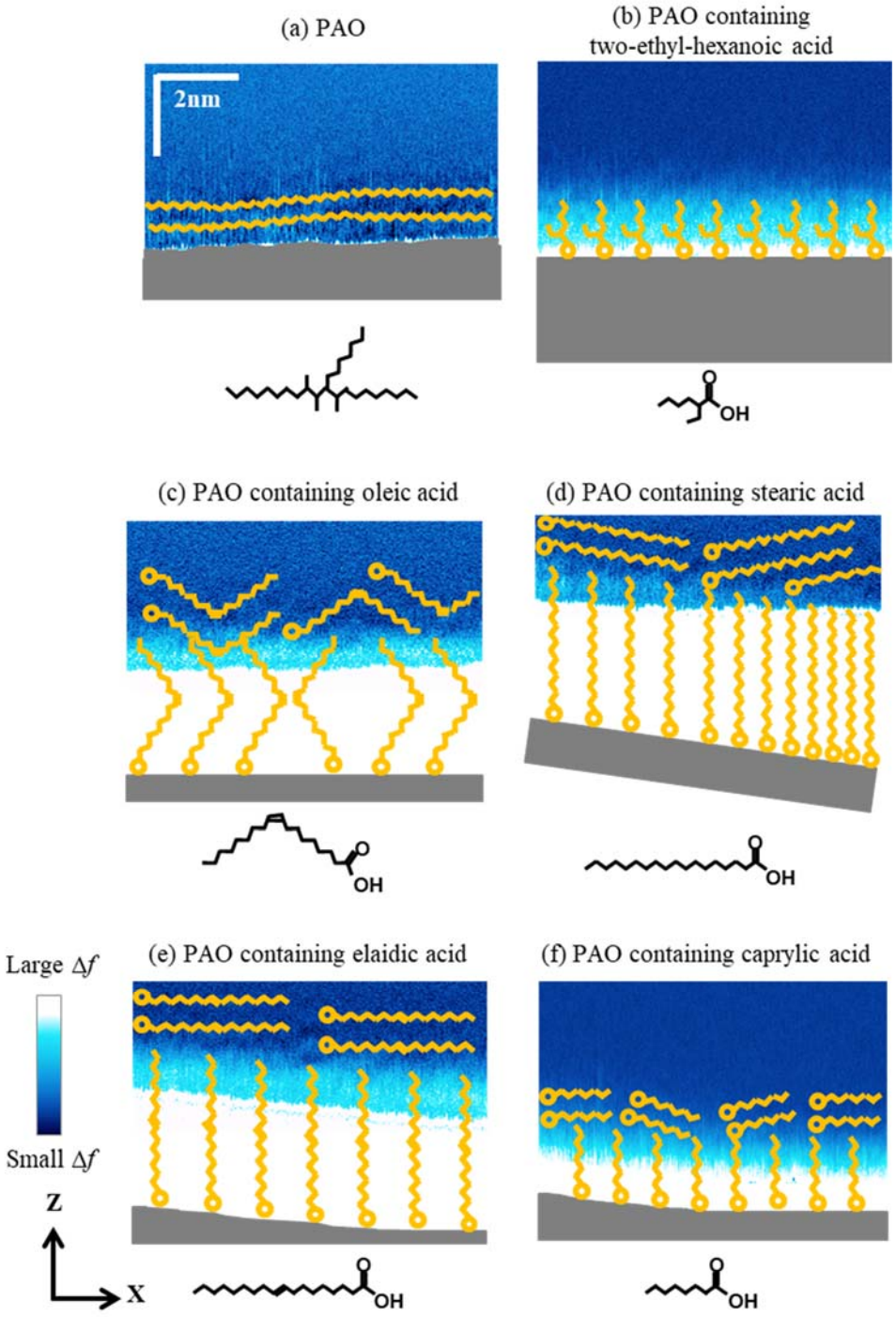

Figure 3.3.19 The molecular behavior inferred from the frequency-shift map observed on the iron oxide wafer immersed in the PAO containing (a) no modifier, (b) two-ethyl-hexanoic acid, (c) oleic acid, (d) stearic acid, (e) elaidic acid, (f) caprylic acid.

3.3.2 Analysis by FM-AFM under heating

3.3.2.1 Back ground

Oleic acid is known to be effective at relatively low temperatures. It is reported that oleic acid molecules are desorbed from the metal surface at high temperatures around 150 degrees centigrade, so lose its effect[6]. One of the advantages of SPM measurement is working well in various atmospheres such as vacuum, air, and liquid. It is also possible to conduct measurements while heating and cooling the sample[10-13]. Here, temperature-dependent changes in the adsorption of oleic acid molecules to iron oxide single-crystal wafers were evaluated, taking advantage of the SPM measurement, in which samples can be observed during heating.

3.3.2.2 Methods

Setting for the observation under heating is shown in Figure 3.3.20. For heating the lubricant, a ceramic heating devise was inserted just beneath the dish. Two cables were for resistance heating and three more cables on the right were for sensing the temperature at the dish bottom. A small petri dish was placed on this stage.

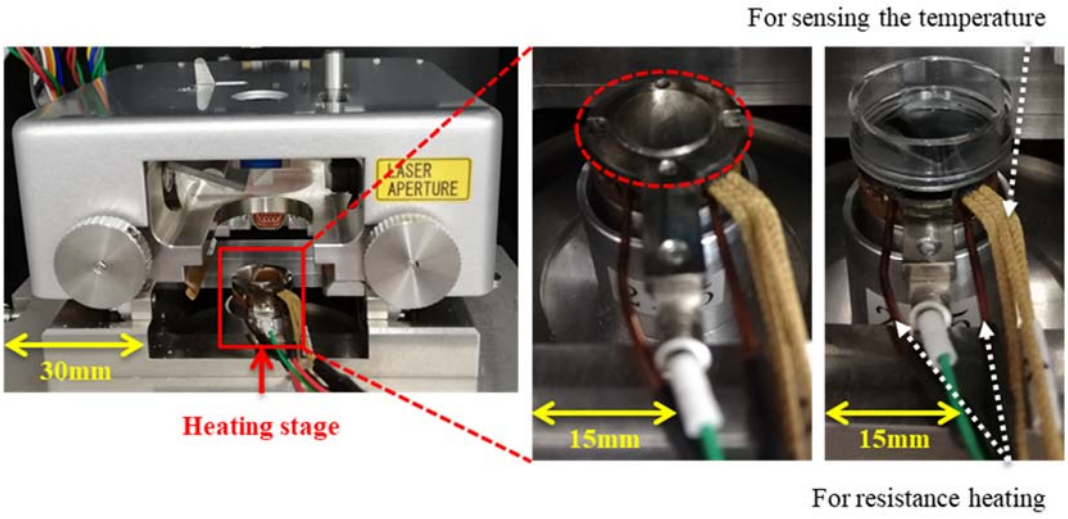

Figure 3.3.20 Setting for the measurement under heating

3.3.2.3 Force mapping

The results are shown in Figure 3.3.21. The frequency shift as a function of the vertical coordinate was simultaneously recorded to obtain one frequency shift-distance curve composed of 256 pixels at one lateral position. The vertical scan was aborted when frequency shift reached a predetermined threshold (+1000 Hz for the acquired maps in Figure 3.3.21); the cantilever was retracted into the lubricant by 30 nm to prevent extensive tip-to-surface contact. 256 vertical scans along a 300 nm long lateral coordinate were acquired repeatedly. One frequency-shift map was subsequently constructed on a plane perpendicular to the iron oxide single-crystalline wafer with an acquisition time of 26 seconds for 256 scans per frame. Bright color represents large positive frequency shift. Dark blue color shows small positive or even negative frequency shifts, while areas outside the scanned range are shown in black. The white line below the blue band is the return point of the vertical scan and indicates contact with the solid.

The left images were observed in the pure PAO. The two images in the right were observed in the PAO containing oleic acid. The upper images were observed at room temperature, and the lower images were measured at 60 degrees centigrade. At room temperature, a bright blue layer indicated the adsorption of oleic acid molecules. On the other hand, at 60 degrees centigrade, regardless of the presence and absence of oleic acid, the bright blue layer was absent. The disappearance of the bright blue layer suggested that oleic acid was desorbed from the iron oxide at 60 degrees centigrade.

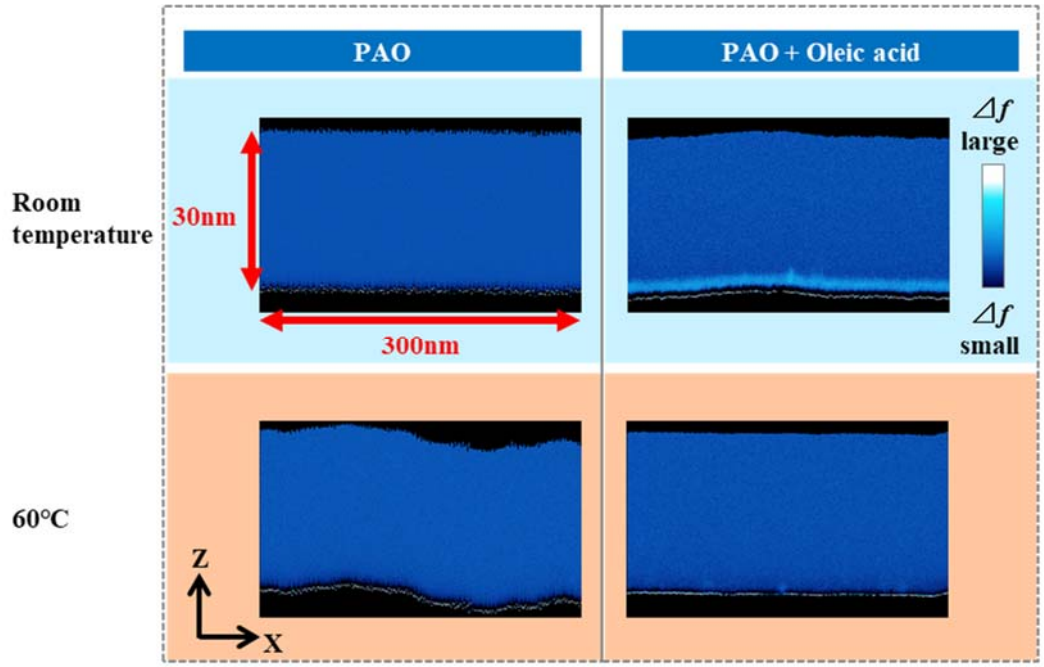

Figure 3.3.21 Lubricants over the iron oxide single-crystalline wafers. The cross-sectional frequency shift distribution was mapped on a plane that was perpendicular to the wafer surface in the pure PAO (two images on the left) and lubricant containing oleic acid with a concentration of 1 mm/kg (two images on the right). The upper images were observed at room temperature, and the lower images were measured at 60 degrees centigrade. The amplitude of the cantilever oscillation was 0.8 nm. The scan range is 30 nm in z direction and 300 nm in x direction.

From these measurements, it was predicted that the end of the oleic acid molecules become so flexible enough not to apply the repulsive force to the tip, or that the oleic acid molecules are desorbed from the iron oxide single-crystalline wafer at 60 degrees centigrade. In order to confirm how did this change proceed, measurements were made at 5 degrees centigrade increments from 25 degrees centigrade to 65 degrees centigrade.

The results are shown in Figure 3.3.22. As in the previous experiment in this subsection, the frequency shift as a function of the vertical coordinate was

simultaneously recorded to obtain one frequency shift-distance curve composed of 256 pixels at one lateral position. The vertical scan was aborted when frequency shift reached a predetermined threshold (+1000 Hz for the acquired maps in Figure 3.3.22); the cantilever was retracted into the lubricant by 30 nm to prevent extensive tip-to-surface contact. 256 vertical scans along a 300 nm long lateral coordinate were acquired repeatedly. One frequency-shift map was subsequently constructed on a plane perpendicular to the iron oxide single-crystalline wafer with an acquisition time of 26 seconds for 256 scans per frame. Then, images of 15 nm in the vertical direction and 150 nm in the horizontal direction shown in Figure 3.3.22 were cut out from the measured frequency-shift maps. These images were measured as the temperature increases by 5 degrees centigrade from 25 degrees centigrade to 40 degrees centigrade from the upper left to the lower left, and from 45 degrees centigrade to 65 degrees centigrade from the upper right to the lower right. PAO and PAO containing oleic acid was used as a lubricant.

The light blue layer, which shows the adsorption of oleic acid molecules on the iron oxide single-crystalline wafer, gradually darkens from 25 degrees centigrade to 40 degrees centigrade. It gradually disappeared from 40 degrees centigrade to 55 degrees centigrade and completely disappeared at 60 degrees centigrade. Disappearance of the light blue layer suggests the desorption of the modifier molecules from the iron oxide single-crystalline wafer or activation of modifier adsorption.

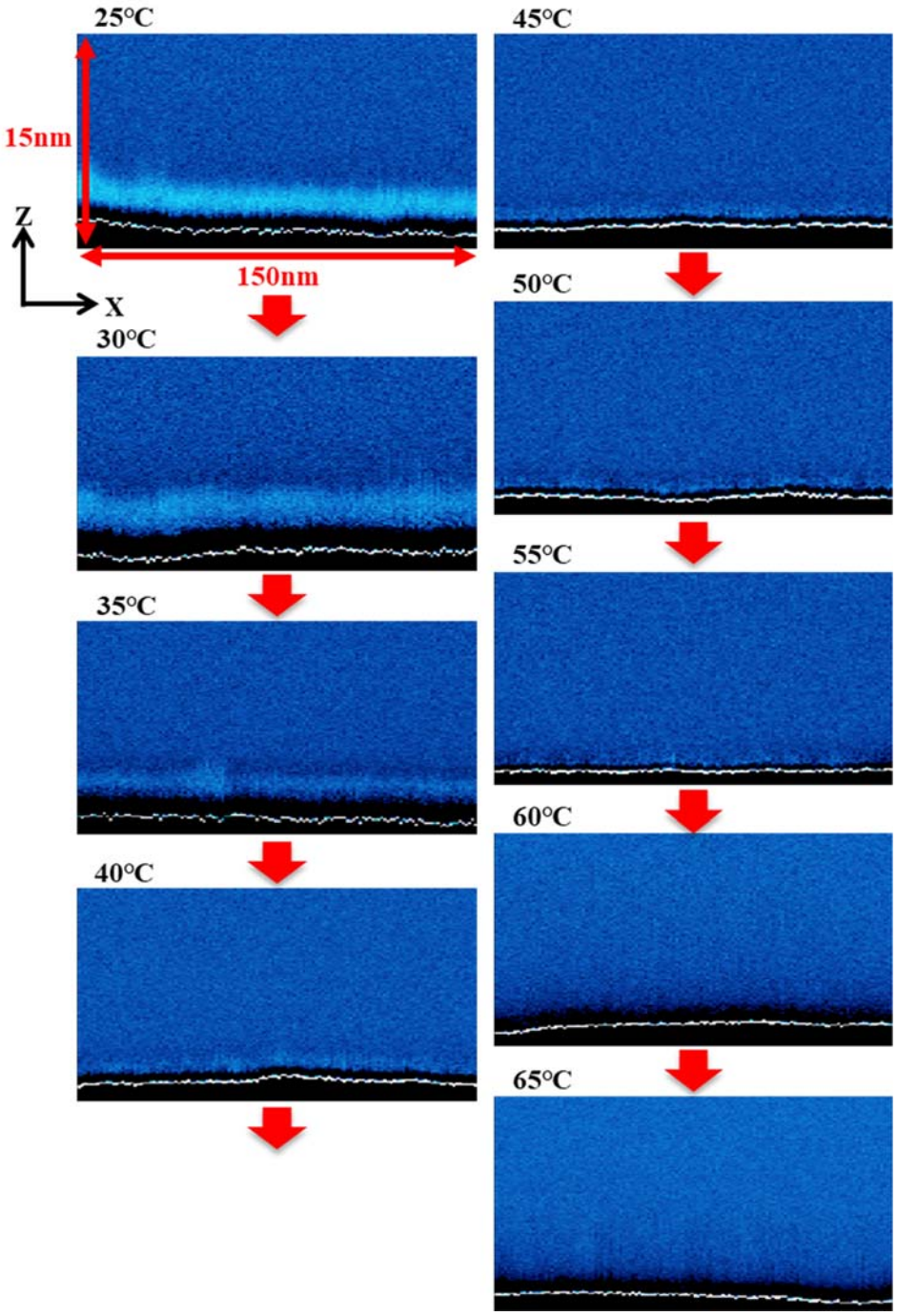

Figure 3.3.22 The images of the frequency-shift distribution on the plane perpendicular to the iron oxide single-crystalline wafer surface as the temperature increases by 5 degrees centigrade from 25 degrees centigrade to 65 degrees centigrade. The amplitude of the cantilever oscillation was 0.8 nm. The scan range is 30 nm in z direction and 300 nm in x direction.

3.3.3 Evaluation of the friction coefficient by a ball on disk friction tester under heating

3.3.3.1 Methods

The friction coefficient was evaluated with an FPR-2100 ball on disk friction tester (RHESCA). The load was adjusted to 50 g. Sliding trajectory was circular. The ball slid on the surface of the disk at a linear velocity of 1 mm/sec for 300 sec. The ball was made of carbon steel (SUJ2). The same kind of iron oxide single-crystalline wafer used for the analysis by FM-AFM was used as the disk. The balls were washed with acetone before setting and replaced with new ones at each measurement. The friction tests were conducted for two kinds of lubricants at different temperatures. One lubricant was PAO, and the other was PAO containing oleic acid with a concentration of 1 mmol/kg. In the friction test for PAO, the temperature was raised in 5 degree centigrade increments from room temperature to 90 degrees centigrade. Besides, the friction test was also conducted at 150 degrees centigrade. For PAO containing oleic acid with a concentration of 1 mmol/kg, the temperature was raised step in 5 degree centigrade increments from room temperature to 75 degrees centigrade. The radius of the sliding trajectory differed by at least 0.1 mm in each test. The radius of the contact area is calculated to be 0.018 mm, so the difference of 0.1 mm in the radius of the sliding trajectory is sufficient. The calculation of the contact area radius is described in Section 3.6.1.

3.3.3.2 Friction coefficient at different temperatures

Figure 3.3.24 shows the friction coefficients at different temperatures. A friction coefficient versus time graph for each temperature is shown in Figure 3.6.2 to Figure 3.6.27 in the Supporting Information. The average value after 150 seconds when the friction coefficient started to stabilize is shown in Figure 3.3.16. From room

temperature to 75 degrees centigrade, the friction coefficient of PAO containing oleic acid was smaller than that of PAO. At 150 degrees centigrade, the friction coefficient of PAO containing oleic acid was almost the same as that of PAO. This result suggests that oleic acid was adsorbed to the surface of iron oxide single-crystalline wafers and has the effect of reducing friction at temperatures below 90 degrees centigrade, but desorbed from the wafers at 150 degrees centigrade.

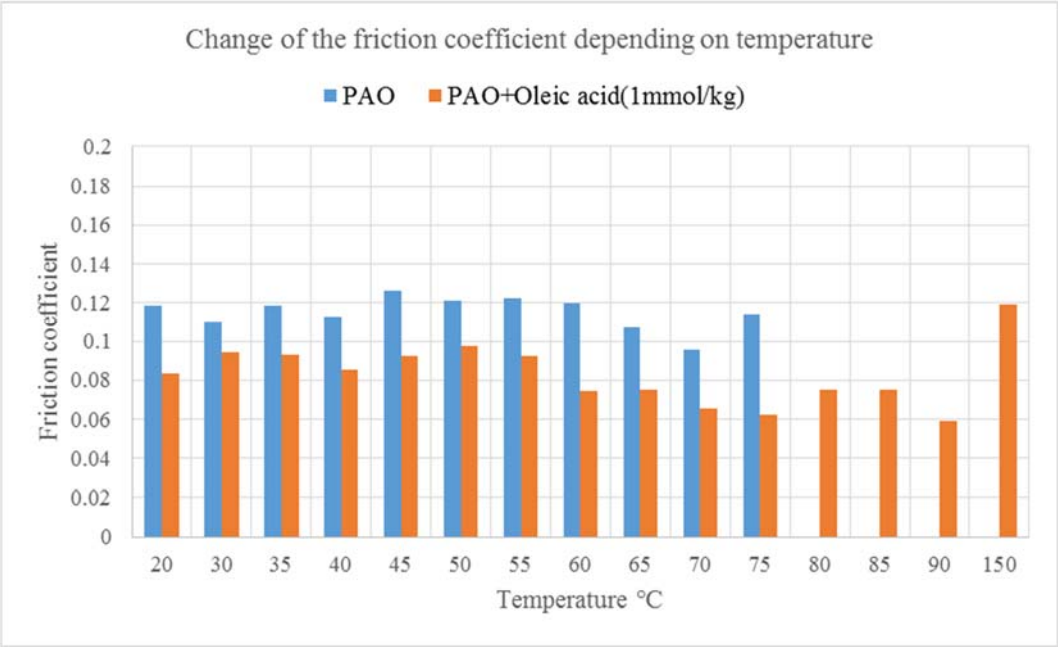

Figure 3.3.23 Friction coefficients at different temperatures

About the effects of reducing the friction by carboxylic acids, F. P. Bowden et al. reported in 1950 that the friction was reduced under conditions that allowed carboxylates to form on the metal surface[14]. M. Ratoi et al. reported in 2000 that the presence of water molecules greatly affects the formation of carboxylates, and when water molecules are present, Fe is oxidized to Fe (II) and Fe (III), which promotes the thickening of carboxylates layers[15]. R. Simie et al. reported in 2013 that stearate formation was induced in the presence of friction[16]. As in the previous studies introduced here, it is generally believed that the friction-reducing effects of carboxylic

acid are due to the carboxylates, and its effect is lost at high temperatures because the carboxylates dissolve. On the other hand, S. Loehle et al. reported that the formation of stearate is not observed in their quantum chemical calculations without friction, even at 150 degrees centigrade. It was also concluded that stearic acid, oleic acid, and linolenic acid did not desorb from iron oxide even at 150 degrees centigrade[6]. There are a number of parameters to consider, such as concentration, temperature, and type of base oil, the mechanism of the friction-reducing by carboxylic acid is still carefully discussed. The results obtained in this study are also one of the materials to consider the mechanism of the friction-reducing by carboxylic acid.

3.4 Conclusion

We demonstrated the feasibility of using FM-AFM for mechanically probing a lubricant-solid interface, carboxylic acid-containing PAO covering the iron oxide single-crystalline wafers. For PAO containing carboxylic acid, as same as PAO containing C18AP, we mapped the lubricant-induced force on the probing tip two-dimensionally on a plane that was perpendicular to the lubricant–iron interface and thus achieved a force sensitivity and spatial resolution on the order of 10 pN and 10 pm, respectively.

We propose the following conclusions after interpretation of the observed topographic images. In the topographic measurement, pseudo sliding was caused by the interaction force generated when the probe was scanned on the surface of the iron oxide single-crystalline wafer. It was found that adsorption of the carboxylic acid on the wafer is promoted by sliding.

We propose the following conclusions after interpretation of the observed force maps. The PAO was directly exposed to the surface of the iron oxide single-crystalline wafer in the absence of the carboxylic acid modifier, and it exhibited a few liquid layer parallel to the wafer surface with a layer-to-layer distance of 0.6 - 0.7 nm. Carboxylic acid, if any in the lubricant, was adsorbed with its polar group end anchored to the wafers. There was fluctuation of single-chain hydrocarbons of carboxylic acid in the lubricant. The force maps reflected the time-averaged density distribution of the fluctuating chains and monotonically decayed to zero force at a tip-to-surface distance of 0.6 nm - 1 nm when a monomolecular layer of carboxylic acid was completed. The distance at which the force decays to zero depended on the molecular structure of the carboxylic acid. Besides, the carboxylic acid in the

lubricant formed the liquid layered structure on the monolayer with a layer-to-layer distance of 0.56 - 0.75 nm.

In addition, the temperature dependence of the modifier adsorption on the iron oxide single-crystalline wafer was verified by measuring the frequency-shift maps at temperatures from 25 degrees centigrade to 65 degrees centigrade. The area where the repulsive force decayed monotonously, that indicates the modifier adsorption to the iron oxide single-crystalline wafer, became thinner with increasing temperature, and disappeared at 60 degrees centigrade. This suggests the desorption of the modifier molecules from the iron oxide single-crystalline wafer or activation of modifier adsorption. The dynamic friction coefficient of the sliding steel–lubricant–iron oxide single-crystalline wafer interfaces, which was determined using the ball on disk friction tester at each temperature from 25 degrees centigrade to 150 degrees centigrade, increased at 150 degrees centigrade compared with it from 25 degrees centigrade to 90 degrees centigrade. From the frequency-shift maps measured by FM-AFM and the dynamic friction coefficient measured by a friction tester, it was found that the carboxylic acid was still adsorbed on the iron oxide single-crystalline wafer at temperatures above 60 degrees centigrade, and although the friction-reducing effect was maintained, the adsorption was activated enough not to present contact force to the tip. The mechanical probing with FM-AFM provides a new knowledge on a molecular scale that cannot be found only from friction phenomena for sliding friction in the macroscopic dimensions.

3.5 Reference

(1) Friction and Wear of Engineering Materials, 1992, London

(2) Allen, C.M.; Drauglis, E. Boundary layer lubrication: monolayer or multilayer. *Wear*, 1969, *14*, 363-384.

(3) Gellman, A.J.; Spencer, N.D. Surface chemistry in tribology. *Proc. of the Institution of Mechanical Engineers J*, 2002, *216*, 443-461.

(4) Hardy, W.B.; Bircumshaw, I. -Boundary Lubrication.- Plane Surface and the Limitations of Amonton's Law. *Proc. R. Soc. London*, A, 1925, *108*, 1

(5) Bowden, F.P.; Tabor, D. The Friction and Lubrication of Solids, Oxford Univ. Press, 1950

(6) Loehle, S.; Matta, C.; Minfray, C.; Mogne, T.L.; Martin, J.M.; Iovine, R.; Obara, Y.; Miura, R.; Miyamoto, A. Mixed Lubrication with C18 Fatty Acids: Effect of Unsaturation. *Tribol.Lett*., 2014, *53*, 319-328.

(7) Sahoo, R. R.; Biswas, S. K. Frictional response of fatty acids on steel. *Journal of Colloid and Interface Science*, 2009, *333*, 707-718.

(8) Lundgren, S. M.; Ruths, M.; Danerlöv, K.; Persson, K. Effects of unsaturation on film structure and friction of fatty acids in a model base oil. *Journal of Colloid and Interface Science*, 2008, *326*, 530-536.

(9) Campen, S.; Green, J.; Lamb, G.; Atkinson, D. On the increase in boundary friction with sliding speed. *Tribol. Lett.*, 2012, *48(2)*, 237‑248.

(10) Wiedemair, J.; Serpe, M.J.; Kim, J.; Masson, J.F.; Lyon, L.A.; Mizaikoff, B.; Kranz, C. In-Situ AFM Studies of the Phase-Transition Behavior of Single Thermoresponsive Hydrogel Particles. *Langmuir*, 2007, *23*, 130-137.

(11) Brodowsky, H.M.; Boehnke, U.-C.; Kremer, F. Temperature Dependent AFM on Ferroelectric Liquid Crystalline Polymer and Elastomer Films. *Langmuir*, 1997, *13*, 5378-5382.

(12) Yarrow, F.; Kuipers, B.W.M. AFM study of the thermotropic behaviour of supported DPPC bilayers with and without the model peptide WALP23. *Chem.Phys.Lipids*., 2011, *164*, 9-15.

(13) Kaasgaard, T.; Leidy, C.; Crowe, J.H.; Mouritsen, O.G.; Jørgensen, K. Temperature-Controlled Structure and Kinetics of Ripple Phases in One- and Two-Component Supported Lipid Bilayers. *Biophys.J*., 2003, *85*, 350-360.

(14) Bowden, F.P.; Tabor, D. Friction and Lubrication of Solids. *Oxford Univ. Press.*, 1950

(15) Ratoi, M.; Anghel, V.; Bovington, C.; Spikes, H.A. Mechanism of Oiliness Additives. *Trib. Int.* 2000, *33*, 241-247.

(16) Simie, R.; Kalin, M. Adsorption mechanisms for fatty acids on DLC and steel studied by AFM and tribological experiments. *Appl. Surf. Sci.*, 2013, *283*, 460-470.

3.6 Supporting Information

3.6.1 The contact surface radius in the ball-on-disk friction test

The contact surface radius of the ball and the sample in the ball-on-disk friction test can be calculated from Equation 3.3.1 in the Hertz contact model:

$$\boldsymbol{a = \left(\frac{3}{4} R^* \frac{F}{E^*}\right)^{\frac{1}{3}}} \qquad 3.6.1$$

$$\boldsymbol{\frac{1}{R^*} = \frac{1}{R_1} + \frac{1}{R_2}} \qquad 3.6.2$$

$$\boldsymbol{\frac{1}{E^*} = \frac{1 - \upsilon_1^2}{E_1} + \frac{1 - \upsilon_2^2}{E_2}} \qquad 3.6.3$$

where a is the contact surface radius of the ball and the sample, F is load, and R_1, E_1 and υ_1 are the radius, Young's modulus and Poisson's ratio of the ball, and R_2, E_2 and υ_2 are the radius, Young's modulus and Poisson's ratio of the sample, respectively. Figure 3.3.23 shows a schematic diagram of a ball in contact with a plane assumed in Hertz contact model.

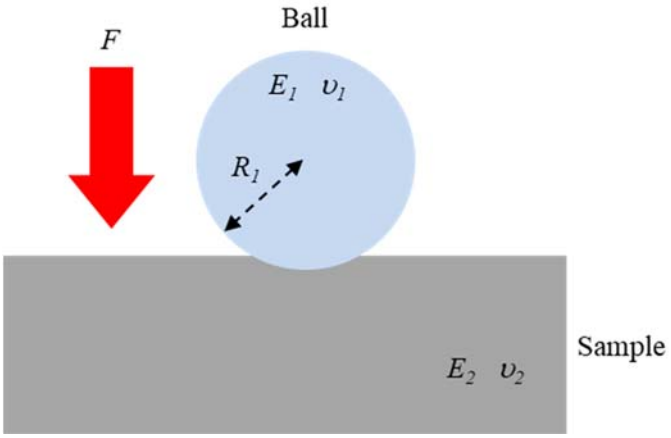

Figure 3.6.1 Schematic diagram of a ball in contact with a plane assumed in Hertz contact model

The values of the parameters in this friction test are as shown in Table 1. R_2 was assumed to be ∞ because the iron oxide single-crystalline wafers were plane. And Young's modulus of the iron oxide single-crystalline wafer was assumed to be the same as that of sapphire (Al2O3) having the same crystal structure. The radius of the contact area is calculated to be 0.018 mm.

Table 3.6.1 Parameters in this friction test

	Ball	Iron oxide single-crystalline wafers
Radius	2.38 mm	∞
Young's modulus	210 GPa	470 GPa
Poisson's ratio	0.3	0.25

3.6.2 Friction test results

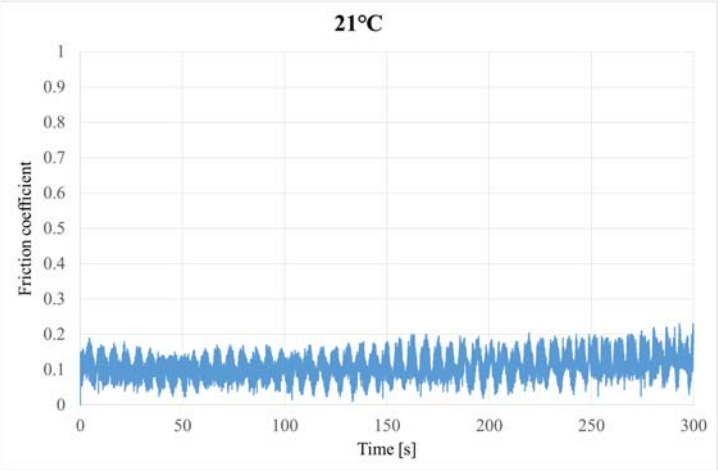

Figure 3.6.2 Friction coefficient-time graph measured using pure PAO at 20 degrees centigrade. The sliding trajectory was circular with a diameter of 1 mm, the load was 50 g, and the linear velocity was 1 mm/s. The periodic change was synchronized with the diameter of the circle.

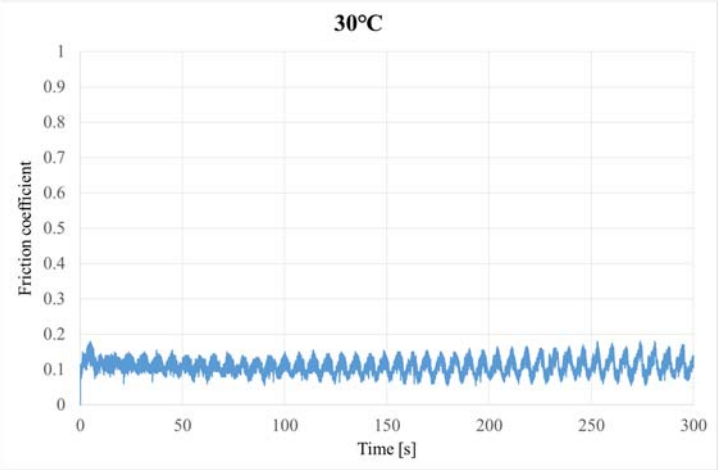

Figure 3.6.3 Friction coefficient-time graph measured using pure PAO at 30 degrees centigrade. The sliding trajectory was circular with a diameter of 1.1 mm, the load was 50 g, and the linear velocity was 1 mm/s. The periodic change was synchronized with the diameter of the circle.

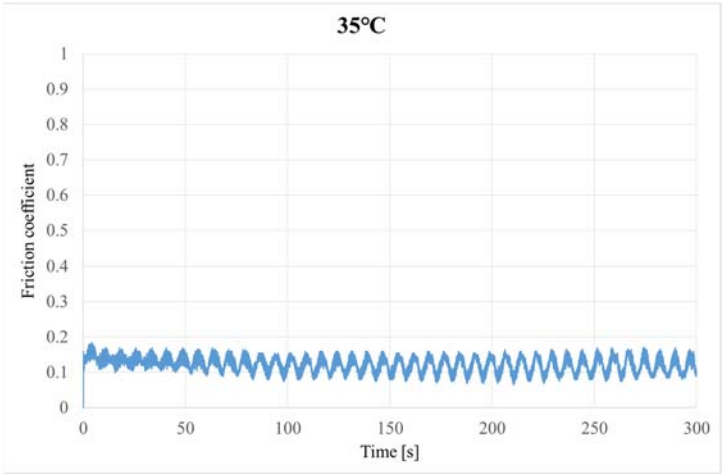

Figure 3.6.4 Friction coefficient-time graph measured using pure PAO at 35 degrees centigrade. The sliding trajectory was circular with a diameter of 1.2 mm, the load was 50 g, and the linear velocity was 1 mm/s. The periodic change was synchronized with the diameter of the circle.

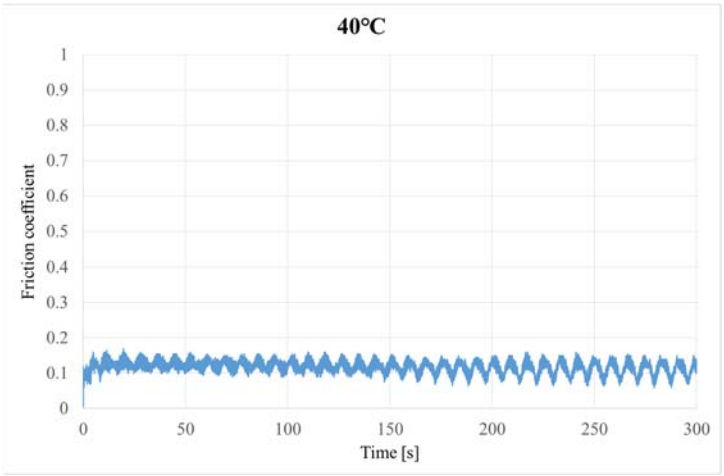

Figure 3.6.5 Friction coefficient-time graph measured using pure PAO at 40 degrees centigrade. The sliding trajectory was circular with a diameter of 1.3 mm, the load was 50 g, and the linear velocity was 1 mm/s. The periodic change was synchronized with the diameter of the circle.

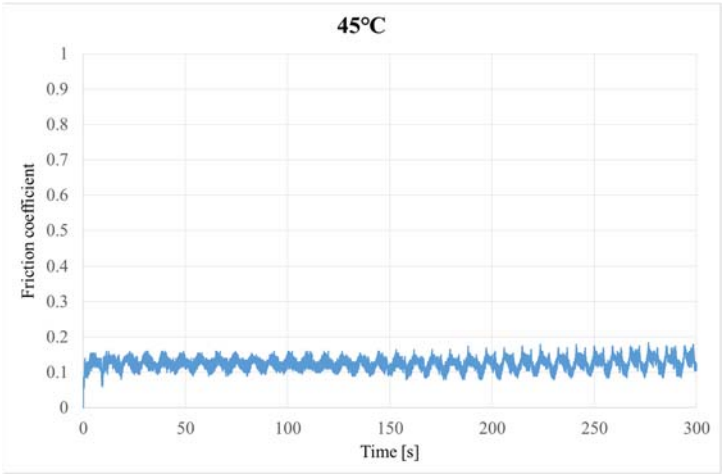

Figure 3.6.6 Friction coefficient-time graph measured using pure PAO at 45 degrees centigrade. The sliding trajectory was circular with a diameter of 1.4 mm, the load was 50 g, and the linear velocity was 1 mm/s. The periodic change was synchronized with the diameter of the circle.

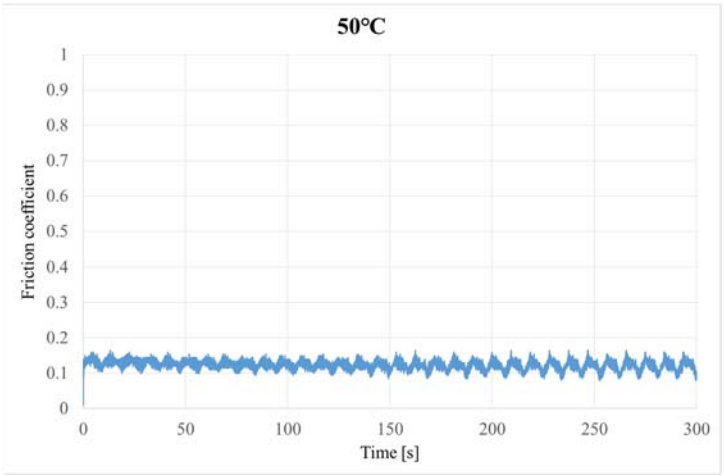

Figure 3.6.7 Friction coefficient-time graph measured using pure PAO at 50 degrees centigrade. The sliding trajectory was circular with a diameter of 1.5 mm, the load was 50 g, and the linear velocity was 1 mm/s. The periodic change was synchronized with the diameter of the circle.

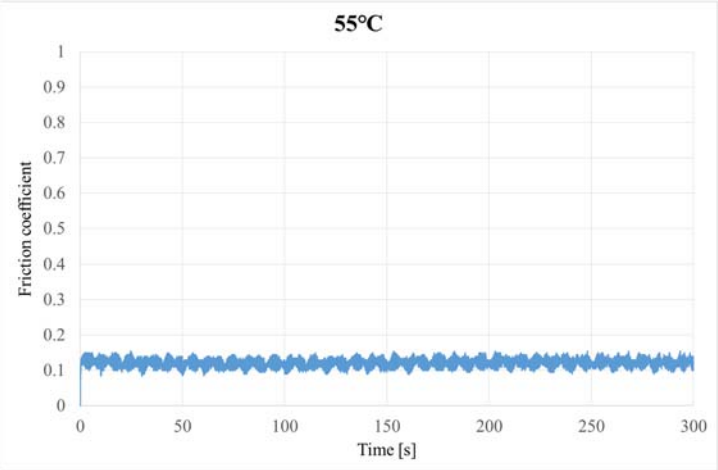

Figure 3.6.8 Friction coefficient-time graph measured using pure PAO at 55 degrees centigrade. The sliding trajectory was circular with a diameter of 1.6 mm, the load was 50 g, and the linear velocity was 1 mm/s. The periodic change was synchronized with the diameter of the circle.

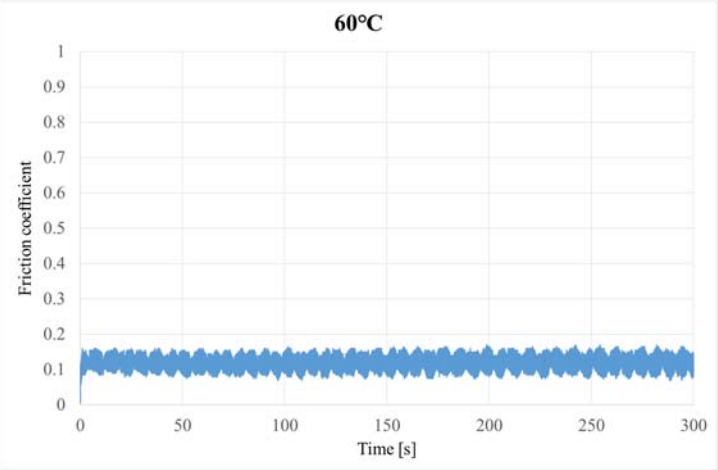

Figure 3.6.9 Friction coefficient-time graph measured using pure PAO at 60 degrees centigrade. The sliding trajectory was circular with a diameter of 1.7 mm, the load was 50 g, and the linear velocity was 1 mm/s. The periodic change was synchronized with the diameter of the circle.

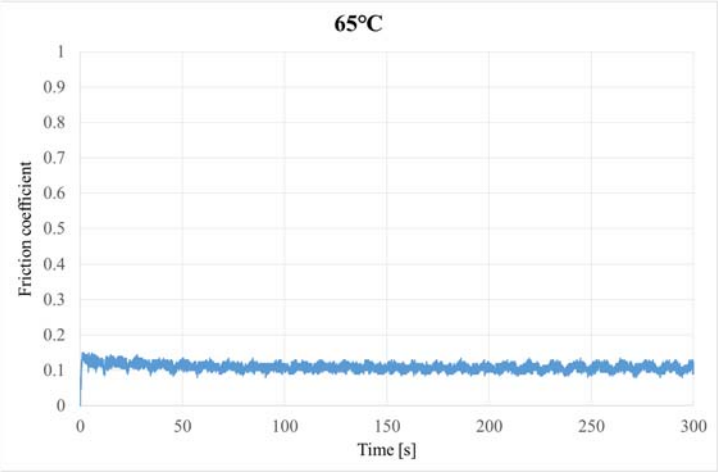

Figure 3.6.10 Friction coefficient-time graph measured using pure PAO at 65 degrees centigrade. The sliding trajectory was circular with a diameter of 1.8 mm, the load was 50 g, and the linear velocity was 1 mm/s. The periodic change was synchronized with the diameter of the circle.

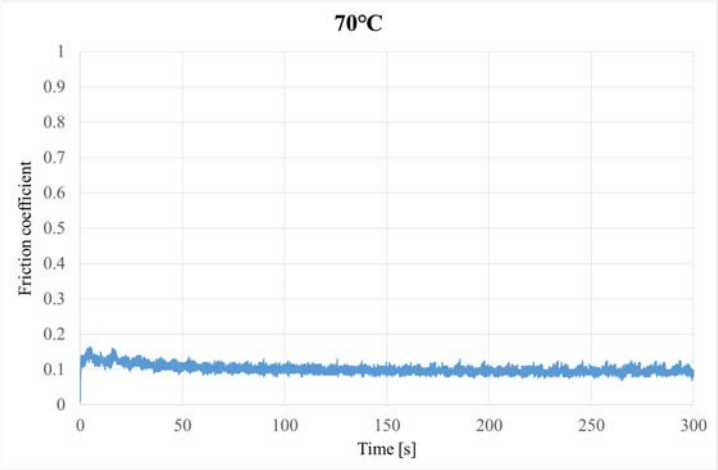

Figure 3.6.11 Friction coefficient-time graph measured using pure PAO at 70 degrees centigrade. The sliding trajectory was circular with a diameter of 1.9 mm, the load was 50 g, and the linear velocity was 1 mm/s. The periodic change was synchronized with the diameter of the circle.

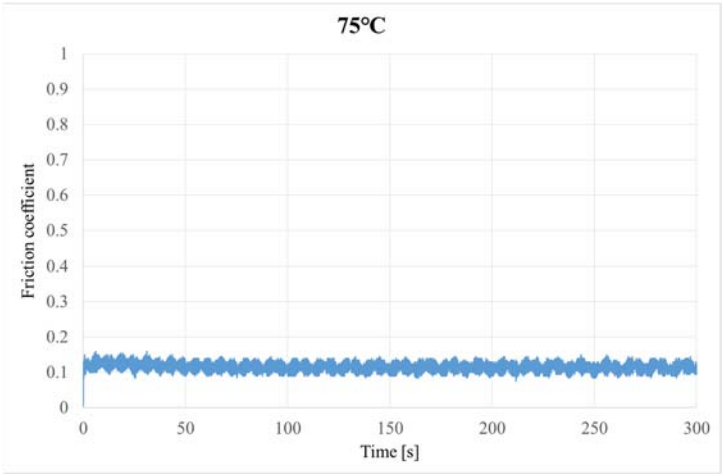

Figure 3.6.12 Friction coefficient-time graph measured using pure PAO at 75 degrees centigrade. The sliding trajectory was circular with a diameter of 2.0 mm, the load was 50 g, and the linear velocity was 1 mm/s. The periodic change was synchronized with the diameter of the circle.

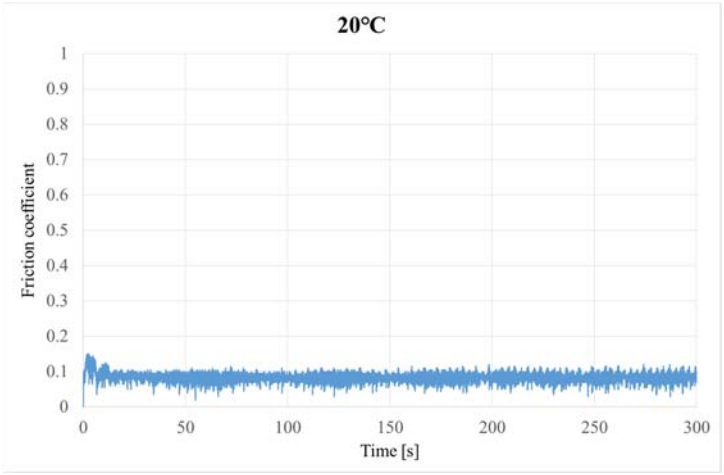

Figure 3.6.13 Friction coefficient-time graph measured using PAO containing oleic acid with a concentration of 1 mmol/kg at 20 degrees centigrade. The sliding trajectory was circular with a diameter of 1.0 mm, the load was 50 g, and the linear velocity was 1 mm/s. The periodic change was synchronized with the diameter of the circle.

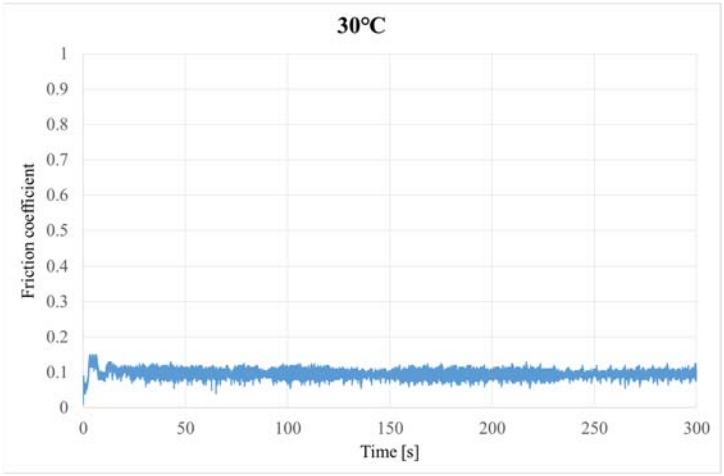

Figure 3.6.14 Friction coefficient-time graph measured using PAO containing oleic acid with a concentration of 1 mmol/kg at 20 degrees centigrade. The sliding trajectory was circular with a diameter of 1.1 mm, the load was 50 g, and the linear velocity was 1 mm/s. The periodic change was synchronized with the diameter of the circle**.**

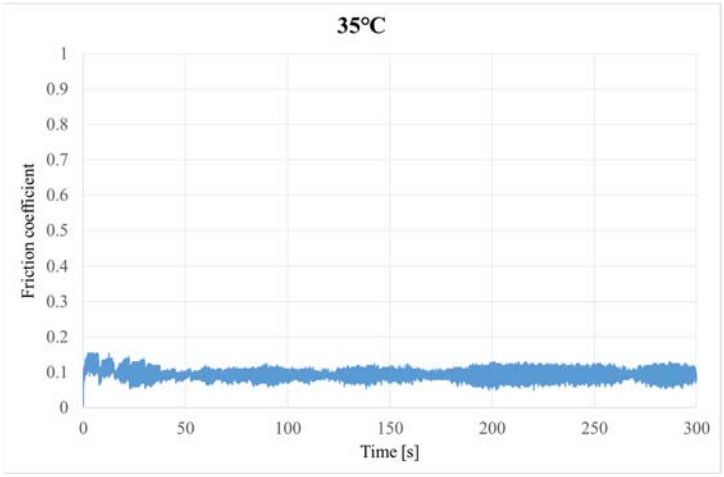

Figure 3.6.15 Friction coefficient-time graph measured using PAO containing oleic acid with a concentration of 1 mmol/kg at 35 degrees centigrade. The sliding trajectory was circular with a diameter of 1.2 mm, the load was 50 g, and the linear velocity was 1 mm/s. The periodic change was synchronized with the diameter of the circle.

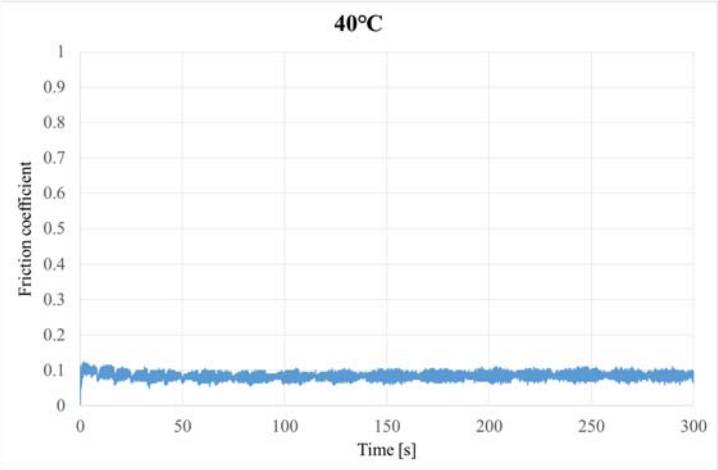

Figure 3.6.16 Friction coefficient-time graph measured using PAO containing oleic acid with a concentration of 1 mmol/kg at 40 degrees centigrade. The sliding trajectory was circular with a diameter of 1.3 mm, the load was 50 g, and the linear velocity was 1 mm/s. The periodic change was synchronized with the diameter of the circle.

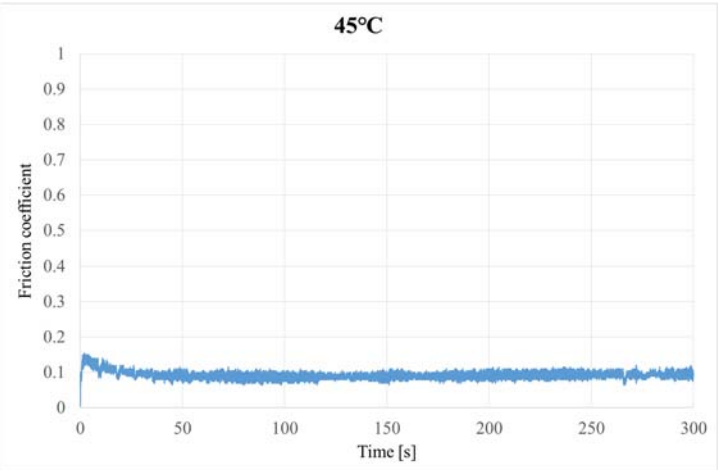

Figure 3.6.17 Friction coefficient-time graph measured using PAO containing oleic acid with a concentration of 1 mmol/kg at 45 degrees centigrade. The sliding trajectory was circular with a diameter of 1.4 mm, the load was 50 g, and the linear velocity was 1 mm/s. The periodic change was synchronized with the diameter of the circle.

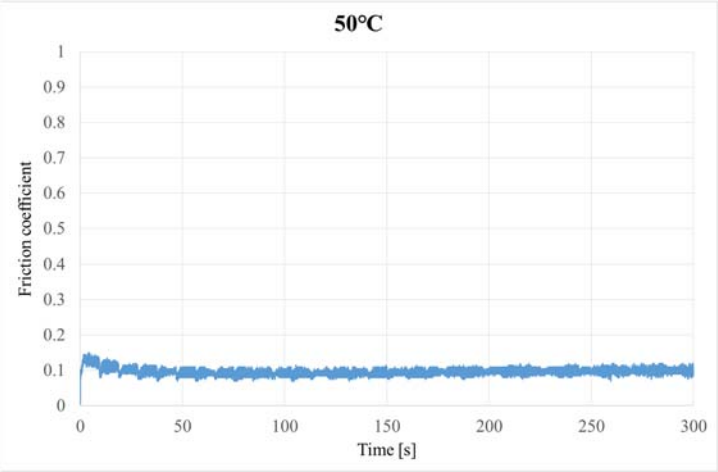

Figure 3.6.18 Friction coefficient-time graph measured using PAO containing oleic acid with a concentration of 1 mmol/kg at 50 degrees centigrade. The sliding trajectory was circular with a diameter of 1.5 mm, the load was 50 g, and the linear velocity was 1 mm/s. The periodic change was synchronized with the diameter of the circle.

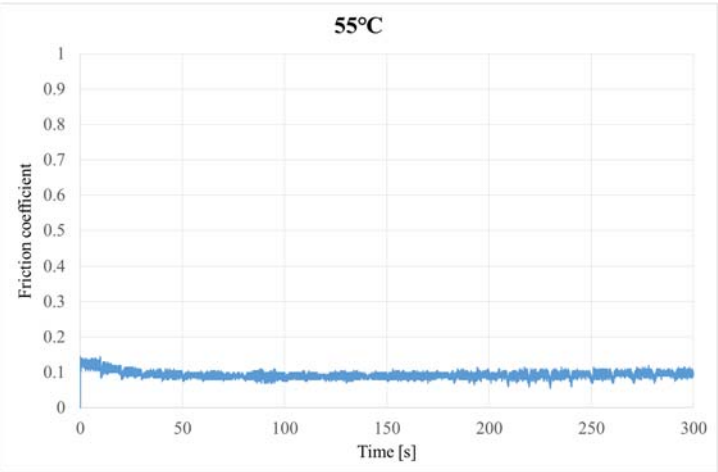

Figure 3.6.19 Friction coefficient-time graph measured using PAO containing oleic acid with a concentration of 1 mmol/kg at 55 degrees centigrade. The sliding trajectory was circular with a diameter of 1.6 mm, the load was 50 g, and the linear velocity was 1 mm/s. The periodic change was synchronized with the diameter of the circle.

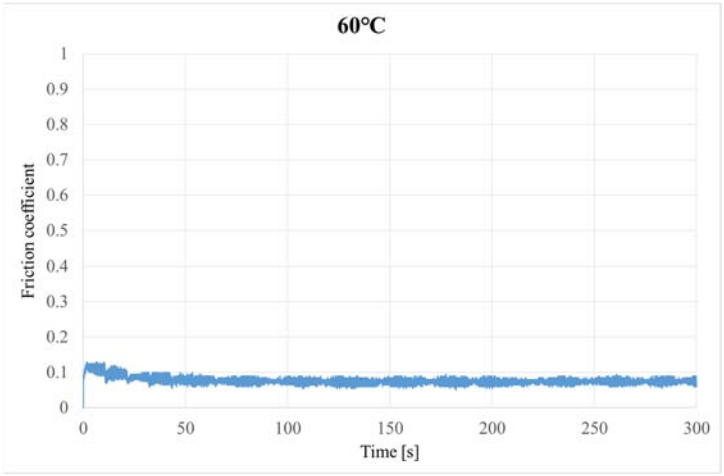

Figure 3.6.20 Friction coefficient-time graph measured using PAO containing oleic acid with a concentration of 1 mmol/kg at 60 degrees centigrade. The sliding trajectory was circular with a diameter of 1.7 mm, the load was 50 g, and the linear velocity was 1 mm/s. The periodic change was synchronized with the diameter of the circle.

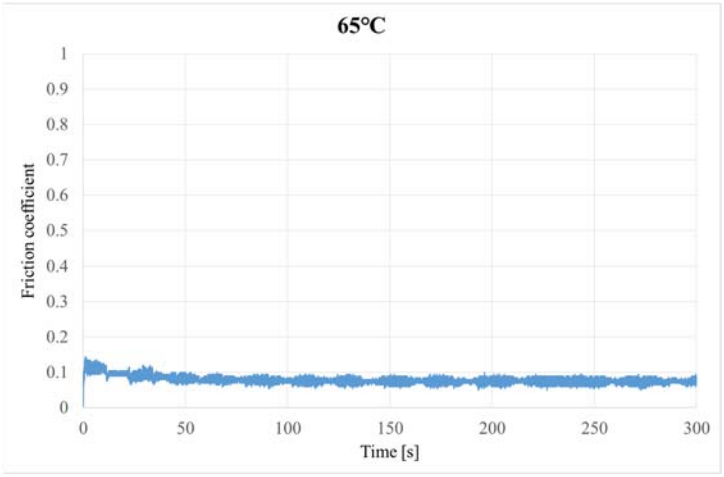

Figure 3.6.21 Friction coefficient-time graph measured using PAO containing oleic acid with a concentration of 1 mmol/kg at 65 degrees centigrade. The sliding trajectory was circular with a diameter of 1.8 mm, the load was 50 g, and the linear velocity was 1 mm/s. The periodic change was synchronized with the diameter of the circle.

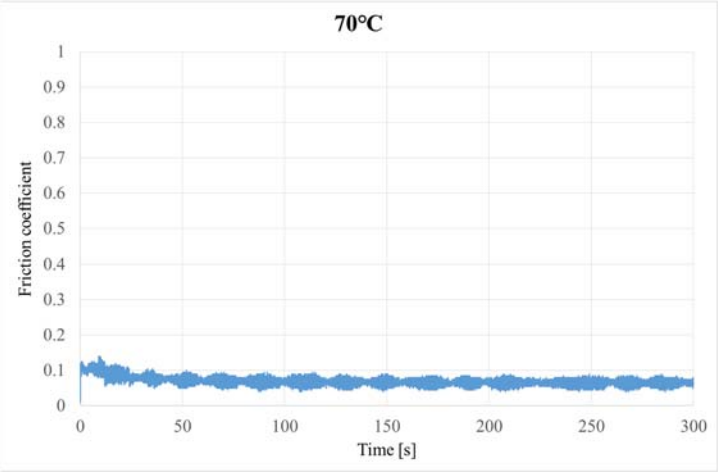

Figure 3.6.22 Friction coefficient-time graph measured using PAO containing oleic acid with a concentration of 1 mmol/kg at 70 degrees centigrade. The sliding trajectory was circular with a diameter of 1.9 mm, the load was 50 g, and the linear velocity was 1 mm/s. The periodic change was synchronized with the diameter of the circle.

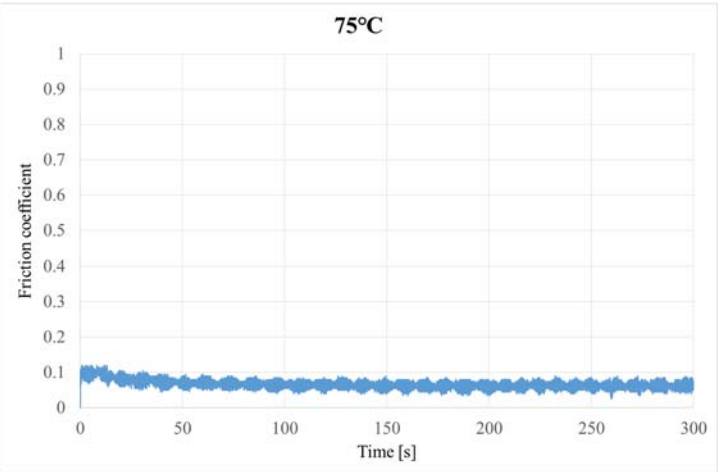

Figure 3.6.23 Friction coefficient-time graph measured using PAO containing oleic acid with a concentration of 1 mmol/kg at 75 degrees centigrade. The sliding trajectory was circular with a diameter of 2.1 mm, the load was 50 g, and the linear velocity was 1 mm/s. The periodic change was synchronized with the diameter of the circle.

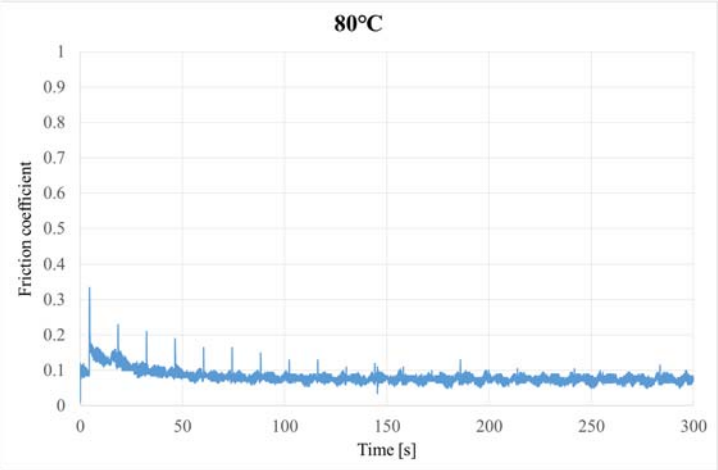

Figure 3.6.24 Friction coefficient-time graph measured using PAO containing oleic acid with a concentration of 1 mmol/kg at 80 degrees centigrade. The sliding trajectory was circular with a diameter of 2.2 mm, the load was 50 g, and the linear velocity was 1 mm/s. The periodic change was synchronized with the diameter of the circle.

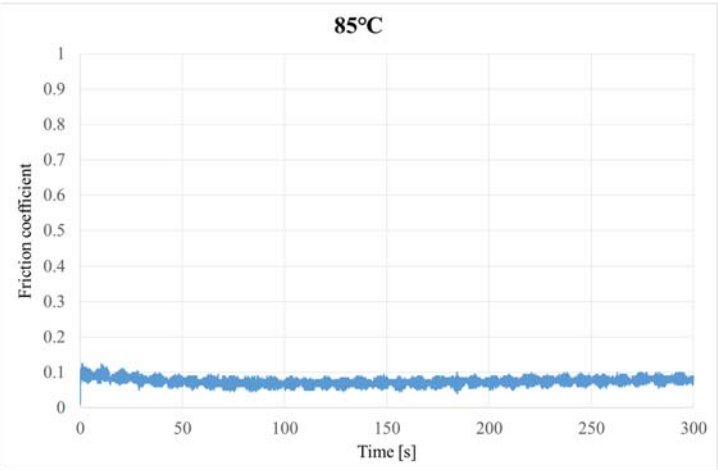

Figure 3.6.25 Friction coefficient-time graph measured using PAO containing oleic acid with a concentration of 1 mmol/kg at 85 degrees centigrade. The sliding trajectory was circular with a diameter of 2.3 mm, the load was 50 g, and the linear velocity was 1 mm/s. The periodic change was synchronized with the diameter of the circle.

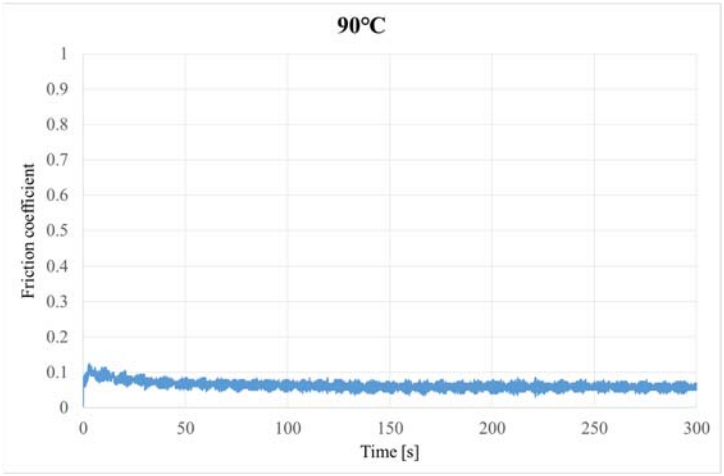

Figure 3.6.26 Friction coefficient-time graph measured using PAO containing oleic acid with a concentration of 1 mmol/kg at 90 degrees centigrade. The sliding trajectory was circular with a diameter of 2.5 mm, the load was 50 g, and the linear velocity was 1 mm/s. The periodic change was synchronized with the diameter of the circle.

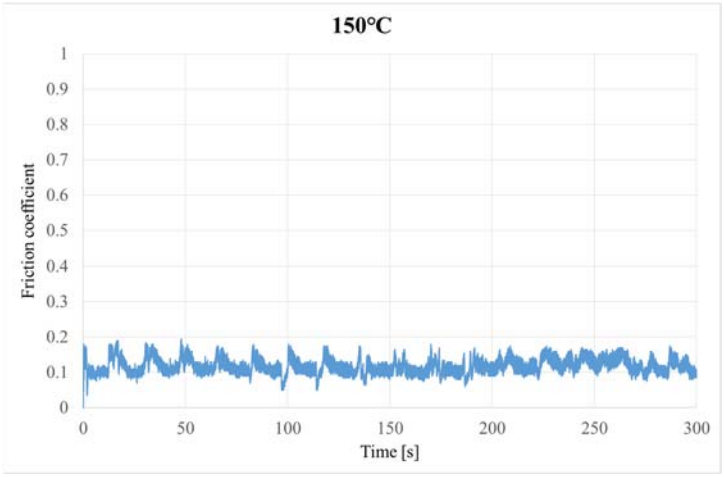

Figure 3.6.27 Friction coefficient-time graph measured using PAO containing oleic acid with a concentration of 1 mmol/kg at 150 degrees centigrade. The sliding trajectory was circular with a diameter of 2.6 mm, the load was 50 g, and the linear velocity was 1 mm/s. The periodic change was synchronized with the diameter of the circle.

Chapter 4 Kelvin probe force mapping in lubricants

4.1 Introduction

In Chapters 2 and 3, the presence or absence of the modifier adsorption layer on the iron oxide was probed using FM-AFM, and the vertical as well as lateral distribution of the layers is visualized in molecular scale resolution by mapping layer-induced force on the probing tip. By discussing these results together with the dynamic friction coefficient measured by friction tests, the usefulness of visualizing the behavior of modifier molecules at the lubricant-metal interface was shown. In these experiments, only one kind of modifier was added. However, actual lubricants include a plurality of kinds of modifiers. In addition to topographic and mechanical response, measurement of surface potential distribution can help in identifying modifiers. In this chapter, we propose KPFM measurement in lubricants as a new method for quantifying modifier molecules. Due to the polarity of modifier molecules, heterogeneous adsorption of modifier molecules on iron oxide should be detected as a difference in surface potential. The amount of charge can be calculated from the potential difference, and the amount of modifier molecules can be estimated from the amount of charge.

Poly-α-olefin containing oleic acid was used for the experiment discussed in this chapter. Poly-α-olefin is a commercially representative hydrocarbon lubricant, and oleic acid is a modifier frequently used in practical lubricants.

4.2 Method

As described in Section 1.2.1, AFM is a microscope that images the interaction force between the probe tip and the sample surface. A small probe having a diameter of several tens nm or less is formed at the edge of the cantilever. During the measurement, the cantilever is mechanically oscillated, and the frequency and amplitude of the oscillation are changed by the interaction force between the probe tip and the sample. The change is detected by the laser beam irradiated on the back of the cantilever. In the measurement of the topography, the scanning is conducted while keeping the atomic force between the probe tip and the sample constant so that the cantilever oscillation does not change during the measurement. It means that the scanning is conducted while keeping the distance between the probe tip and the sample surface constant. As a result, the scanned trajectory is regarded as the topography of the sample surface.

KPFM is an analytical method applying Kelvin Probe Force method to AFM[1], and can measure the potential distribution on the sample surface in addition to topography. Figure 4.2.1 shows a schematic diagram of the KPFM, and Figure 4.2.2 shows a brock diagram of the KPFM. In KPFM, an AC voltage is applied to the conductive cantilever. When the potential of the probe is different from that of the sample surface, an electrostatic attractive force acts between the probe and the sample surface. In KPFM, the distance between the probe and the sample surface is feedback regulated to keep constant by the topography measurement mechanism. Therefore, it can be considered that the electrostatic attractive force is changed only depending on the potential difference between the probe and the sample surface. When an AC voltage is applied to the cantilever, a potential difference is generated between the cantilever and the sample surface, and an electrostatic attractive force acts between them, and the

cantilever is oscillated at a frequency synchronized with the frequency of the AC voltage. When a DC voltage is applied to the cantilever so that the potential of the cantilever is equal to that of the sample surface, the cantilever oscillation amplitude synchronized with the frequency of the AC voltage is minimized. The potential distribution on the sample surface can be measured by scanning the cantilever while applying DC voltage to the cantilever so that the oscillation amplitude of the cantilever is minimum at each position. The change of the cantilever oscillation by the atomic force and by the electrostatic attractive force can be separated with the lock-in amplifier. When KPFM is applied to the AM-AFM, the spatial resolution of the potential is several tens nm in the XY direction. On the other hand, when KPFM is applied to the FM-AFM, the spatial resolution of the potential is higher than that of AM-AFM, and is several nm in the XY direction.

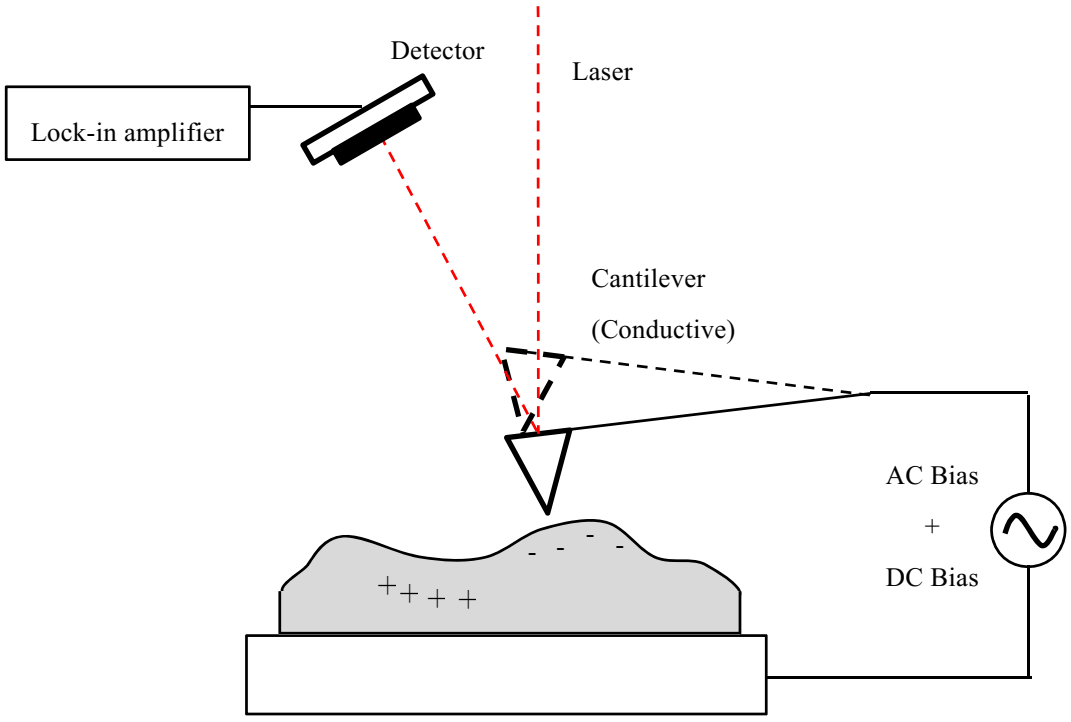

Figure 4.2.1 A schematic diagram of KPFM.

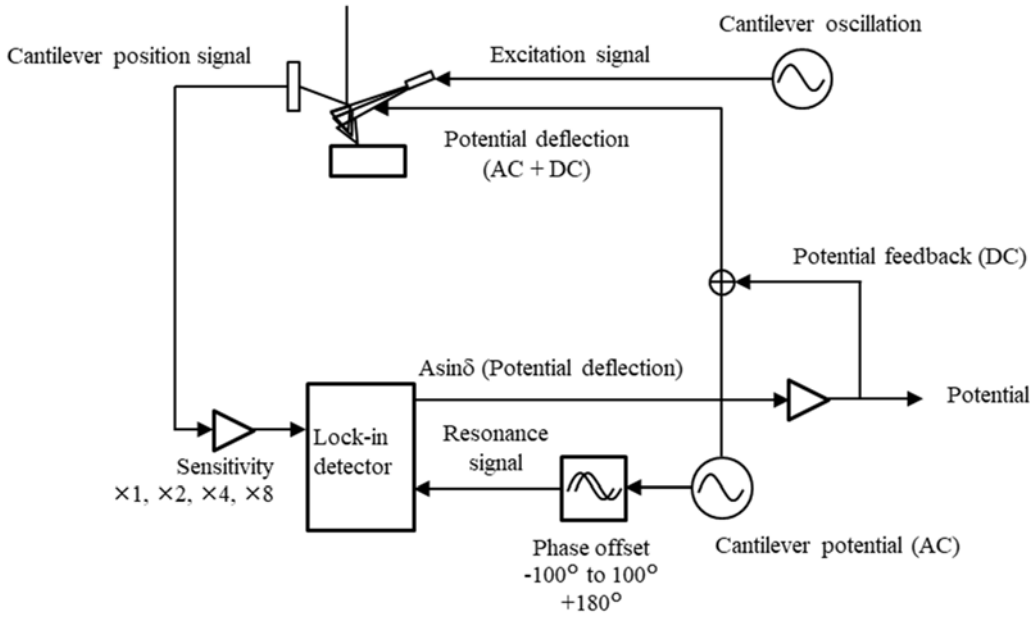

Figure 4.2.2 A brock diagram of the KPFM. In addition to a feedback circuit for measuring topography, there is a feedback circuit for measuring the surface potential distribution of the sample. An AC voltage and a DC voltage are applied to the cantilever, and a change in the cantilever oscillation caused by the applied voltage is extracted with the lock-in amplifier.

KPFM is a method already established in ultrahigh vacuum[2-7] and gas.[8] On the other hand, in liquid, it is both experimentally and theoretically discussed by Ken-ichi Umeda et al. that it is difficult to work KPFM well when liquid molecules are ionized[9]. However, there is reported case that work function changes of Au were measured by KPFM in the nonpolar liquid decane, by Anna L. Domanski et al.[10] And fortunately, since poly-α-olefin (PAO) used as a base oil was also a nonpolar organic solvent, KPFM could be available for the analysis of the modifiers in lubricating oil. Therefore, in this section, it was confirmed that KPFM worked well in the lubricant and was able to detect the potential difference caused by sliding.

KPFM was enabled with SPM-8100FM and the control unit of SPM-9700HT (Shimadzu). In FM-KPFM, for the topographic and the potential distribution imaging of the iron oxide single-crystalline wafers, the resonance oscillation of a doped silicon cantilever (Nanoworld, PPP-NCHR) was mechanically excited with a piezo-actuator. The nominal spring constant and the resonant frequency of the cantilevers was 42 N/m and 100–140 kHz, respectively. In AM-KPFM, the doped silicon cantilever coated with PtIr (Nanoworld, EFM) was mechanically oscillated at the operating frequency with a piezo-actuator. The nominal spring constant and the resonant frequency of the cantilevers was 2.8 N/m and 70 kHz, respectively.

Based on the cantilever holder for the observation in liquid with SPM-8100 FM and SPM-9700 HT, the cantilever holder was improved to be able to operate KPFM in liquid. The iron oxide single-crystalline wafer was fixed in a Cu petri dish placed on the microscope stage driven by a piezoelectric scanner. The dish was filled with the lubricant of 500 μl and then the cantilever assembly was put on top. The reason why Cu petri dish was used was in order to keep electrical conductivity. Imaging scans were conducted at RT.

4.3 Operation confirmation of KPFM measurement

4.3.1 In hexadecane

Figure 4.3.1 shows the step potential image measured as an operation confirmation in hexadecane using FM-KPFM. The step potential was made by applying sample bias voltage at 1V increments. The red color represents higher potential and the blue color represents lower potential. The potential profile line on the white line is shown below the potential image and the potential difference between steps was measured at three points. The step potential of 1 V was measured stably. This result presented that KPFM operated normally in nonpolar organic solvent hexadecane.

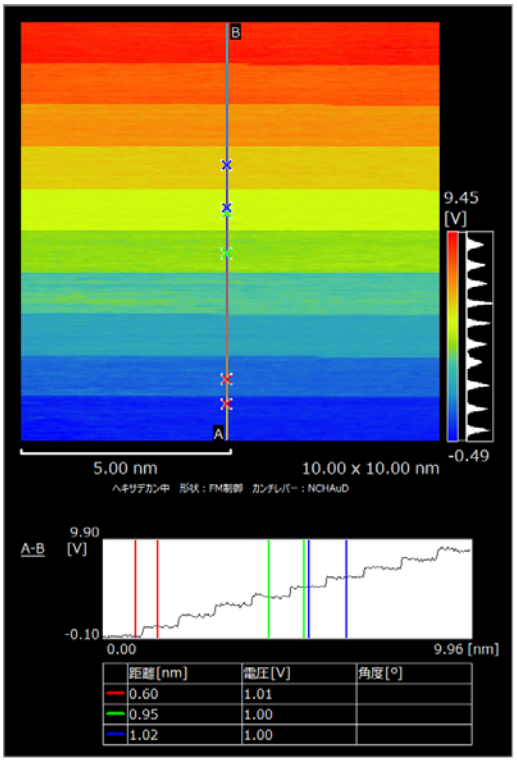

Figure 4.3.1 The potential image of the metal surface with a sample bias voltage applied in 1V increments. The potential profile line on the white line is shown below the potential image, and the potential difference between steps was measured at three points.

4.3.2 In lubricants

Figure 4.3.2 shows the step potential images measured as an operation confirmation Figure 4.3.1 shows the step potential image measured as an operation confirmation in hexadecane using FM-KPFM. The left image was measured in PAO and the right image was measured in PAO containing oleic acid with a concentration of 1mmol/kg. The step potential was made by applying sample bias voltage at 1V increments. The red color represents higher potential and the blue color represents lower potential. The potential profile lines on the white line are shown below the potential image. In both cases, the step potential of 1 V was measured stably. These results represented that KPFM operated normally in PAO and PAO containing oleic acid with a concentration of 1mmol/kg.

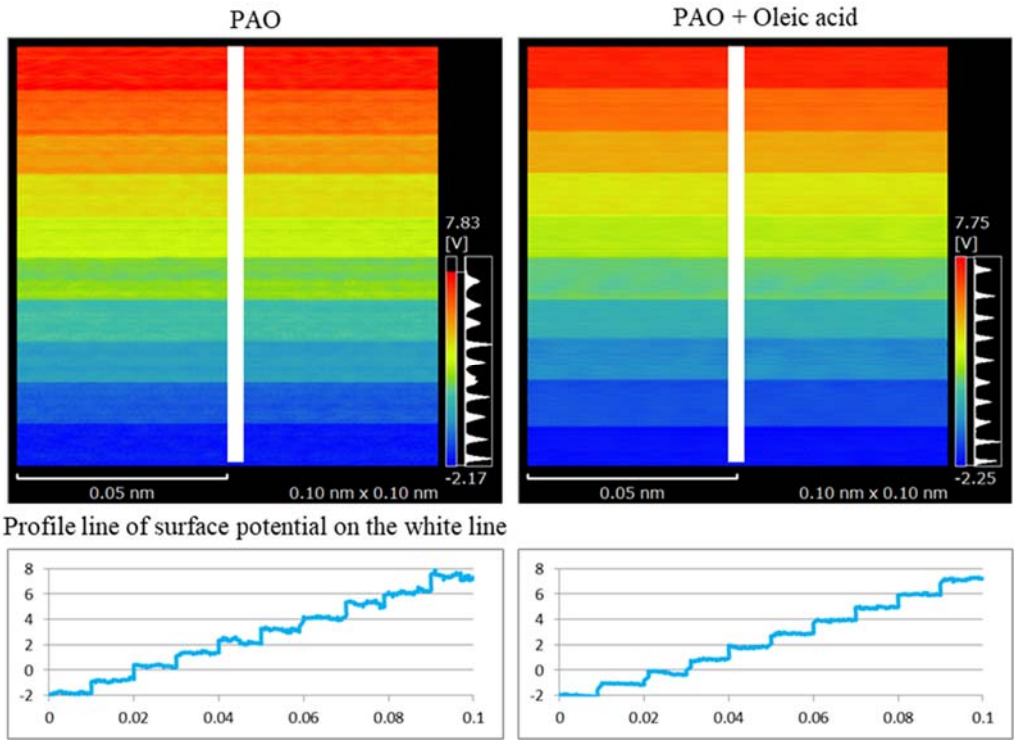

Figure 4.3.2 The potential image of the metal surface with a sample bias voltage applied in 1V increments. The potential profile line on the white line is shown below the potential image.

4.4 Surface potential distribution of sliding part and non-sliding part

The probe was slid in the region of 500 nm × 500 nm on the surface of the iron oxide single-crystalline wafer in the lubricants to create a pseudo-boundary lubrication, using Contact Mode of SPM in which the probe traces the sample surface with a constant force. The sliding part was fabricated by scanning the AFM probe ten times in the same area with a contact force of about 0.4 μN for about 43 minutes. Then the scanning mode of SPM was changed to KPFM Mode from Contact Mode, the surface potential distribution of this sliding part and non-sliding part was measured in about 43 minutes. AM-KPFM easier to control than FM-KPFM was used, because this analysis did not require atomic resolution in XY direction.

The results are shown in Figure 4.4.1. The left image was the potential distribution image of the wafer surface measured after making the sliding part in PAO and the right image was the potential distribution image of the wafer measured after making the sliding part in PAO containing oleic acid with a concentration of 1mmol/kg. The scanning range was 2 μm × 2 μm. The area of 500 nm × 500 nm surrounded by the black broken line located in the center of the potential image is the pre-created sliding part by the AFM probe. The red color represents higher potential and the blue color represents lower potential.

In either case, there was no significant change in the surface topography before and after sliding, but in the potential, the change that the potential of sliding part was higher than that of the non-sliding part was seen. From the non-uniform distribution of the surface potential due to sliding in lubricating oil, it was succeeded to detect the change in the surface of the iron oxide single-crystalline wafer, which could not be detected by topography.

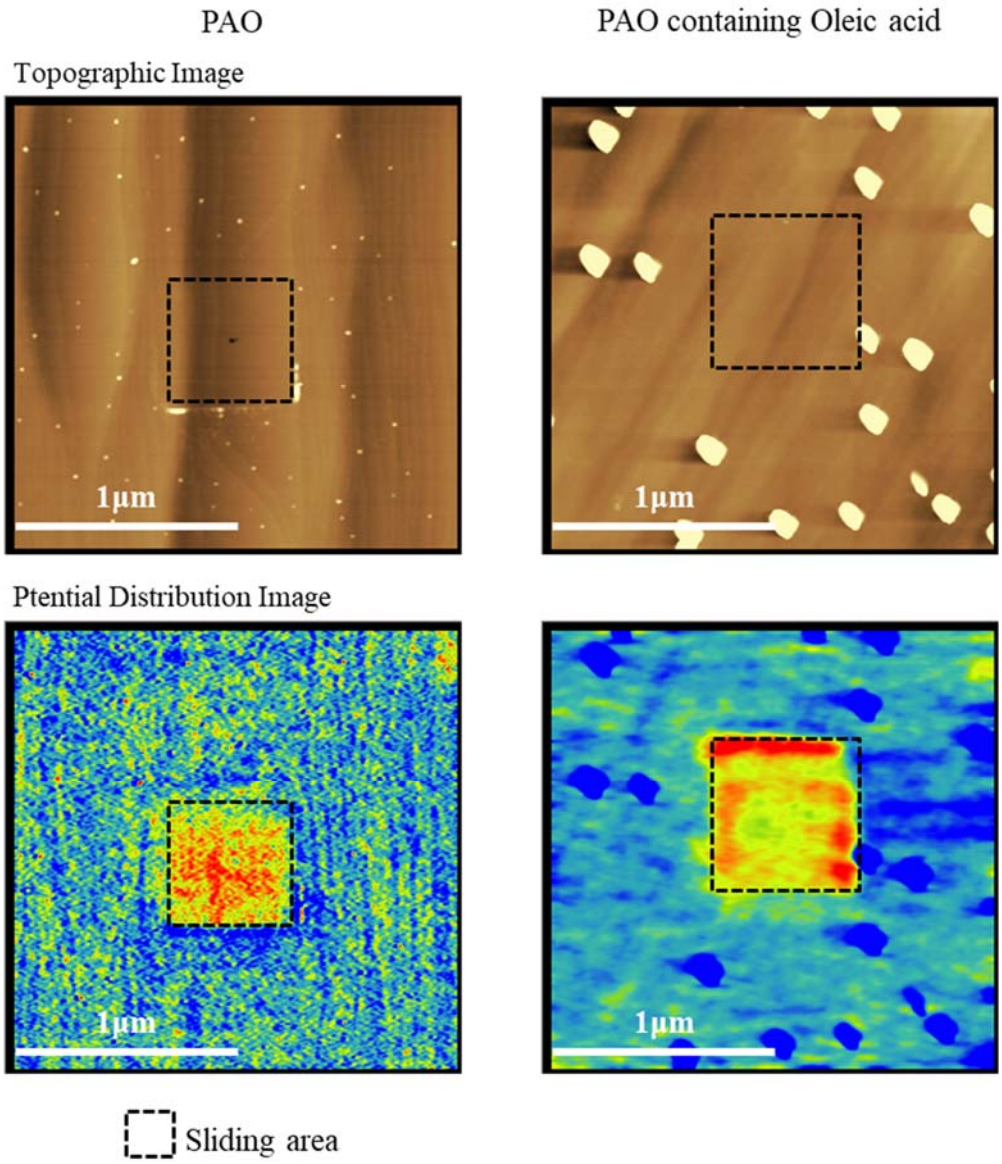

Figure 4.4.1 The surface potential distribution image of the iron oxide single-crystalline wafer measured after making the sliding part (a) in PAO and (b) in PAO containing oleic acid with a concentration of 1mmol/kg. In either case, the potential was higher in the sliding part than in the non-sliding part.

4.5 Conclusion

In this chapter, it was confirmed for the first time that KPFM works normally in PAO and PAO containing oleic acid. Besides, boundary lubrication was simulated with an AFM probe, and it was detected that the surface potential was different between the sliding part and the non-sliding part. This indicates that the sliding in the lubricating oil changes the charged state of the iron oxide single-crystalline wafer.

Although the objective of this experiment was to identify the type of modifier and its amount of adsorption from the surface potential difference by using the polar nature of the modifier, in this study, the experiment is completed when it is confirmed that the surface potential is different between the sliding part and the non-sliding part. Further experiments are needed to use KPFM for quantitative evaluation of modifier sorption layers.

4.6 Reference

(1) Nonnenmacher, M.; O'Boyle, M. P.; Wickramasinghe, H. K. Kelvin probe force microscopy. *Appl. Phys. Lett.* 1991, *58* (*25*), 2921

(2) Kitamura, S.; Suzuki, K.; Iwatsuki, M.; Mooney, C. B. Atomic-scale variations in contact potential difference on Au/Si(111) 7×7 surface in ultrahigh vacuum. *Appl. Surf. Sci.* 2000, *157*, 222

(3) Okamoto, K.; Yoshimoto, K.; Sugawara, Y.; Morita, S. KPFM imaging of Si(1 1 1)53×53-Sb surface for atom distinction using NC-AFM. *Appl. Surf. Sci.* 2003, *210*, 128

(4) Shiota, T.; Nakayama, K. Atom-Resolved Imaging of the Potential Distribution at Si (111) 7×7 Surfaces. *Jpn. J. Appl. Phys* 2002, *41*, L1178

(5) Eguchi, T.; Fujikawa, Y.; Akiyama, K.; An, T.; Ono, M.; Hashimoto, T.; Morikawa, Y.; Terakura, K.; Sakurai, T.; Lagally, M. G.; Hasegawa, Y. Imaging of all Dangling Bonds and their Potential on the Ge/Si(105) Surface by Noncontact Atomic Force Microscopy. *Phys. Rev. Lett.* 2004, *93*, 266102

(6) Sasahara, A; Kitamura, S.; Uetsuka, H.; Onishi, H. Oxygen-Atom Vacancies Imaged by a Noncontact Atomic Force Microscope Operated in an Atmospheric Pressure of N2 Gas. *J.Phys.Chem,.* 2004, *B 108*, 15735

(7) Onishi, H.; Fukui, K.; Iwasawa, Y. Atomic-Scale Surface Structures of TiO2(110) Determined by Scanning Tunneling Microscopy: A New Surface-Limited Phase of Titanium Oxide. *Bull. Chem. Soc. Jpn*. 1995, *68*, 2447

(8) Kokawa, R.; Ohta, M.; Sasahara, A.; Onishi, H. Kelvin Probe Force Microscopy Study of a Pt/TiO_2 Catalyst Model Placed in an Atmospheric Pressure of N_2 Enviroment. *Chemistry - An Asian Jounal*, 2012, *7*, 1251

(9) Umeda, K.; Kobayashi, K.; Oyabu, N.; Hirata, Y.; Matsushige, K.; Yamada, H. Practical aspects of Kelvin-probe force microscopy at solid/liquid interfaces in various liquid media. *J.Appl.Phys*., 2014, *116*, 134307

(10) Domanski, A. L.; Sengupta, E.; Bley, K.; Untch, M. B.; Weber, S. K. L.; Landfester, K.; Weiss, C. K.; Butt, H-J.; Berger, R.; Kelvin Probe Force Microscopy in Nonpolar Liquids. *Langmuir*, 2012, *28*, 13892-13899

Chapter 5 General conclusion

The prevention of wear and seizure and the reduction of friction in boundary lubrication where the distance between two sliding surfaces is close and contact between solids is partially generated are still major problems. One of the solutions is a modifier contained in lubricating oil. By modifying the solid surface or adsorbing to the solid surface, the modifier reduces friction and prevents wear and seizure. Especially, in the boundary lubrication in which the single molecule adsorption film influences the friction reduction characteristic, the adsorption of the modifier to the solid surface directly leads to the performance improvement of the lubricating oil. That is, knowing and controlling the modifier adsorption film is the key to controlling boundary lubrication.

On the other hand, even today, it is not easy to characterize adsorbed modifiers of nanometer-scale thickness. The mass and chemical structure of the adsorbed modifier and the thickness of the adsorption film have been evaluated in the previous study. However, these analyses are based on the assumption that the modifier is uniformly adsorbed. It is expected that the adsorption is not uniform in the actual sliding part, and an operand method capable of evaluating the non-uniformity is required. The FM-AFM has a spatial resolution in the order of sub nanometers, which is on the atomic and molecular size, in both the in-plane and vertical directions, and can detect unevenness at the molecular level of the adsorption film. In addition, it has a force detection sensitivity of the order of 10 pN, and can capture not only a solid modifier adsorption film but also a modifier adsorption layer existing in a liquid state at a solid-liquid interface. In this study, we tried to visualize the adsorption film of the modifier using FM-AFM, and succeeded.

In Chapter 2, the adsorption of C18AP on the iron oxide film was evaluated, which is commonly used as an antifriction agent. As the base oil, PAO was used, which is

also widely used. The antifriction agent forms a tribofilm of the reaction secondary product on the solid surface to prevent seizure and wear. The formed reaction coating is hard enough to be recognized as a solid and can be analyzed with a conventional AFM/SPM. However, the precursor adsorption film formed by the physical or chemical adsorption of modifier molecules on the solid surface as a preliminary step for this reaction was so soft and required the force sensitivity of the order of 10 pN achieved in FM-AFM to detect the layer induced force response. The adsorption layer of C18AP contained in PAO, the base oil, to the oxidized iron film was evaluated. The formation state of the C18AP adsorption layer was evaluated by changing the concentration of C18AP. According to the dynamic response measurement of the ZX cross section, C18AP was adsorbed with its phosphoric acid end anchored to the films. There was fluctuation of the $C_{18}H_{35}$ chains of C18AP in the lubricant. The force maps reflected the time-averaged density distribution of the fluctuating chains and monotonically decayed to zero force at a tip-to-surface distance of 2 nm when a monomolecular layer of C18AP was completed. The oxidized iron film was intermittently covered with C18AP molecules in the lubricants containing C18AP concentrations of 0.2 and 2 ppm; it completely covered at 20 and 200 ppm. The oxidized iron film that was completely covered with the C18AP layer produced topographic images with reduced sharpness according to its fluctuating, dynamic boundary with the lubricant. And in addition to analysis with FM-AFM, the dynamic friction coefficient of the sliding steel-lubricant-steel interfaces was evaluated using the friction tester. As the results, the dynamic friction coefficient decreased with increasing the coverage of the monomolecular C18AP on the iron film. These experimental results indicate that nanometer-scale distribution of C18AP precursor adsorption film on the oxidized iron film is related with the friction characteristics of

sliding surfaces, and it proved that the nanometer-scale analysis is valuable for the control of the modifier adsorption layer at the lubricating interface.

In Chapter 3, the adsorption films of carboxylic acids were evaluated such as stearic acid and oleic acid, commonly used as oiliness agents, onto iron oxide single-crystalline wafers. As the base oil, PAO was used, which is also widely used. The adsorption film formed by the oiliness agent is also expected to be soft enough not to be recognized as a solid, as is the case with the precursor adsorption film formed by the extreme-pressure agent and the antifriction agent, and the detection required the force sensitivity of the order of 10 pN achieved in FM-AFM. As in Chapter 2, topography and dynamic response measurements of the ZX cross section were used to evaluate. In the topographic measurement, it was found that adsorption of the carboxylic acid onto the wafer is enhanced by pseudo sliding caused from the interaction force generated when the probe was scanned on the surface of the wafer. In frequency-shift mapping on ZX plane, by comparing the analytical results of five carboxylic acids with different molecular structures, their adsorption on the wafer was elucidated on a molecular scale. The carboxylic acid was chemically adsorbed with its polar group to the wafer and inhibited the direct contact of PAO with the wafer by forming a monolayer on the surface of the wafer. In case of single chain carboxylic acid, the carboxylic acid in the lubricant formed the liquid layered structure on the monolayer with a layer-to-layer distance of 0.56 - 0.75 nm. This is the first time that the behavior of carboxylic acids at the solid-liquid interface has been identified in the order of molecular scale.

In addition, the temperature dependence of the oleic acid adsorption onto the iron oxide single-crystalline wafer was verified by measuring the frequency-shift maps at temperatures from 25 degrees centigrade to 65 degrees centigrade. The repulsive force

from the fluctuating tail of the oleic acid adsorbed to the wafer, became thinner with increasing temperature, and disappeared at 60 degrees centigrade. On the other hand, the dynamic friction coefficient of the sliding SUJ2–lubricant–iron oxide single-crystalline wafer interfaces, which was determined using the ball on disk friction tester at each temperature from 25 degrees centigrade to 150 degrees centigrade, increased at 150 degrees centigrade compared with it from 25 degrees centigrade to 90 degrees centigrade. These results indicated that the adsorption of oleic acid to the wafer is activated at a temperature much lower than the temperature at which the effect is lost. The mechanical probing with FM-AFM provides a new knowledge in a molecular scale that cannot be found only from friction phenomena in the macroscopic dimensions.

In Chapter 4, it was confirmed for the first time that KPFM works normally in PAO-based lubricant. In addition, it was detected that the surface potential of the sliding part simulated with the AFM probe was different from that of the non-sliding part. This indicates that sliding in a lubricating oil using a nonpolar organic solvent as a base oil changes the charged state of the iron oxide shingle-crystalline wafer surface. In the present experiment, PAO containing only oleic acid was used, but several kinds of modifiers are added to the actual lubricants to improve the performance, which makes the behavior of the modifier more complicated. It is very useful in designing a modifier formulation to know which modifier preferentially forms an adsorption film and provides a good effect, when multiple modifiers are mixed. The KPFM proposed as a new analytical method adds an index of electrical characteristics in addition to topographic and mechanical response. This can be of great help in identifying the type of modifier and the amount adsorbed.

In this study, the behavior of the modifier molecule in the lubricant at the solid-liquid interface was identified at the molecular resolution by the excellent spatial resolution and force sensitivity of FM-AFM. Not only an adsorption film hard enough to be recognized as a solid, but also an adsorption film existing as a liquid was captured. The relationship between the adsorption film and the macroscopic frictional properties was confirmed, and it was clarified that the behavior of the modifier at the molecular level affected the macroscopic frictional properties in no small way. FM-AFM and KPFM can be expected as new methods to accelerate the development of lubricants by clarifying the behavior of lubricants at friction interfaces on a molecular scale and providing a theoretical basis for lubricant design.

List of research achievements

Presentations

1. KOKAWA Ryohei, MORIGUCHI Shiho, TSUJIMOTO Teppei, SASAHARA Akira, ONISHI Hiroshi: FM-AFM Imaging of Adsorbate Generated by Oiliness Agent. Tribology Conference 2018 Spring in Tokyo, Oral presentation
2. MORIGUCHI Shiho, KOKAWA Ryohei, TSUJIMOTO Teppei, SASAHARA Akira, ONISHI Hiroshi: Lubricants Containing Oiliness Agent - FM-AFM Imaging on a Model Substrate for Steal. MAINZ Summer School Solid Liquid Interfaces 2018, Poster presentation
3. MORIGUCHI Shiho, KOKAWA Ryohei, TSUJIMOTO Teppei, SASAHARA Akira, ONISHI Hiroshi: Observation of Interface between Lubricant and Fe Substrate by FM-AFM. International conference on Non-Contact Atomic Force Microscopy 2018 (NCAFM 2018), Poster presentation
4. MORIGUCHI Shiho, KOKAWA Ryohei, FUJINO Keita, TSUJIMOTO Teppei, SASAHARA Akira, ONISHI Hiroshi: FM-AFM Imaging of Additives on Iron Interfaces Tribology Conference 2018 Autumn in Ise, Oral presentation
5. MORIGUCHI Shiho, KOKAWA Ryohei, FUJINO Keita, TSUJIMOTO Teppei, SASAHARA Akira, ONISHI Hiroshi: High Temperature Imaging of PAO with Oiliness Agents by FM-AFM. Tribology Conference 2019 Spring in Tokyo, Oral presentation
6. MORIGUCHI Shiho, KOKAWA Ryohei, FUJINO Keita, TSUJIMOTO Teppei, SASAHARA Akira, ONISHI Hiroshi: FM-AFM Imaging of Interfaces between Lubricants Containing Oiliness Agent and an Iron Substrate. International Tribology Conference Sendai 2019, Oral presentation

Publications

1. MORIGUCHI Shiho, TSUJIMOTO Teppei, SASAHARA Akira, KOKAWA Ryohei, ONISHI Hiroshi: Nanometer-Scale Distribution of a Lubricant Modifier on Iron Films: A Frequency-Modulation Atomic Force Microscopy Study Combined with a Friction Test. *ACS Omega*, *4*, 17593-17599, 2019
2. MORIGUCHI Shiho, KOKAWA Ryohei, TSUJIMOTO Teppei, SASAHARA Akira, ONISHI Hiroshi: Analysis of Solid-Liquid Interface by Frequency Modulation Atomic Force Microscopy. *Tribologist, 64-11*, 648-654, 2019

Acknowledgments

First and foremost, I would like to express my sincere thanks to Professor Hiroshi Onishi of Chemistry Department at Kobe University, who has been my academic advisor, for his patient support and excellent guidance for my research. He gave me a lot of precious opportunities which I could never had only in my work. Everything I have experienced as a student will be a valuable resource for my future life. I would like to express my deepest gratitude once again.

I am also deeply grateful to Manager Dr. Ryohei Kokawa of Analytical & Measuring Instruments Division at SHIMADZU CORPORATION and Product Manager of Scanning Probe Microscope Hidero Nakajima of X-ray/Surface Business Unit of Analytical & Measuring Instruments Division at SHIMADZU CORPORATION for providing an environment that I could do the both of study and work. I couldn't have started my Ph.D. challenge in the first place if they did not set up the environment. I used a lot of new setups for the analysis instrument in this study. I would like to express my sincere gratitude to Dr. Masato Hirade and Keita Fujino of X-ray/Surface Business Unit of Analytical & Measuring Instruments Division at SHIMADZU CORPORATION for their great cooperation to making these new setups. In particular, I would like to once again thank Keita Fujino for his cooperation in various things such as preparation for the conference presentation and knowledges in the field of tribology. I would also like to express my deepest gratitude to General Manager Dr. Masahiro Ohta of Device Department at SHIMADZU CORPORATION for his meaningful discussion on the scanning principle of SPM and interpretation of measured data. Besides, I would like to thank Shogo Onomura of Shimadzu Techno-Research, INC. and Kotomi Kuroda of Global Application Development Center at SHIMADZU CORPORATION for helping me balance work and study by

sharing daily tasks. I would like to thank staffs who work for surface analysis at SHIMADZU CORPORATION for their meaningful discussion on the analysis by SPM, which forms the basis of this research.

I would like to show my sincere appreciation to Associate Professor Akira Sasahara of Chemistry Department at Kobe University for his great help for my research. He has always rapidly supported me about the preparation of iron oxide single-crystalline wafer, which was a very important factor in this study. It is thanks to his speedy cooperation that I was able to conduct such experiments in the limited time of three years. And I deeply thank Yasuko Imamura of our laboratory for her great support. She helped me about various procedures. I couldn't finish this Ph.D. student life without her help. I gratefully acknowledge the meaningful discussion of past and present members of our laboratory and I am also grateful that they accepted me as a classmate even though I am much older than them.

I would like to express my deepest gratitude to Manager of Osaka Branch Office1、Lubricants & Specialties Group 2 Teppei Tsujimoto of JXTG Nippon Oil & Energy Corporation for providing me with the lubricant that is the theme of this research. In addition to providing lubricating oil, he provided valuable advice on this research. His curiosity as a lubricant researcher has always indicated the direction this research should advance. Deeply thank again.

I express my sincere thanks to Professor Tomoko Hirayama of Department of Mechanical Engineering and Science at Kyoto University. She has taught me a lot of things in the field of tribology, from the basics to recent trends. I was very fortunate to have the opportunity to discuss with her, a wonderful researcher. Thank you again for taking the time out of your busy schedule to give me the precious comments and guidance for my research. And I also deeply grateful to Dr. Naoki Yamashita of

Department of Mechanical Engineering and Science at Kyoto University for his great help, especially for the experiments with ball on disk friction tester. He prepared the experiment carefully as if it was his own, and he was kind enough to give me advice on how to proceed with the experiment. His thoughtfulness was the best in the world. His courteous instruction enabled me to complete the experiment in a limited amount of time.

I am deeply grateful to President Shuro Fukunaga, Senior General Manager of Testing & Analysis Division Atsuhiro Hayashi, and Department Manager of Analytical Measuring Center Department Noboru Yamashita, at Shimadzu Techno-Research, INC. for allowing me to spend time on my personal studies. I would like to thank my colleagues, Tomohide Daigen, Naoto Ichimaru and Naomi Okuyama of Shimadzu Techno-Research, INC. They have always provided nutrition to my mind, then I was able to get energy to move forward.

Finally, I would like to thank my husband for supporting me financially and mentally.

Thanks to the guidance, encouragement, cooperation and kindness of many people, I was able to finish this work. I would like to express my deepest gratitude to all of you.